2017

Promotional Effect of Molten Carbonates on Proton Conductivity and Oxygen Reduction Reaction – An Experimental and Computational Study

Xiaolei Xiong
University of South Carolina

PROMOTIONAL EFFECT OF MOLTEN CARBONATES ON PROTON CONDUCTIVITY AND OXYGEN REDUCTION REACTION – AN EXPERIMENTAL AND COMPUTATIONAL STUDY

by

Xiaolei Xiong

Bachelor of Engineering
Wuhan University of Technology, 2010

Master of Science
City University of Hong Kong, 2011

Submitted in Partial Fulfillment of the Requirements

For the Degree of Doctor of Philosophy in

Mechanical Engineering

College of Engineering and Computing

University of South Carolina

2017

Accepted by:

Kevin Huang, Major Professor

Xinyu Huang, Committee Member

Hui wang, Committee Member

Changyong Qin, Committee Member

Cheryl L. Addy, Vice Provost and Dean of the Graduate School

ACKNOWLEDGEMENTS

I would like to express my sincere gratitude to my advisor Dr. Kevin Huang for his tremendous guidance, patience, motivation and continuous financial support for my research. His guidance helped me through the whole research and writing of this thesis. I would also like to thank my committee members, Dr. Xinyu Huang, Dr. Hui Wang, Dr. Changyong Qin for serving as my committee members. I also want to thank you for your brilliant comments and suggestions.

My sincere thanks also go to Dr. Xueling Lei, who is the mentor in computational work and trains me to get start the modelling, and Dr. Cuijuan Zhang, who gave me the most detailed guidance for the experiment such as fuel cell fabrication and data analysis. I would also like to thank all other group members, Dr. Yunhui Gong, Dr. Tao Wei, Dr. Lingling Zhang, Dr. Jingjing Tong, and Dr. Jie Wang for their extensive hands-on trainings on experiment skills.

Last but not the least, words cannot express how grateful I am to my family and friends. Their year's love and support encouraged me to take the challenge and finish the thesis.

ABSTRACT

Recent research of Solid oxide fuel cells (SOFCs) is aimed to lower the operating temperature to an intermediate temperature (IT) range of 500 to 700^{o}C, while maintaining a proper performance. This Ph.D. research project investigates the promotional effects of alkaline carbonate eutectics on the proton conductivity of proton conducting electrolytes and cathodic ORR reactivity in SOFCs by both experimental and computational methods.

The ionic conductivity of the MC-BZY composite above 500^{o}C increases with the higher loading of MC. The sample exhibited nearly a factor of two higher conductivity in H_2-containing atmosphere than in air. First-principles DFT modeling further investigated proton transfer at the interface of $BaZrO_3$ and molten carbonate. With the presence of carbonate ion, the energy barrier for proton migration becomes as low as 0.332 eV. The modeling indicates the reduction of energy barrier is resulted from the change of rate-determining step from proton transfer between oxygen atoms to proton rotation around oxygen atom.

Infiltration of MC into porous cathode can reduce the polarization of resistance (R_p), i.e., enhance the oxygen reduction reaction (ORR) activity. The EIS analysis shows that MC has a beneficial effect on reducing R_p for different cathodes including Au, $La_{0.8}Sr_{0.2}MnO_{3-\delta}$(LSM), $La_{0.6}Sr_{0.4}Co_{0.2}Fe_{0.8}O_{3-\delta}$(LSCF) and $La_2NiO_{4+\delta}$ (LNO). Specifically, the study on MC loading effect was carried out on LSCF cathode. It shows that a higher loading makes a greater reduction on R_p and the degree of reduction is the same from 500

to 600^{o}C. As the loading increases to 1.4 wt%, the degree of R_p reduction tends to reach a limit. First-principles DFT modeling was further used to investigate the incorporation of oxygen into MC. The formation of CO_5^{2-} in molten carbonate was considered as a chemisorption of gas oxygen on the surface of MC infiltrated cathodes. After the formation of CO_5^{2-}, it reacts with another CO_3^{2-} to form two CO_4^{2-}, which is a rate-limiting step on potential energy surface. After dissociation, oxygen atoms migrate in molten carbonate, which is energetically favor by intermolecular pathways. An O-O-O linkage is formed between carbonate ions, which facilitates the oxygen migration between carbonate ions.

TABLE OF CONTENTS

LIST OF TABLES

LIST OF FIGURES

LIST OF SYMBOLS

η_{Carnot}	Efficiency of carnot cycle
T_i	Absolute temperature of the inlet gas
T_e	Absolute temperature of the engine exhaust
ΔG_f	Change in Gibbs free energy of formation
ΔH_f	Change in the enthalpy of formation
V_c	Output voltage
E_N	Nernst potential
E_L	Voltage loss due to leakage
η_{act}	Activation overpotential
η_{IR}	Ohmic overpotential
η_{con}	Diffusion overpotential
P_{max}	Maximum of power output
t	Tolerance factor
r_A	Ionic radius of A site cations
V_f	Lattice free volume
σ	Total conductivity
σ_{ion}^0	Ionic conductivity
σ_n^0	n-type conductivity at 1 atm

σ_p^0	p-type conductivity at 1 atm
R_p	Polarization resistance
D*	Oxygen bulk diffusion
k*	Surface exchange coefficient
E[ρ]	Total energy of the system
ρ	Single electron density
T[ρ]	Kinetic energy
V_{ext}[ρ]	Potential energy from the external field from nuclei
V_{ee}[ρ]	Electron-electron interaction energy
T_s [ρ]	Kinetic energy of a system of non-interacting electrons
E_{xc}[ρ]	Exchange-correlation functional
$V_{Hartree}$	Hartree energy
E_{corr}	Correlation energy
$\varepsilon_{XC}(r)$	Exchange-correlation energy density
$\varepsilon_{XC}^{LDA}(r)$	Localized exchange-correlation energy density
∇	The gradient operator
E_a	Activation energy
k	Reaction rate coefficient
P_{H_2O}	Water partial pressure
P_{O_2}	Oxygen partial pressure
T	Temperature

LIST OF ABBREVIATIONS

AFC ..... Alkaline Fuel Cell

APUs ..... Auxiliary Power Units

APT ..... Atomic Polar Tensor

ASR ..... Area-Specific Resistance

BSCF ..... Sr- and Fe- doped $BaCoO_3$

BZY ..... Y- doped $BaZrO_3$

CHP ..... Combined Heat and Power

DFT ..... Density Functional Theory

DSC ..... Differential Scanning Calorimetry

DPB ..... Double Phase Boundary

EDX ..... Energy Dispersive X-ray spectroscopy

EIS ..... Electrochemical Impedance Spectroscopy

EPS ..... Emergency Back-up power Supply

ESP ..... Electrostatic Spray Deposition

FCC ..... Face-Centered Cubic

FE-SEM ..... Field Emission Scanning Electron Microscopy

GDC ..... Gd-Doped CeO_2

GGA ..... Generalized Gradient Approximation

HF ..... Hartree-Fock

H-FCEVs..... Hight-duty Fuel Cell Electric Vehicles

HT ..... High Temperature

HTPC .....High Temperature Protonic Conductor

HVE .....High Valence Element

IPCC..... Intergovernemental Panel on Climate Change

IRC..... Intrinsic Reaction Coordinate

IT..... Intermediate Temperature

LDA .....Local Density Approximation

L-FCEVs .....Light-duty Fuel Cell Electric Vehicles

LK .....Li_2CO_3-38mol% K_2CO_3 eutectic

LN .....Li_2CO_3-48mol%Na_2CO_3 eutectic

LSCF .....Sr- and Fe- doped $LaCoO_3$

LSCM.....Sr- and Cr- doped $LaMnO_3$

LSGM ..... Sr- and Mg- doped $LaGaO_3$

LSM .....Sr-doped $LaMnO_3$

LST ..... Sr-doped $LaTiO_3$

LTVs.....Light Traction Vehicles

LVE ..... Low Valence Element

MC .....Molten Carbonate

MCFC .....Molten Carbonate Fuel Cell

MIEC..... Mixed Ion-and Electron Conductor

NASA..... National Aeronautics and Space Administration

NEB.....Nudged Elastic Band

OCV .....Open Circuit Voltage

ORR ..... Oxygen Reduction Reaction

PAW .....Projector Augmented-Wave Method

PBE .....Perdew-Burke-Ernzerhof functional

PLD ..... Pulsed Layer Depositon

PP .....Pseudopotential

PW..... Plane Waves

PW91.....Perdew-Wang functional

RDS.....Rate-Determining Step

PAFC..... Phosphoric Acid Fuel Cell

PEMFC ..... Polymer Electrolyte Membrane Fuel Cell

PES.....Potential Energy Surface

PM..... Particulate Matters

PM10..... Particulate Matter-10

RAPS..... Remote-Area Power Supply

SDC..... Sm- doped CeO_2

SOFC.....Solid Oxide Fuel Cell

SOFC-H^+ ..... Proton-based SOFC

SOFC-O^{2-} .....Oxide ion based SOFC

SSZ.....Scandium-Stabilized Zirconia

TEC..... Thermal Expansion Coefficient

TEM ..... Transmission Electron Microscopy

TPBs..... Triple Phase Boundaries

TS ..... Transition State

VASP ..... *Vienna Ab-initio Simulation Package*

VOCs..... Volatile Organic Compounds

XRD ..... X-ray Diffraction

YSB..... Yttrium-stabilized Bi_2O_3

YSZ ..... Yttria Stabilized ZrO_2

ZPE .....Zero-Point Energy

CHAPTER 1

INTRODUCTION

1.1 Motivation of Research

1.1.1 Energy security

Energy is a crucial source for human survival and development. To maintain a modern life style on current populations needs a great amount of energy supply to power almost everything from transportation to industrial goods production. It is estimated that every calorie in food product consumes ten calories of fossil fuel energy for fertilizer, pesticide, packaging, transportation and operating facilities. Sufficient energy supply is the engine for economic growth [1, 2], which is however affected by dynamics of political and ecological environments. Therefore, energy source has become an important national security issue. In general, energy security is about the relative availability, affordability, and safety of energy and services.[3]

However, due to the non-uniform distribution of energy sources, different regions and countries have their own situations. Saudi Arabia is known as the largest exporter of crude oil, but it lacks industry to refine gasoline. The United States is a net exporter of coal but still imports oil and natural gas. Russia has great source of natural gas but lacks of uranium. Japan as the third largest economy in the world but has no domestic fossil fuels reserves

and completely depends on foreign supply. These examples reveal that energy security is not simple and standing alone issue by any countries, which is deeply affecting the diplomatic relations in a geographic context.

1.1.2 Climate change

Although energy sources vary in fossil, renewable and fissile, fossil fuels are the main energy resource due to the consideration of accessibility, cost and technology capability.[4] In the United State, for example, half of the electric power produced by conventional coal-fired power plants and less than 30% of electricity was produced by non-fossil fuels, as shown in Figure 1.1.

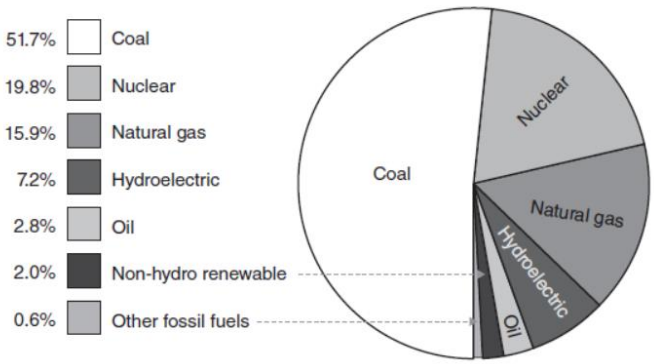

Figure 1.1. Distribution of U.S. power plants by fuel type in annual production[5]

The by-products of burning fossil fuels, such as CO_2, SO_x, NO_x and particulate matters etc., cause serious environmental pollution and climate change. The air pollution happened nowadays is mainly caused by the emissions from power plants, vehicles and furnaces in factories. These emissions contain O_3, CO_2, NO_x, SO_x, particulate matters (PM) and volatile organic compounds (VOCs). They are either the air pollutants themselves or react with other chemicals then polluting atmosphere. For example, while SO_x and NO_x are emitted into the atmosphere, a series of chemical reactions with water produce acid rain.

The acidic raindrop damages buildings and contaminates soil and water sources affecting the farming industries. Besides, air pollution also do harms to human health causing respiratory illness, pulmonary illness, cancer and etc..

On the other hand, CO_2 as greenhouse gas causes more serious global environmental problem and climate change. Greenhouse gases can partially absorb and reflect infrared radiation back to the surface of Earth in the atmosphere, which keeps the planet surface warm, a process termed greenhouse effect. Originally, the Earth benefits from the greenhouse effect to support living creatures by increasing near-surface air temperature to 15^oC.[5] However, scientists have observed a continuous increase of global mean temperature from 1950s and found that it has increased about 0.65 to 1.06 ^oC during 1880 to 2012, as shown in Figure1.2. In the Intergovernmental Panel on Climate Change (IPCC) report 2014, scientists have reached consensus that the global warming is caused by human activities, viz. the increasing concentration of CO_2, CH_4 and N_2O since the Industrial Revolution when people begin to burn fossil fuels as the energy sources. Figure 1.2 shows CO_2 emissions amount from combusting fossil fuels and Figure 1.3 shows that the concentration of CO_2 and CH_4 in the lower atmosphere is increased by 30% and 143% from 1860 to 2000, respectively. In the same period, Earth's near-surface temperature has increased by around 0.6^oC as shown in Figure 1.4. This raise of temperature is unusually high in the past. Besides, other evidences such as attenuation of Arctic sea ice, snow cover and rise of global average sea level are also an indicative of global warming. For the future, climate model predicts that the global surface temperature is likely to rise a further 0.3 to 1.7 ^oC with the lowest emissions and 2.6 to 4.8 ^oC with the highest emissions in the end of 21st Century[6].

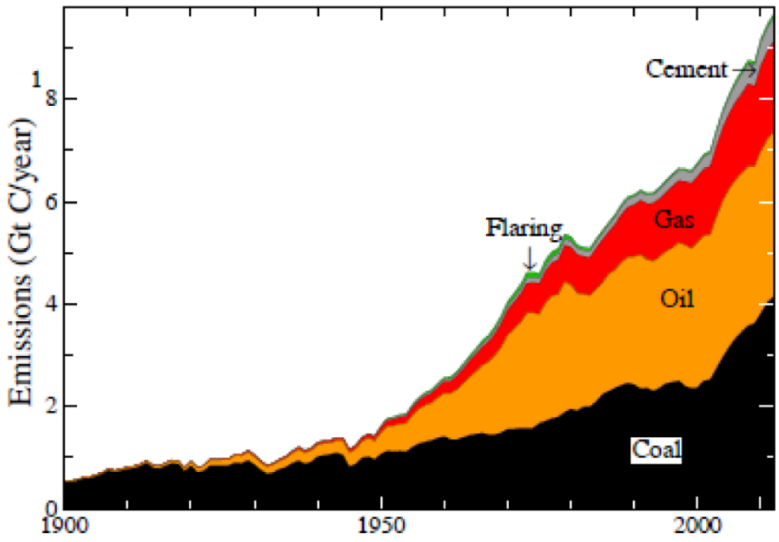

Figure 1.2. CO_2 annual emissions from fossil fuel use. [7]

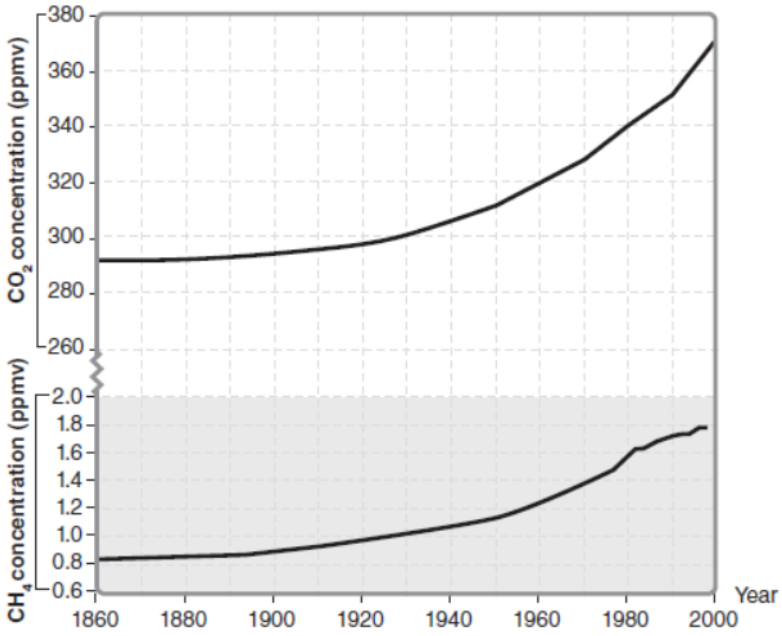

Figure 1.3. From 1860 to 2000, concentrations of CO_2 and CH_4 in the lower atmosphere.[5]

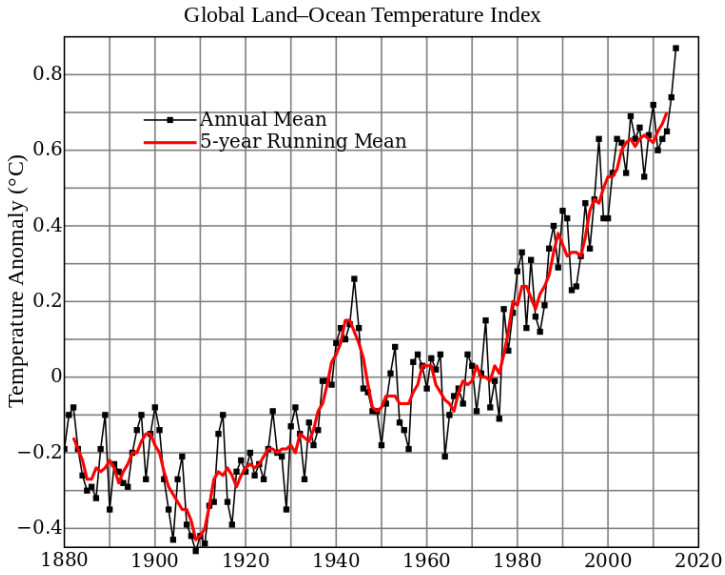

Figure 1.4. Global mean surface temperature relative to 1951-1980 mean. [7]

As global warming will not be regionally uniform, the effect of global climate change will be different in some regions going warmer or wetter. Thus, occurrence of extreme weather such as heavy rainfall, encroaching seas, droughts, heat waves, storms or hail, will happen more frequently.[8-10] Additionally, global warming leads to sea level rising. Since 1993, the sea level has gone up on average 2.6 to 2.9 mm per year with accelerated rate from 1995 to 2015 [11, 12]. Especially, once the global mean surface temperature rises up to 2 ^{o}C, sea level rise will eventually rise to 1 to 4 m resulting from the melting of ice caps and thermal expansion of sea water.[12] Global warming and climate change may potentially lead to food and water shortages, spread of infectious disease, mass migration and extreme property, all of which could further cause increased international conflict.[13]

With the worldwide economy growing, the worldwide energy demand and prices will be high, expecting to increase by more than 300% by the end of the century. Based on the current energy mix, the growing fossil fuel consumption will cause more serious greenhouse gas emissions and may result in unpredictable change to the global climate in

the next decades.[14] Except for environmental issues, fossil fuels with limited storage diminish rapidly and will exhaust in the foreseeable future. The world is facing a change from abundant fossil energy supply to a largely resource-constrained supply in the future. As an alternate choice, nuclear energy is still not generally used for most countries due to its safety issues, technology monopoly and relatively high cost. In contrast, renewable energy sources are more attractive due to the independence on foreign energy sources, pollution and safety issues. Renewable energy sources are energy from naturally repetitive and persistent flows of energy occurring in the local environment [15], such as solar energy, wind energy, biomass energy, geothermal energy, etc. They are the primary, domestic and clean energy, which is the solution to resolve the present environment issues and improve energy security [16]. However, the intermittent nature of renewable energy hinders commercial development and additional infrastructure such as energy storage is needed to deploy the technology.

There is a promising sustainable style called “hydrogen economy”. In this system, hydrogen fuel cells are coupled with electrolyzers and renewable energy conversion technique to construct a close-loop, environment-friendly energy economy. The electricity produced from solar or wind farms can be directly supplied to cities, while excess electricity can be used to produce and store hydrogen via electrolysis. When the renewable energy is not available, the fuel cells operated on hydrogen can be dispatched to provide electricity by consuming the stored hydrogen. In addition, some fuel cells are flexible to fossil fuels. While they are powered with the traditional fossil fuels, the same power output consumes less fuel with less CO_2. Fuel cells combined with the renewable energy would be an attractive technology to solve the environmental issue and energy security.

1.2 Fuel cell technology

A fuel cell is an electrochemical device that directly converts the chemical energy of fuels to electrical energy by harnessing the electrons through oxidizing the fuels. Thus, without burning, pollutants such as NO_x, SO_x, and particulate emissions are almost nil. Fuel cells are not only powered by the common fossil fuels, but also compatible with hydrogen, renewable sources and modern energy carriers for sustainable development and energy security. Besides, fuel cells are modular, thus easily scaling up to larger systems, e.g. from the 1-W range of consumer electronics to megawatt range of power plants. They have higher energy densities and quicker recharge time by refueling. Compared to conventional technologies, fuel cells show better efficiency, greater scaling flexibility, reduced emissions and other advantages.

Fuel cell has a long developing history. Dating back to the early 19th century, a Swiss scientist Christian Friedrich Schœnbein first proposed a possible fuel cell device that combines hydrogen with oxygen to produce electricity. In the meantime, an English scientist William Robert Grove built a device called “gas cell” to generate electricity by combining hydrogen and oxygen. This “gas cell” was considered as the first fuel cell device. In 1959, an English engineer, Francis Thomas Bacon, successfully operated a completed fuel cell similar to today’s version. From then on, scientists reached a several important milestones and developed a series of practical fuel cells for special programs like the Apollo space missions as well as on the Space Shuttle orbiters. It was until the early of 21st century that commercialization of fuel cells had really begun with a worldwide development.

1.2.1 Types of fuel cells

Scientists/engineers have developed many types of fuel cells, which can be categorized by the electrolyte materials. Fuel cells vary in operating temperature, power output and application. Among them, there are five major types of fuel cells: proton exchange membrane fuel cell (PEMFC), alkaline fuel cell (AFC), phosphoric acid fuel cell (PAFC), molten carbonate fuel cell (MCFC) and solid oxide fuel cell (SOFC). Figure 1.5 shows the working principle of the five major types of fuel cells.

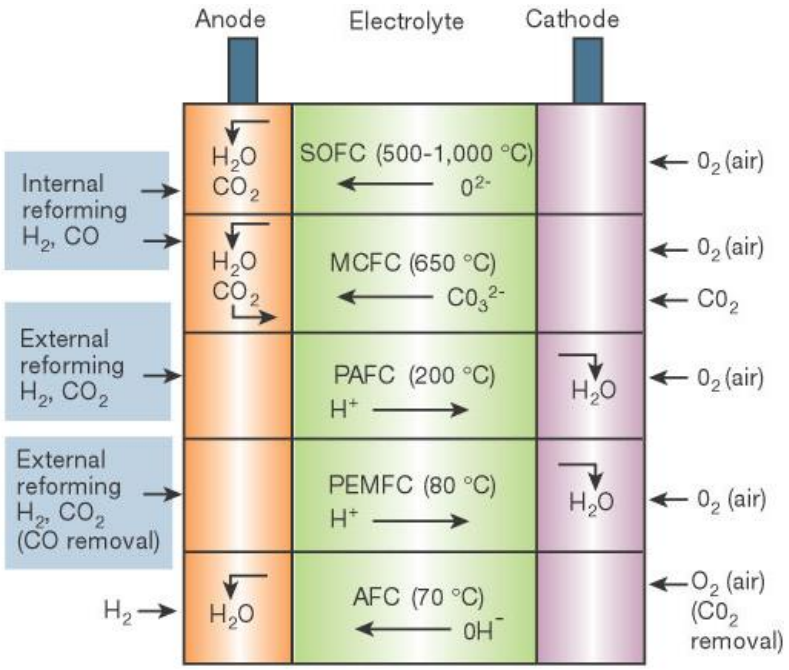

Figure 1.5. Schematic of five major fuel cells.[17]

Proton exchange membrane fuel cell (PEMFC) uses a polymer electrolyte membrane to transport proton, which is oxidized on anode and release electrons to the external circuit. Since PEMFC operates at lower temperature (80 ^oC), it needs the precious metal of platinum on anode and cathode to activate the oxidation of H_2 and reduction of O_2 reaction:

Anode: $H_2 \rightarrow 2H^+ + 2e^-$ (1-1)

Cathode: $1/2O_2 + 2H^+ + 2e^- \rightarrow H_2O$ (1-2)

Since the polymer membrane has to be hydrated with water to provide conductivity, the operating temperature is limited to below the boiling point of water, less than 90 ^oC. Such a low temperature makes platinum based materials be the only suitable catalysts for now. Nevertheless, PEMFC is still too expensive to the market due to materials cost. The PEMFC is proved to be highest power producing fuel cell among other types of fuel cells aforementioned. Besides, it has the features of fast start-up, high efficiency and safety, which make it the most promising candidates for transport applications.

Alkaline fuel cell (AFC) uses potassium hydroxide aqueous solutions as the electrolyte to transport hydroxyl from cathode to anode; its operating temperature ranges from 23 to 70 ^oC. It does not need precious metal catalysts to catalyze the following cathode and anode reactions:

Anode: $H_2 + 4OH^- \rightarrow 4H_2O + 4e^-$ (1-3)

Cathode: $2H_2O + O_2 + 4e^- \rightarrow 4OH^-$ (1-4)

From the reactions, water are present in reactants and products. The excess water produced needs to be removed in order to avoid diluting the electrolyte. Besides, the electrolyte is extremely sensitive to CO_2, which will degrade the KOH electrolyte to produce carbonates. Thus, it can only use pure hydrogen and oxygen, or the cell would suffer performance loss in long-term operation. On the other hand, AFC possesses advantages of making it suitable for some important applications. Since a wide range of metal-based catalysts can be stable in alkaline solutions, cheap catalysts such as nickel rather the expensive platinum could be used as the cathode. Also, the oxygen reduction reaction (ORR) kinetics is more rapid, allowing it to achieve a high working voltages, like 0.875 V. Thus, AFC was historically

successful in the mid-1960s, when the National Aeronautics and Space Administration (NASA) of the U.S. first used AFC to provide electricity and drinkable water in many space missions. However, due to the limitations that KOH electrolyte needs to be continually refilled in the long term use, AFC is not yet suitable for most remote power applications.

Phosphoric acid fuel cell (PAFC) uses concentrated phosphoric acid as the electrolyte supported in a porous matrix of Teflon bonded silicon carbide; the concentrated phosphoric acid can transport proton from anode to cathode. The electrodes are carbon-supported platinum metal catalyst to catalyze the following electrode reactions:

Anode: $2H_2 \rightarrow 4H^+ + 4e^-$ (1-5)

Cathode: $O_2 + 4H^+ + 4e^- \rightarrow 2H_2O$ (1-6)

Its working temperature is around 200 - 215 ^oC in order to achieve a high proton conductivity in acid. During the operation, phosphoric acid must be replenished periodically to compensate the loss due to evaporation. Although PAFC uses platinum as catalysts, the higher operating temperature makes it more resistant to impurities than PEMFC. Hence, PAFC does not require pure oxygen and is able to use reformed fossil fuels and air as the fuel and oxidant, respectively. PAFC is the most developed and commercialized fuel cell technology in stationary combined heat and power applications with power output ranging from 200kW to 1MW. Nevertheless, the high manufacture cost is still a major challenge to a widespread commercial use.

Molten carbonate fuel cell (MCFC) utilizes molten alkali carbonate as the electrolyte sandwiched by two porous Ni-based electrodes. Hence it operates at high temperatures, 600-700 ^oC. At the anode side, hydrogen and carbon monoxide react with carbonate ions to form carbon dioxide, water and electrons. In the meantime, oxygen reacts with carbon

dioxide to form new carbonate ions into electrolyte:

Anode: $H_2 + CO_3^{2-} \rightarrow H_2O + CO_2 + 2e^-$ (1-7)

Cathode: $1/2O_2 + CO_2 + 2e^- \rightarrow CO_3^{2-}$ (1-8)

From the above reactions, CO_2 is the product in anode and the reactant in cathode. Therefore, CO_2 can be recycled from anode and to cathode. Normally, anode is a porous Ni or Ni/Cr/Al alloy, while cathode is porous Li-doped NiO. Due to the high operating temperature and free of CO_2 poison issue, MCFC has the advantage in a flexible fuel choice, such as using simple hydrocarbons and simple alcohols as fuel. MCFC is typically used for combined stationary heat and power applications ranging from 250 KW to 1 MW in electrical utility, military and industrial applications.

Solid oxide fuel cell (SOFC) is also a high-temperature fuel cell, the operating temperature of which ranges from 600 to 1000 ^oC. The electrolyte is a ceramic, either oxide-ion conductor, or proton conductor. Electrodes are oxides or oxide/metal cermets, free from precious metals. The electrode reactions are:

For oxide-ion conductor based SOFCs

Anode: $H_2 \rightarrow 2H^+ + 2e^-$ (1-9)

Cathode: $1/2O_2 + 2H^+ + 2e^- \rightarrow H_2O$ (1-10)

For proton conductor based SOFCs

Anode: $H_2 + O^{2-} \rightarrow H_2O + 2e^-$ (1-11)

Cathode: $1/2O_2 + 2e^- \rightarrow O^{2-}$ (1-12)

The anode and cathode are quite different materials. The anode should be able to withstand the reducing environment. The commonly used material is a nickel based metal-ceramic mixture. Nickel conducts electrons and catalyzes the oxidation of hydrogen, while the

ceramic ionic conductor is the electrolyte materials providing ionic conductivity. The cathode materials are usually highly catalytic oxides. The mixed ion- and electron conducting (MIEC) oxides always show a great performance. SOFC has a wide applications ranging from auxiliary power units to stationary power generations with outputs from 100W to 2 MW. The high operating temperature gives advantages such as fuel flexibility and high-grade heat. However, it has issues of a slow start-up process, degradation of performance in long-term operation and high manufacturing costs. Lowering the operating temperature to the intermediate-temperature (IT) (400-700^{o}C) can solve most of the issues. For instance, cheaper sealing materials and inexpensive metals for interconnects can be used, meanwhile the IT-SOFC can still maintain reasonably high efficiency and fuel flexibility.

In summary, there is still no one type of fuel cell ready for the market entry, unless the issues with cost, power density, reliability and durability can be greatly improved. Among these five types of primary fuel cells, PAFCs and AFCs have been developed and used in some applications since the early time. PEMFCs and SOFCs were catching up in recent years due to their better performance in broadened applications, and poised to attract more attention in the future. Especially, PEMFCs are suited for portable power applications because of the high power density and low operating temperature. In the residential and stationary power applications, PEMFCs and SOFCs are the better choice. High-temperature fuel cells have the advantages in higher efficiency, fuel flexibility and high-quality waste heat, which are suited for combined heat and power applications. A comparison among these fuel cells is give in Table 1.1.

Table 1.1 Comparison of Fuel Cell Types

	PEMFC	AFC	PAFC	MCFC	SOFC
Electrolyte	Polymer membrane	KOH aqueous solution	H_3PO_4 solution	Molten carbonate	Ceramic
Charge carrier	H^+	OH^-	H^+	CO_3^{2-}	O^{2-}
Catalyst	Pt	Pt	Pt	Nickel	ceramic
Operating temperature	50-100 °C	23-70 °C	200 °C	600-700 °C	600-1000 °C
Fuel	H_2, CH_4	H_2	H_2	H_2, CH_4	H_2, CH_4, CO
Advantages	High power density, low operating temperature	High cathode performance, non-precious-metal catalyst	Technologically mature, Good tolerance to contaminants	Fuel flexibility, non-precious-metal catalyst, high-quality waste heat	Fuel flexibility, non-precious-metal catalyst, completed solid-state electrolyte, High-quality waste heat
Disadvantages	Expensive catalyst, membrane and cell components, poor poison tolerance	Water management issues, replenishment of KOH electrolyte, requirement for pure H_2 and O_2	System complexity, Expensive catalyst	System complexity, corrosive molten electrolyte, expensive cell components	System complexity, High operating temperature, expensive cell component

1.2.2 Features

One of the great advantages of fuel cells is the high energy conversion efficiency. As a traditional and widely used energy conversion, efficiency of internal combustion engine is limited by the ideal reversible Carnot cycle:

$$\eta_{Carnot} = \frac{T_i - T_e}{T_e} \tag{1-13}$$

where T_i is the absolute temperature of the inlet gas and T_e is the absolute temperature of the engine exhaust. The efficiency is about 20-30%. Since fuel cells are electrochemical devices where fuels are isothermally oxidized, the efficiency is effected only by the chemical energy content of the fuels:

$$\eta = \frac{\Delta G_f}{\Delta H_f} \tag{1-14}$$

where ΔG_f is the change in Gibbs free energy of formation and ΔH_f is the change in the enthalpy of formation. Comparing to the combustion engines, fuel cells convert chemical energy to electrical energy with an efficiency up to 60% as shown in Figure 1.6. Moreover, if fuel cells are operated in a combined heat and power (CHP) system, the heat produced can be recovered and the system efficiency can go up to 85-90% [18, 19].

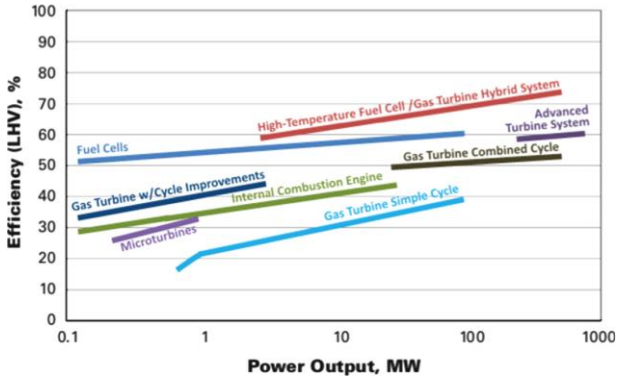

Figure 1.6. Efficiency comparison, including fuel cells and other energy conversion devices. [20]

Another important feature of fuel cells is low emissions. The clean nature of fuel cells relies on the type of fuels. For the fuel cells operated on pure hydrogen, the product are water and heat, undoubtedly zero emission. On the other hand, some fuel cells have reformer system to produce hydrogen from methane, methanol, and hydrocarbons. They still emit greenhouse gas, but in smaller amount. The higher conversion efficiency of fuel cells infers a less greenhouse gas emission per unit electricity produced compared to internal combustion engines. Undeniably, to achieve a total zero emission is challenging but meaningful, which relies on scientists/engineers to develop renewable-based hydrogen generation from clean water electrolysis.

Fuel cells have excellent modularity so as to be a potential candidate for domestic and industrial applications. Fuel cells are connected in series to become a stack by flow plates, as shown in Figure 1.7. Numbers of stacks are integrated with balance of plant components (fuel processor, compressor, etc.) to be a functional system. The number of cells in a stack and stacks in a system determine the total power output of a fuel cell system. Fuel cells can meet wide range of demands from micro fuel cells with less than 1W to MW scale prime power plants, with applications ranging transportation, material handling, stationary, portable, and emergency backup power supply.

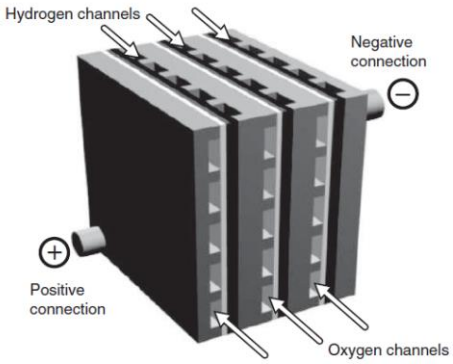

Figure 1.7. Schematic of a fuel cell bipolar stack.[5]

Additionally, fewer moving parts make fuel cells quiet during operation. This feature also contributes to a simpler and compact design, manufacturing, assembly, operation, and analysis than that of heat engines.

1.2.3 Applications

As fuel cells have high modularity, wide power range and efficiency/emission advantage, they have found applications from potable device to large cogeneration power plants in the market. The market value of fuel cells worldwide has doubled from 2008 to 2011 with applications ranging from the back-up power for telecommunication networks market, airport ground support equipment market and material handling market.[21-23] The employment growth in the fuel cell sector has also increased at an annual rate of 10.3% from 2003 to 2010 in the US, which demonstrated the market growth. The United State, Germany, Japan and Canada lead the research and commercialization of fuel cells and the global industry market is expected to grow to billion dollars by 2020.[20]

Portable applications mainly fall in portable power generators for light outdoor personal uses and consumer electronic devices (like cell phones, laptops). Portable fuel cells typically provide 5 to 500 W output. The modularity, high energy density and free from recharging are very competitive features for future portable personal electronics. Also, portable military devices are a growing important application for PEMFCs and direct methanol fuel cells, which is very similar to PEMFC, but use methanol as a fuel, due to its low acoustic signature, high power density and low weight compared to some other batteries.[24, 25]

Stationary applications include residential, commercial and industrial stationary power generation sectors, including emergency back-up power supply (EPS), remote-area power

supply (RAPS), and distributed power or CHP generation. In the EPS market, especially the telecommunications market, the uninterrupted power supply is critical. PEMFCs are the prime choice due to high energy and power density, reliability and modularity. PEMFCs become a promising alternative to batteries in the EPS market. RAPS focuses on gird-isolated locations, where are the sparsely populated regions, like deserts, forest, islands and remote research facilities. It is much more economical to use RAPS than grid power lines.[26] Fuel cells system is also used for residential power or CHP distributed generation on a single household or a community. PEMFCs and PAFCs are suitable for household based CHP generation, while MCFCs and SOFCs are used in large residential block based CHP generation. A CHP fuel cell system will provide not only electricity, but also space heating and water heating demands. MCFCs and PAFCs using natural gas in CHP system reduce 78-88% NO_x emissions, 60% particulate matter-10 (PM10) emissions and 90-99% CO_2 emissions comparing to combustion-based distributed generation CHP.[27] It is expected that CHP systems will take half of the world distributed generation market by 2020 if its cost and durability criteria can be met.[28] CHP for both energy and chemicals generation in industrial processes are also growing.[29]

The transportation industry is in heavy demands on energy, which contributes 18% of the global greenhouse gas emissions [30]. Fuel cells' advantages of near-zero emissions and high efficiency over internal combustion engines can meet the transportation industry expectation. As a consequence, fuel cells research and development for light-duty passenger cars have attracted much attention in the past decades. For instant, Japan made a development plan to manufacture two million fuel cell electric vehicles and one thousand hydrogen refilling stations by 2025[31]. Also, the fuel cell shipments in 2010 indicated that

35% of these shipments was related to transportation.[32] Fuel cell applications for transportation are mainly categorized into auxiliary power units (APUs), light traction vehicles (LTVs), light-duty fuel cell electric vehicles (L-FCEVs), heavy-duty fuel cell electric vehicles (H-FCEVs), aerial propulsion, and marine propulsion.

1.3 Summary

The global energy demand has increased significantly in this century. Economy growth relies on low cost and reasonable energy supply. A great deal of fossil fuels are being combusted worldwide, leading to high air pollution and deteriorating climate. The energy supply stress and environmental problems urge us to make serious and smart decisions to adjust our energy supply structure and promote clean energy conversion technology. Fuel cells as a cleaner, more efficient, and possibly the most flexible chemical-to-electrical energy conversion device can be a powerful asset to be applied in a broad application from personal electronics to megawatt power plants. Fuel cell technology is an excellent choice to mitigate the growing environmental issues and facilitate the utilization and deployment of renewable energy.

CHAPTER 2

DEVELOPMENT OF INTERMEDIATE-TEMPERATURE SOLID OXIDE FUEL CELLS – A REVIEW

Solid oxide fuel cell (SOFC) is a device that electrochemically converts chemical energy directly into electrical energy, which is characterized by high efficiency, fuel flexibility, environmental friendliness, low noise, and easy modularity.[33] A single SOFC is composed of porous anode, cathode and dense electrolyte. The electrolyte can be an oxide-ion or proton conductor. The working principles of oxide ion-based (SOFC-O^{2-}) and proton-based SOFC (SOFC-H^{+}) are shown in Figure 2.1.

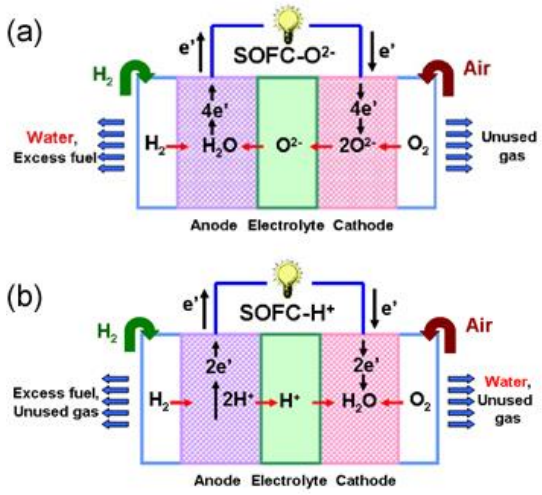

Figure 2.1. Working principles of (a) oxide ion-based and (b) proton-based solid oxide fuel cells.

Take SOFC-O^{2-} as an example. At the cathode side, oxygen molecules are reduced to oxide ions after obtaining electrons from the external circuit, i.e.,

$$\frac{1}{2}O_2+2e'\leftrightarrow O^{2-} \quad (2\text{-}1)$$

Under the driving force of concentration gradient of partial pressure of oxygen, the resultant oxide ions transport across the electrolyte via vacancy and/or interstitial mechanism, and oxidize the fuel at the anode, releasing electrons to the external circuit via

$$O^{2-} + H_2 \leftrightarrow H_2O + 2e' \quad (2\text{-}2)$$

The electrons return to the cathode via the external circuit. The reaction product of water vapor and excess fuel are released from the anode.

The case of SOFC-H^+ is similar except that the protons, rather than oxide ions, diffuse across the proton electrolyte from anode to the cathode, and water vapor is generated at the cathode. The overall reaction for both types of SOFC is the same:

$$H_2 + \frac{1}{2}O_2 \leftrightarrow H_2O \quad (2\text{-}3)$$

Compared with the conventional SOFC-O^{2-}, SOFC-H^+ works at lower temperature (400-750^{o}C) and exhibits lower dependence of performance on temperature owing to the lower protonic activation energy (0.4-0.6 eV vs. 0.8-1.0 eV). Furthermore, SOFC-H^+ possesses higher efficiency because water is generated at the cathode side but at the anode side for SOFC-O^{2-}, which does not dilute the fuel and thus higher voltage. Meanwhile, no internal water treatment system is needed for SOFC-H^+, which significantly simplify the stack structure. [60]

The output voltage of a SOFC can be expressed by [4]

$$V_c = E_N - E_L - \eta_{act} - \eta_{IR} - \eta_{con} \quad (2\text{-}4)$$

where V_c is output voltage; E_N is Nernst potential of single cell; E_L is voltage loss due

to leakage; η_{act}, η_{IR} and η_{con} are activation, ohmic and diffusion overpotential, respectively. Due to various losses, the real voltage-current relationship always deviates from the ideal case, as shown in Figure 2.2. All the losses become more severe with decreasing temperature.

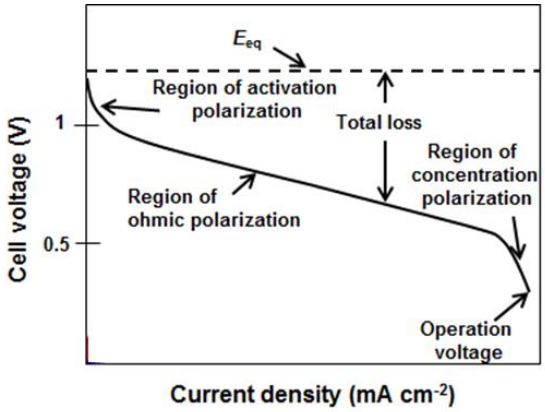

Figure 2.2 Ideal (dash line) and real (solid line) current-voltage curves of SOFC.

The commercial SOFC-O^{2-} work at temperatures ≥ 750^{o}C. Such high operating temperature significantly impedes its deep market penetration due to the high cost and low reliability. To overcome these barriers, it is greatly desirable to reduce the temperature to intermediate temperature range (400-700^{o}C), which can be realized by reducing the thickness of the state-of-the-art electrolyte, development of new electrolyte materials with high oxide ion conductivity and electrode materials of high electrochemical activity, and development of SOFC-H^{+}. Although SOFC-H^{+} shows several advantages over SOFC-O^{2-} as aforementioned, its performance is generally lower than that of SOFC-O^{2-} and thus less attractive for commercial applications. Accordingly, in the following parts, the development, especially recent progress in the electrode and electrolyte materials for SOFC-O^{2-} will be reviewed in detail. The electrolyte materials for SOFC-H^{+} will also be discussed briefly.

2.1 Anode materials

To keep the overpotential losses low at the anode side, the anode material should have high electron and oxide ion conductivity and appropriate porosity (~30%) to extend the triple phase boundaries (TPBs) to the whole anode. One advantage of SOFCs is fuel flexibility, not only pure hydrogen, but also hydrocarbons and even alcohols can be employed as fuels. H_2S-based sulfides always co-exist with hydrocarbons. Therefore, the anode material should be coking and sulfur resistant. The state-of-the-art anode material is Ni-YSZ (yttria-stabilized zirconia) cermet. Several other types of materials, mainly perovskite-oxides, are also developed.

2.1.1 Ni-YSZ cermet

Ni-YSZ is the state-of-the-art anode material for SOFC-O^{2-}, where Ni is the electron conducting phase and catalyst for fuel oxidation and hydrocarbon reforming whilst YSZ is the oxide ion conducting phase to expand the TPBs, to match the thermal expansion coefficient (TEC) of anode with YSZ electrolyte and to serve as the scaffold to improve the sintering resistance of Ni. The electrical conductivity and TEC of anode can be modified by adjusting the ratio of Ni and YSZ. Generally, the dependence of electrical conductivity on volume percent of Ni exhibits characteristic “S-shaped” curve,[34, 35] as shown in Figure 2.3.[34] The content of Ni is higher than 30 vol% to achieve high electrical conductivity, which is predicted by percolation theory. Such sharp increase in conductivity corresponds to the point where a continuous Ni network forms and the conduction is transited from YSZ-dominated ionic conduction to Ni-dominated electron conduction. The percolation threshold is influenced by many variables such as the porosity, pore size, pore size distribution, size of raw powders, and contiguity of each constituent

component. Thus, the electrical conductivity of Ni-YSZ cermet is a strong function of these factors.[36]

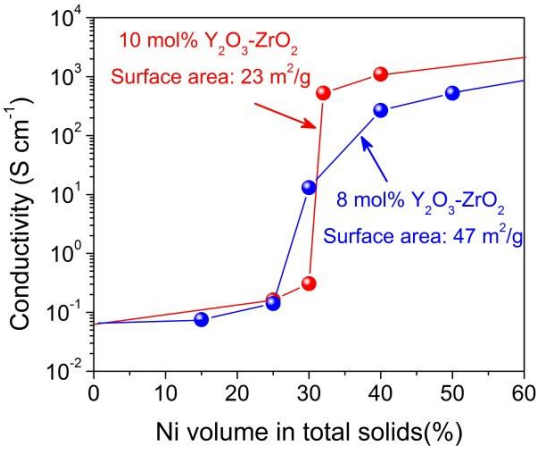

Figure 2.3. Electrical conductivity of Ni-YSZ cermets at 1000°C as a function of volume percent of Ni in total solids fabricated with two types of zirconia powders.[34]

Not only the electrical conductivity, but also the electrochemical activity is strongly dependent on the Ni content. Figure 2.4 shows the IR resistance and polarization resistance of Ni-YSZ anode.[35] The IR resistance decreases monotonically with the increase in Ni content whereas the polarization resistance reaches a minimum value at appropriately 40 vol% Ni. The former depends on the contact area of Ni on the electrolyte and the latter is associated with the number of reaction sites along the TPBs and strongly dependent on the Ni:YSZ ratio. In addition, different effective anode thickness was reported. Brown et al. found that the active thickness of the fine Ni-YSZ cermet anode is about 10 μm and is supposed to be related with the conductivity of the YSZ network.[37] Nakagawa et al. studied the effect of thickness of nickel film and porous YSZ ceramic layer on the anode polarization at 1000°C and found that the rate-determining step was an activation process and it takes place at very thin zone of the Ni film within 1 μm from the electrolyte/electrode interface.[38] Cha and Xia reported that the polarization reaches the minimum at anode

thickness of roughly 50, 100, and 160 μm for particle size of 0.1, 0.2, and 0.5 μm, respectively.[39]

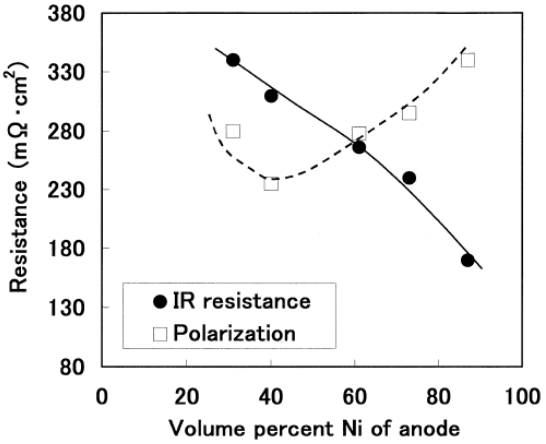

Figure 2.4. IR resistance and activation polarization resistance of single cell with different anodes. A flow of 200 cc/min of hydrogen as fuel and 1000 cc/min oxygen as oxidant in the cathode.[35]

One problem with the Ni-YSZ anode is the degradation with operation. Iwata[40] found that a Ni-YSZ anode degraded by 14 μV/h at 1200 K and by 33 μV/h at 1281 K at a current density of 0.3 A/cm^2. Such anode degradation was due to Ni sintering, which not only decreases the surface area of the Ni particles but also decreases the contact area at the electrolyte/anode interface. The surface area of Ni-YSZ anode decreased from 1.285 m^2/g before running to 0.613 m^2/g after 1015 h operation at 1281 K. The scanning electron microscopy (SEM) observation found that the diameter of Ni particles was about 0.1-1 μm before oepration and increased up to 10 μm after 1015 h. Mercury porosimetry revealed that the Ni-YSZ anode substrate had two pore distribution peaks in the radius ranges of 10-200 and 200-50000 nm before testing. The pore distribution peak in the radius ranges of 10-200 nm shifted toward large pore radius range that it almost disappeared after 1015 h at 1281 K.[40] The sintering of Ni can be alleviated by tailoring the ratio of Ni:YSZ ratio and Ni-YSZ particle size. By employing a YSZ frame made of coarse (average size of 27.0 μm)

and fine (average size of 0.6 μm) powders, Horita et al. successfully stabilized the anode overpotential for ca. 3000 h.[41] The coarse and fine YSZ particles form a solid framework and prevent damages on the reduction of NiO and Ni agglomeration.

Another challenge with the Ni-YSZ anode is the nickel oxidation during fuel starvation and volume change during gas fluctuations between reducing and oxidizing conditions, which leads to irreversible degradation even failure of the SOFC stack.[42-44] In addition, its resistance to coke deposition (due to the high catalytic activity of Ni towards C-C bond cleavage)[45, 46] and sulfur poisoning (due to the strong adsorption of H_2S on Ni active site)[35, 47, 48] is rather poor when hydrocarbons and sulfides with low concentration of water vapor in the fuel gases. To solve this problem, Kurokawa et al.[49] infiltrated ceria nanoparticles to the conventional Ni-YSZ anode and they found that adding 40 ppm H_2S to the H_2 stream of an unmodified SOFC caused the cell voltage to drop to zero within several minutes. After the addition of ceria nanoparticles, the addition of 40 ppm H_2S caused the cell voltage to drop from 0.78 to 0.6 V after several minutes but then the performance was sable for the next 500 h. Switching the feed stream back to pure H_2 restored the initial performance of the cell. Alternatively, new anode materials have been developed in terms of replacing Ni with other metals (such as Cu) and developing mixed oxygen ionic-electronic conductors (MIECs).

2.1.2 Cu-based cermet anode materials

Compared with Ni, Cu shows weaker catalytic activity towards the cleavage of C-C bond and thus higher coke-deposition resistance. Moreover, the cost of Cu is lower. The ceramic phase can be not only YSZ, but also CeO_2, which is a good MIEC in reducing atmosphere and also demonstrates good catalytic activity towards the oxidation of

hydrocarbons. Furthermore, CeO_2 shows excellent resistance to coke deposition and sulfur poisoning.[48] Gorte et al.[50] fabricated Cu-YSZ and Cu-CeO_2-YSZ anodes with ionic impregnation. The resultant single cell with the above two anodes, YSZ electrolyte and LSM-YSZ cathode delivered P_{max} of ~55 and 300 mW cm^{-2} (H_2 as fuel), and 30 and 120 mW cm^{-2} (C_4H_{10} as fuel) at 700 °C, respectively. No coke deposition was observed on Cu-CeO_2-YSZ anode for 70 h of test at 700 °C with C_4H_{10} as fuel. Cu particles, however, tend to coarsen over time owing to their relatively low melting point (1085 °C), causing decreased electronic conduction; they also have poor catalytic activity for direct hydrocarbon oxidation, limiting the power output.

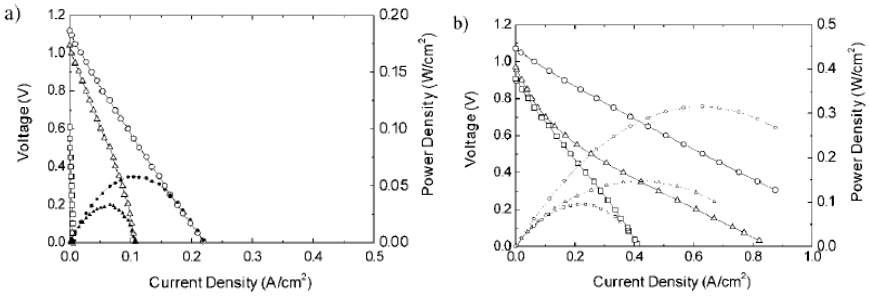

Figure 2.5. Current-voltage and current-power curves for an SOFC using (a) Cu-YSZ and (b) Cu-CeO2-YSZ cermet as the anode at 700 °C with different fuels, H2 (○), C4H10 (△), and CH4 (□).

2.1.3 $SrTiO_3$-based anode materials

The $SrTiO_3$-base materials are the most widely investigated MIEC anode due to its stability in reducing atmosphere and relatively high electrical conductivity. Hui and Petric first investigated the feasibility of Y-doped $SrTiO_3$ as anode for SOFC-O^{2-}.[51] $Sr_{0.86}Y_{0.08}TiO_3$ showed electrical conductivity of as high as 82 S cm^{-1} at 800°C and p(O_2) of 10^{-19} atm，and also good reversibility of conductivity upon oxidation and reduction. This material shows very good structural stability over broad temperature (RT-1400°C) and $p(O_2)$

(1-10^{-20} atm) ranges, and good TEC and chemical compatibility with YSZ and LSGM electrolyte. Marina et al. studied the thermal, electrical, and electrocatalytic properties of La-doped $SrTiO_3$, $La_xSr_{1-x}TiO_3$ (LST). Depending on the dopant amount (x) and $p(O_2)$, LST possesses an electrical conductivity on the order of 0.01-500 Scm^{-1} at 800-1000 ^oC. Furthermore, LST is found to be dimensionally and chemically stable when subjected to oxidation-reduction cycling.[52] All these results demonstrate that $SrTiO_3$-based materials can be promising anode for SOFC-O^{2-}. Although the electrical conductivity of LST is high, its catalytic activity towards H_2 oxidation is lower than that of Ni-YSZ, which can be enhanced by doping. Marina et al. [13] studied the catalytic activity of LST with B-site being doped with Ni, Co, Cu, Cr, Fe and Ce and found that Ce-doping can significantly improve the catalytic activity. The polarization resistance of $(La,Sr)(Ti,Ce)O_3$ anode in H_2 (3% H_2O) was 0.2 and 1.3 cm^2 at 850 and 700^{o}C, respectively. The electrochemical performance can be enhanced by addition of catalyst. Lee et al. loaded 45 wt% $La_{0.3}Sr_{0.7}TiO_3$ onto 65% porous YSZ skeleton by infiltration and found that with the addition of 0.5wt% Pd and 5 wt% CeO_2, the maximum power density of SOFC increased to 780 $mWcm^{-2}$ from less than 20 $mWcm^{-2}$ for catalyst-free one at 800 ^oC with 97% H_2/H_2O as fuel.[53]

Vey recently, Irvine's group reported that the electrocatalytic activity of $SrTiO_3$ can be significantly enhanced by exsolution in the form of in-situ growth of nanoparticles. [54, 55] They demonstrated that growing nano-sized phases from perovskites can be controlled through judicious choice of composition, particularly by tuning deviations from the ideal perovskite stoichiometry ABO_3. A-site deficient perovskites are more prone to exsolve B-site species than the oxygen-excess ones and thus non-stoichiometry control can be employed to produce decorated perovskite surfaces with evenly distributed nanoparticles

when traditional formulations cannot. When reduced at 930 ºC for 20 h in flowing 5% H_2/Ar, the A-site deficient oxygen stoichiometric composition $La_{0.52}Sr_{0.28}Ni_{0.06}Ti_{0.94}O_3$ precipitates out numerous metallic Ni nanoparticles that uniformly covered the surface of the parent perovskite, whilst no particle growth was observed from the A-site stoichiometric oxygen-excess $La_{0.3}Sr_{0.7}Ni_{0.06}Ti_{0.94}O_{3.09}$ composition, even though both samples possessed 6% Ni on the B-site (Figure 2.5). It is also found that the surface morphology of the as-prepared porous samples correlated with oxygen non-stoichiometry. O-deficient compositions developed distinctive, terraces-like motifs. The separation between adjacent terraces decreased significantly for O-stoichiometric compositions and eventually faded into a smooth surface for O-excess compositions. The exsolution phenomenon occurred preferentially along the edge of these terraces, and typically never in the separation zone between them. The exsoluted Ni particles are universally socketed in the perovskite surface, which show strong adhesion between metal and oxide phases. These features appear to contribute synergistically towards considerably improving the anchorage of exsolved particles, which contributes to the higher thermal stability of those exsolved Ni particles and improved coke-resistance of those perovskite materials. It should be noted that the Ni-based catalyst prepared by exsolution exhibits a level of activity and sensitivity to H_2S comparable to deposited Ni analogues prepared by conventional deposition methods, but with considerably improved coking resistance.

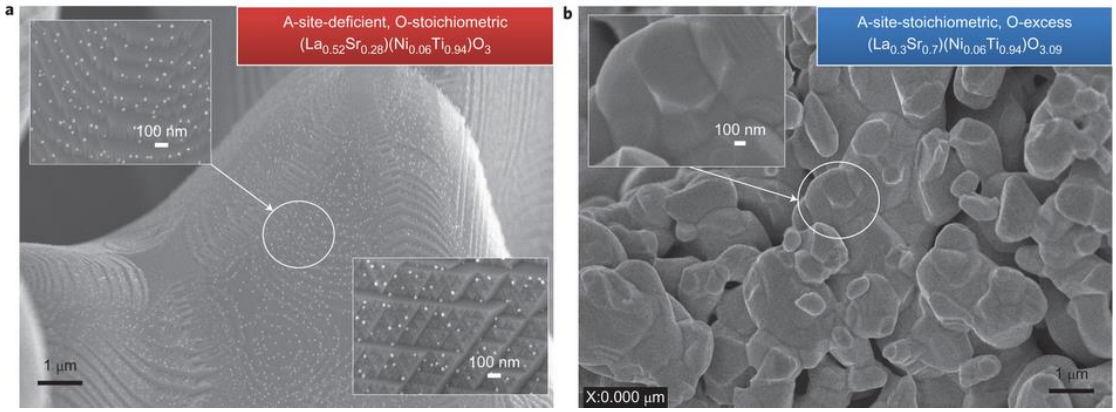

Figure 2.6. Role of non-stoichiometry in the formation of exsolutions on stoichiometric and A-site-deficient peovskites illustrated through SEM images. Exsolution from the initially (a) A-site deficient $La_{0.52}Sr_{0.28}Ni_{0.06}Ti_{0.94}O_3$ and (b) A-site-stoichiometric, O-excess $La_{0.3}Sr_{0.7}Ni_{0.06}Ti_{0.94}O_{3.09}$ samples reduced at 930ºC for 20 h in 5%H_2/Ar.[54]

Although the exsolution by chemical reduction can be carried out in situ and in one step, bringing obvious simplifications to SOFC manufacture, it is still relatively lengthy (taking 10-30 h) owing to the relatively slow speed of ion diffusion in oxide across bulk and surfaces. Additionally, this slow speed might limit the overall extent of exsolution and therefore the final population of surface particles, resulting in limited electrochemical performance. To circumvent this, Myung et al. reported that the exsolution can be triggered under an applied potential in 2016.[56] They show that applied electrical potentials can be instrumental in controlling exsolution, and can significantly enhance it to generate more or less instantly-rich nanostructures with outstanding electrochemical activity and stability. They compared the reduction/exsolution kinetics of two fresh samples $La_{0.43}Ca_{0.37}Ni_{0.06}Ti_{0.94}O_{3-\delta}$ at 900ºC upon exposure to a reducing atmosphere (5%H_2/N_2) or upon application of a 2 V potential (50%H_2O/N_2). Compared with the conventional reduction by hydrogen, electrochemical switching requires less time to complete (~150 s vs. > 17 h); leads to a higher extent of exsolution (~6.2×10^{-7} vs. ~3.7×10^{-7} nickel atoms μm^{-2}); produces a particle population four times greater (370 vs. 90 particles μm^{-2}) at a

smaller average particle size (15 vs. 20 nm), and overall resulted in a sevenfold increase in the maximum fuel-cell power density (1.3 vs. 0.2 W cm^{-2}), as shown in Figure 2.6. The faster kinetics is associated with the much lower $p(O_2)$ differential experienced by the sample when exposed to voltage application (~10^{-35} atm) compared with that achieved through reducing atmosphere (10^{-19} atm). In spite of this tremendous $p(O_2)$ difference, exsolution still occurs in a very controlled fashion, which makes electrochemical switching an appealing method for selective and highly targeted particle growth. As compared with the slow reduction under hydrogen, the sudden flooding of the perovskite lattice with electrons during voltage supplication greatly favors particle nucleation, leading to small yet numerous particles. Despite the small initial exsoluted particle size (~15 nm) and the close proximity of particles to each other, there was no noticeable particle agglomeration. Over 100 h period, additional metal exsolved (from around 130 nm to some 240 nm deep), increasing the particle population and size by about 10%, which results in slightly improved polarization resistance and maximum power density. This work brings an unprecedented simple approach to prepare stable nanostructures with high performance and is worth further study.

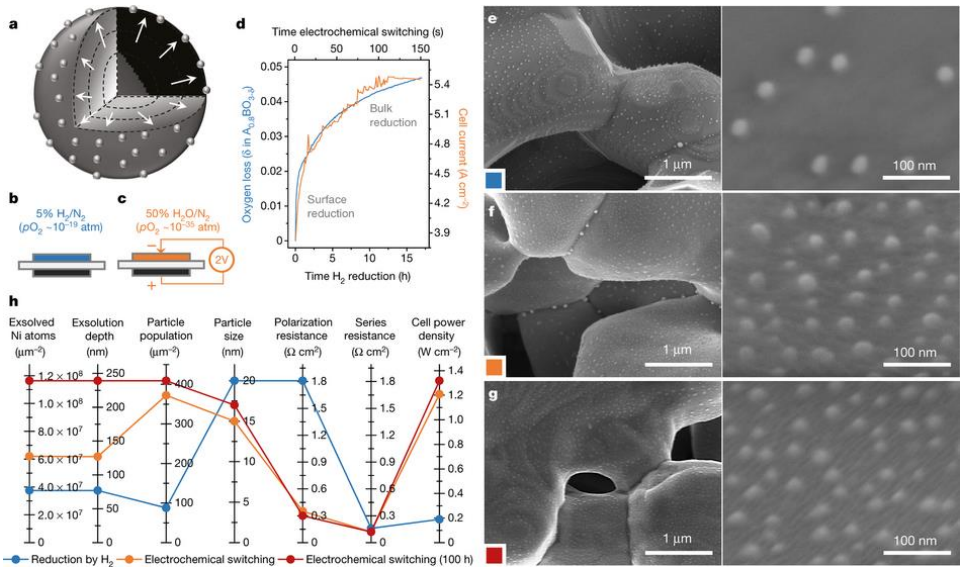

Figure 2.7. (a) The process of redox exsolution: a catalyzing active metal is embedded in the crystal lattice of a backbone in oxidizing conditions, and is exsolved onto the surface as metal particles upon reduction. (b, c) The conditions used to trigger exsolution in a solid oxide cells at the fuel electrode (shaded in blue and orange) by reduction in 5%H_2/N_2 (b) and electrochemical switching by applying 2 V across the cell (c). (d) In blue thermogravimetric analysis (TGA) data showing oxygen loss upon reduction by hydrogen as a function of time. In orange, cell current upon application of 2 V, also as a function of time. This reduction kinetics is typical for titantate systems and suggestions two processes, one fast and one slow, corresponding to surface and bulk reuction. (e, f) SEM images of $La_{0.43}Ca_{0.37}Ni_{0.06}Ti_{0.94}O_{3-\delta}$ electrodes produced by (e) reduction by hydrogen at 900°C for 20 h and (f) electrochemical switching under 50%H_2O/N_2 at 900°C for 150 second. (g) Replica of the sample shown in (f) after 100 h of fuel cell testing at 750 °C in 3%H_2O/H_2 at 0.7 C. (h) Various characteristics of the samples shown in (e-g), plotted in a parallel coordination system. Polarization and series resistances are given at open-circuit voltage. Cells used for this figure had 140 μm thick electrolyte. [56]

2.1.4 $LaCrO_3$-based anode materials

Tao and Irvine[57] reported a new anode material in 2003, $La_{0.75}Sr_{0.25}Cr_{0.5}Mn_{0.5}O_3$ (LSCM)，which exhibited excellent chemical and TEC (9.3×10^{-6} K^{-1}) compatibility with YSZ electrolyte in both air and in 5%H_2. The polarization resistance of LSCM at 900°C was 0.26 Ω cm^2 in wet H_2, which was comparable with the conventional Ni-YSZ anode, but the former showed higher oxidation-reduction stability. The polarization resistance can be decreased with A-site deficient $(La_{0.75}Sr_{0.25})_{1-x}Cr_{0.5}Mn_{0.5}O_{3-\delta}$ material [16]. The

maximum power density of single cell with $(La_{0.75}Sr_{0.25})_{0.9}Cr_{0.5}Mn_{0.5}O_{3-\delta}$ anode is 0.47 and 0.2 W cm^{-2} in wet H_2 and wet CH_4, respectively. [57] Jiang et al. [17] prepared GDC-impregnated LSCM, which greatly improved the catalytic activity towards CH_4 oxidation, with anode polarization resistance of 0.44 Ω cm^2 at 800 ^oC with GDC loading of 4.0 mg cm^{-2}. Kim et al.[58] infiltrated a 65% porous YSZ scaffold with 45wt% $La_{0.8}Sr_{0.2}Cr_{0.5}Mn_{0.5}O_3$ and found that the maximum power density of single SOFC with such anode was only 105 mW cm^{-2} at 700^{o}C. The addition of 5 wt% CeO_2 increased this to 300 mW cm^{-2}. The power density further increases after the addition of 0.5 wt% Pd alone or addition of 0.5 wt% Pd and 5 wt% CeO_2, exhibiting maxima of 500 and 520 mW cm^{-2}, respectively. AC impedance analysis revealed that the ohmic loss is the same for all cells, but the electrode losses in the cell containing Pd is the lowest. Not only Pd, but also Rh and Ni show similar behavior. The maximum power density of cell with 0.5 wt% Rh or 1 wt% Ni catalyst is ~530 mW cm^{-2}. Kim et al.[59] further investigated the performance of SOFC anode based on LSCM-YSZ containing 0.5wt% metals catalysts in methane. The electrode containing Pt was stable in CH_4 but carbon deposits with granular or filamentous morphologies were found with electrodes containing either 0.5wt% Pd or Ni. Carbon deposition with both Pd and Ni was greatly suppressed by the addition of 10wt% ceria as co-catalyst. However, the electrical conductivity of LSCM in reducing atmosphere is low, 38 S cm^{-1} at 900^{o}C at $p(O_2) > 10^{-10}$ atm. In addition, at lower $p(O_2)$ values, conductivity decreases indicating p-type conductivity as the dominant electronic mechanism [15]. In addition, its sulfur tolerance is poor, and its resistance to sulfur poisoning decreases with Mn content due to the generation of MnS and La_2O_2S [18].

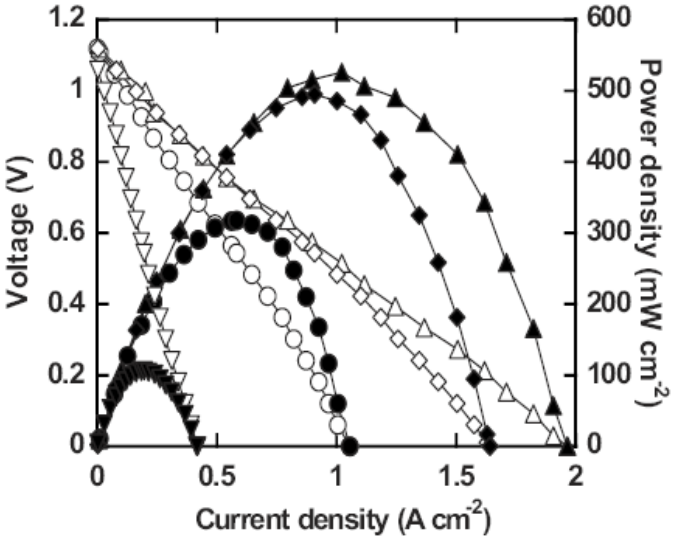

Figure 2.8. Current-voltage and current-power curves in humidified H_2/3%H_2O at 700°C for cells having anodes with 45 wt% LSCM in YSZ, using various catalysts: no catalyst (▽), with 5 wt% CeO_2 (○), with 0.5 wt% Pd (◇), and with 5 wt%CeO_2 and 0.5 wt% Pd (△).[58]

2.1.5 Layered perovskite anode materials

In 2006, the Goodenough group reported a brand new double-layer perovskite ($A_2BB'O_6$, Figure 2.9) anode Sr_2MgMoO_6.[60] The maximum power density of single cell with Sr_2MgMoO_6 anode at 800°C was 838 and 829 mW cm^{-2} with power loss of 3.5% and 2.5% when H_2 and H_2/H_2S were used as fuels, respectively. The exciting performance makes Sr_2MgMoO_6 a possible promising anode material. However, later study revealed that electrochemical activity of this anode material is very sensitive to the current collectors employed. The intrinsic catalytic activity of Sr_2MgMoO_6 was very poor, which could be improved by one to two orders of magnitude with addition of 2 wt.% Pt.[61] The electrical conductivity of Sr_2MgMoO_6 is low, only ~ 6 S cm^{-1} at 800 °C, which can be enhanced with partial or complete replacement of Sr with La, Mg with Co, Ni, and Fe.[62, 63]

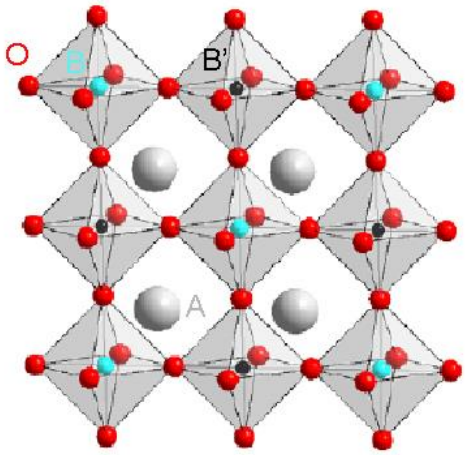

Figure 2.9. Schematic structure of double-layered perovskite $A_2BB'O_6$

Very recent work by Sengodan et al.[64] reported the layered oxygen-deficient double perovskite can be employed as an efficient and stable anode for direct hydrocarbon SOFCs. They prepared the layer perovskite anode $PrBaMn_2O_{5+\delta}$ (PBMO) by in-situ annealing of $Pr_{0.5}Ba_{0.5}MnO_3$ in fuel conditions and actual fuel cell operation, as shown in Figure 2.10. At 800°C, layered PBMO shows high electrical conductivity of 8.16 S cm^{-1} in 5% H_2 and demonstrates peak power densities of 0.57 W cm^{-2} at 850°C using humidified hydrogen fuel. The electrochemical activity can be enhanced by infiltration of PBMO or Co-Fe catalysts. The maximum power density of layered PBMO with the Co-Fe catalyst reached 1.77, 1.32, and 0.57 W cm^{-2} at 850°C in humidified H_2, C_3H_8, and CH_4, respectively. Furthermore, no degradation was observed from coking under a constant current load of 0.2 A cm^{-2} at 700°C in C_3H_8 for more than 500 h, as shown in Figure 2.11. Such results are very exciting and are worth further investigation.

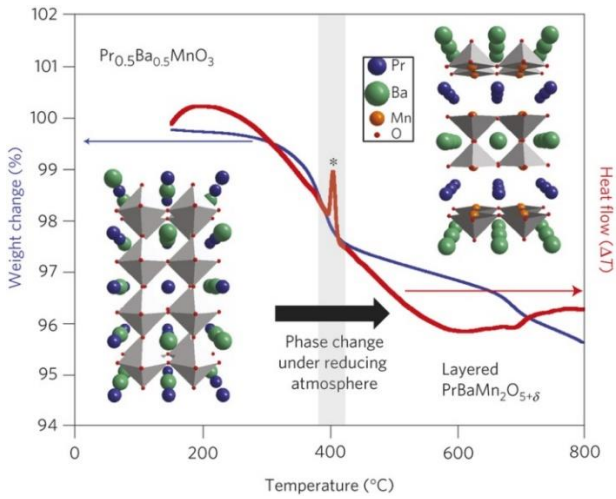

Figure 2.10. Principle of the approach to prepare A-site layered perovskite $PrBaMn_2O_{5+\delta}$. Phase change of $Pr_{0.5}Ba_{0.5}MnO_3$ to layered $PrBaMn_2O_{5+\delta}$ occurs under a reducing atmosphere. The differential thermal analysis curve shows the presence of a sharp exothermic peak on heating at 400°C. A-site layered $PrBaMn_2O_{5+\delta}$ shows that the MnO_2 square sublattcie is sandwiched between two rock salt layers, PrO and BaO layers, along the c-axis.[64]

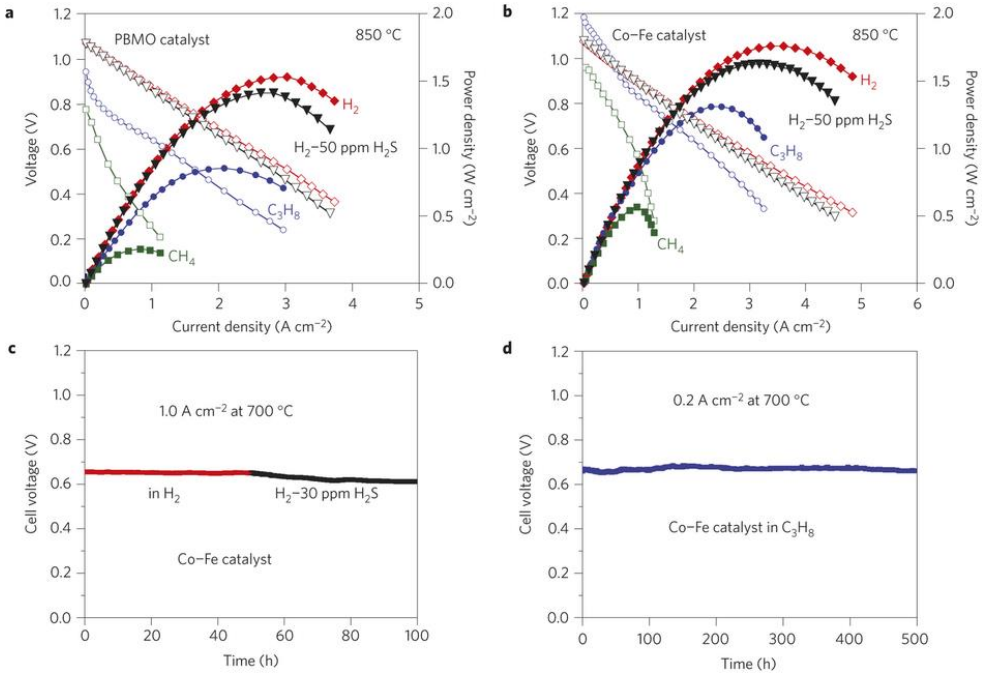

Figure 2.11. (a, b) Current-voltage curves and the corresponding power densities of the layered PBMO anode with (a) layered PBMO catalyst and (b) Co-Fe catalyst using different humidified (3%H_2O) fuels and ambient air as the oxidant at 850°C. (c) short – term stability for a layered PBMO with Co-Fe catalyst under a constant current load of 1.0 A cm^{-2} at 700°C in H_2 and H_2-30 ppm H_2S. (d) Long-term stability test of layered PBMO with Co-Fe catalyst under a constant current load of 0.2 A cm^{-2} at 700°C in C_3H_8.

Besides the anode materials above, $SrVO_3$-based (high electronic conductivity, high resistance to sulfur poisoning, but large volume change during redox),[65] pyrochlore-structured $Gd_2Ti_2O_7$ (good structural stability, but low electrical conductivity) [66] can be also candidate anode materials for SOFC-O^{2-}.

Although numerous novel anode materials have been developed up to date, they always have various deficiencies, especially the inferior catalytic activity towards H_2 reaction compared with Ni. In addition, they only show acceptable electrochemical catalytic activity at elevated temperatures (e.g. $\geq 800^oC$), which is a great challenge for their application at intermediate temperature range. The most widely used anode is still Ni-based cermet materials.

Another point needed to be mentioned is the anode performance in a single SOFC. Generally, it is well known that the overall performance of SOFC is limited by the cathode, rather than anode. Such argument generally works for SOFCs operated at high temperatures. More and more evidences show that the anode can also be performance limiting factor, especially at lower temperatures. Gas diffusion and mass transfer can be seriously hampered by the high tortuosity of the anode. According to the model shown by Chan et al., the effect of concentration polarization in the anode is much greater than that in the cathode of an anode-supported cell and is strongly affected by the hydrogen partial pressure at the reaction sites.[67] Suzuki et al.[68] fabricated tubular fuel cell with Ni-10Sc1CeSZ anode of different porosities, 54, 47, and 37%, respectively after sintered in air. The cell with anode porosity of 54% delivers maximum power densities of 1.1 and 0.5 W cm^{-2} at 600 and 550^oC, respectively, at a linear fuel velocity of 0.8 m s^{-1}. In contrast, the cells with anode of porosity of 47% and 37% shows maximum power density of 0.36 and

0.2 W cm^{-2} at 600°C, respectively. Electrochemical impedance analysis revealed that the gas diffusion is significantly improved by higher porosity and higher linear fuel velocity. Many groups also found that the fuel cell performance can be significantly improved by preparation of anode with phase-inversion method.[69-74] The resultant anode microstructure is asymmetric, containing a thick finger-like porous structure (one finger-like pore has a continuously transition pore size that changes from a few μm to several tens μm) and a thin sponge-like porous structure (homogeneous submicron pores), as shown in Figure 2.12. A single cell with this unique anode structure is successfully fabricated, demonstrating maximum power densities of 0.76, 1.04, 1.32, and 1.97 W cm^{-2} at 650, 700, 750, and 800°C, respectively, with humidified hydrogen (3%H_2O) as fuel and oxygen as the oxidant.[74] The superior cell performance is mainly attributed to the unique anode structure and optimized electrolyte/anode interface. The large and long finger like pores dramatically reduces the gas transport resistance in the anode and homogeneous sponge like pores provide abundant TPBs.

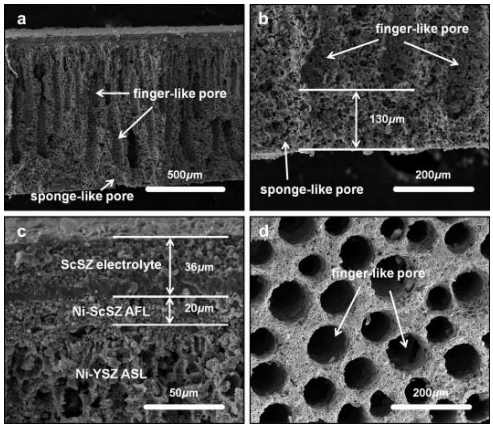

Figure 2.12. Cross-sectional SEM images of the electrolyte/anode half cell after testing. (a) overall view, (b) interface of sponge-like pores and finger-like pores, (c) electrolyte/ anode functional layer/anode support layer interface, (d) surface of finger-like pores.[74]

2.2 Electrolyte materials

The role of electrolyte in SOFC is to separate the anode and cathode and transport oxide ion or proton. According to equation (2-4), the ohmic loss is dominated by the contribution from electrolyte, which can be reduced by reducing the thickness of electrolyte and/or improving the ionic conductivity of electrolyte to achieve desirable performance in IT-SOFC. An ideal electrolyte for SOFC should have high ion transference number close to unity, high ionic conductivity, TEC and chemical compatibility with electrode materials, structural and chemical stability under working conditions. The most widely employed electrolyte materials are fluorite type doped zirconia, ceria, and bismuth oxide, perovskite type doped $LaGaO_3$ as an oxide ion conductor, and doped $BaCeO_3$, $BaZrO_3$, $SrCeO_3$, $SrZrO_3$ as a proton conductor. There are also many other types of electrolyte materials such as pyrocholre $Gd_2Zr_2O_7$, Aurivillius type $Bi_4V_2O_{11}$, hydroxyapatite type $La_{10}(Si/GeO_4)_6O_3$, brownmillerite type $Ba_2In_2O_5$, $La_2Mo_2O_9$ type, Ruddlesden-Popper type $Sr_3Ti_2O_7$, etc. Here fluorite and perovskite type electrolyte materials will be discussed in the framework of this thesis.

2.2.1 Oxide ion electrolytes

2.2.1.1 Fluorite-type electrolyte materials

The stabilized zirconia is the state-of-the-art electrolyte for SOFC due to its high ionic transfer number, high ionic conductivity at high temperature, high structural stability and mechanical strength. The tetragonal/cubic form is stabilized by producing a solid solution with trivalent rare earths ZrO_2-Ln_2O_3 or divalent alkaline earth metals ZrO_2-AO. The maximum ionic conductivity in ZrO_2-based systems is observed when the concentration of the dopant is close to the minimum necessary to completely stabilize the cubic fluorite-

type phase.[75] This concentration (so-called low stabilization limit) and the corresponding conductivity depends on the dopant elements, processing history and microstructural features such as dopant segregation, impurities, kinetically limited phase transition and formation of ordered micro-domains. The most widely used are yttrium-stabilized zirconia (YSZ) and scandium-stabilized zirconia (SSZ). The conductivities of these two electrolytes increase with the degree of substitution to an optimum at 8mol% Y_2O_3 and 11mol% Sc_2O_3. Further addition decreases the ionic conductivity due to increasing association of the oxygen vacancies and dopant cations into complex defects of low mobility, as shown in Figure 2.13.[76] It is commonly accepted that this tendency increases with increasing difference between the host and dopant cation radii. The ideal dopant is scandium considering the ionic radius match but at the expense of high cost. Correspondingly, YSZ is the most widely electrolyte because of the balance of ionic conductivity and cost. However, the problem with YSZ electrolyte is high working temperatures (800-1000^{o}C depending on the thickness of the electrolyte) is needed to obtain acceptable ionic conductivity. Such problem can be partly circumvented by using Sc-doped zirconia owing to its higher ionic conductivity. Nevertheless, the Sc-singly doped zirconia shows aging behavior at moderate temperatures. The co-doping of Sc and Ce significantly improves the structural stability. Lee et al.[77] found that ZrO_2 doped with Sc_2O_3 and CeO_2 did not show any phase transition during heat treatment up to 1250-1550^{o}C and was exceedingly stable as a cubic phase in all temperature ranges. The zirconia co-doped with Sc_2O_3 and CeO_2 showed much higher electrical conductivity than YSZ in the whole temperature range of 300-1100^{o}C and better long-term stability than any other Sc-doped ZrO_2. All these properties render it a good electrolyte material for IT-SOFC.

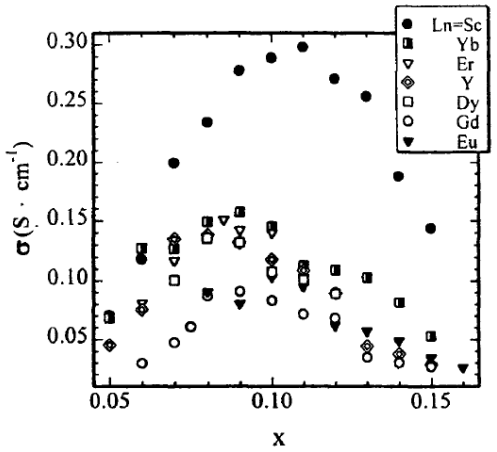

Figure 2.13. Comparison dependence of the electrical conductivity in $(ZrO_2)_{1-x}(Ln_2O_3)_x$ (Ln=lanthanides).[76]

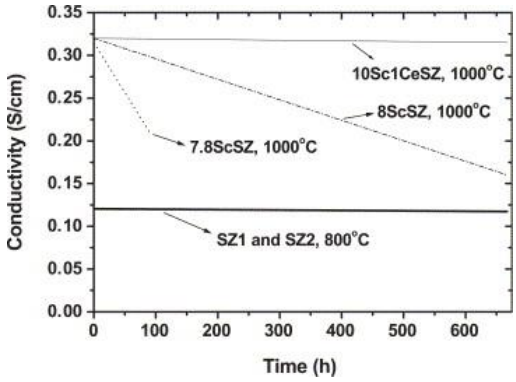

Figure 2.14. Comparison of long-term stability of Sc-and Ce-co-doped ZrO_2 with other Sc-singly doped ZrO_2 and YSZ.[77]

To reduce the ohmic resistance contribution from electrolyte, various techniques[78] have been explored to fabricate thin zirconia electrolyte film so that it can be applied for IT-SOFC, such as dry-pressing, tape-casting, drop coating, dip coating, spin coating, pulsed layer deposition, etc.. It has been shown that when the thickness of YSZ electrolyte film was decreased from 20 to 8 μm, the maximum power density of single cell was improved from 0.46 to 0.57 W cm^{-2} in an anode-supported cell at 700ºC.[79] A balance of ohmic resistance and gas tightness is needed to be taken into account. Wang et al.[80] found that ~10 μm electrolyte film is the best choice for getting high quality electrolyte films which

can meet the requirements of both low ohmic ASR and high OCV; the 10 μm YSZ film was prepared by slurry spin coating.

One concern of the zirconia-based electrolyte is its poor chemical compatibility with many classical cathode materials, such as $La_{1-x}Sr_xCo_{1-y}Fe_yO_{3-\delta}$, $Ba_{1-x}Sr_xCo_{1-y}Fe_yO_{3-\delta}$, $Sm_{1-x}SrCoO_{3-\delta}$, $LnBa_{1-x}Sr_xCo_2O_5$. It always reacts with those materials during fabrication or operation, leading to formation of poorly conductive phases such as $La_2Zr_2O_7$, $SrZrO_3$, $BaZrO_3$. [81, 82] Accordingly, a buffer layer such as Sm- or Gd- doped ceria is needed to alleviate such undesirable reactions,[83-85] which inevitably increases fabrication cost and complexity.

An alternative electrolyte for IT-SOFC is doped ceria. The main advantage of it is a higher ionic conductivity and more compatibility with many cathode materials compared with doped zirconia. The bulk ionic conductivity at 500 ^oC can be as high as 0.01 S cm^{-1}.[86] Eguchi et al. studied the ionic conductivity of ceria doped with Ln-series cations and found that the ionic conductivity increased with increasing ionic radius from Yb to Sm, but decreased at radius larger than 0.109 nm, as shown in Figure 2.15.[87] Similar with doped zirconia, the ceria doped with cations of similar ionic radius shows the highest ionic conductivity, in this case, it is Sm. The optimum doping level is 10-20%. In spite of this, Steele [86] proposed that the highest bulk ionic conductivity of the doped ceria is exhibited by the Gd-doped CeO_2, $Ce_{0.8}Gd_{0.2}O_{1.9}$, which is probably related to the microstructural characteristics. As with all ceramic electrolytes, the grain boundaries are partially blocking ionic transport across them. The high total conductivities found for $Ce_{0.8}Sm_{0.2}O_{1.9}$ might indicate that doping with Sm for some reason tends to induce a lower grain boundary resistance.[88]

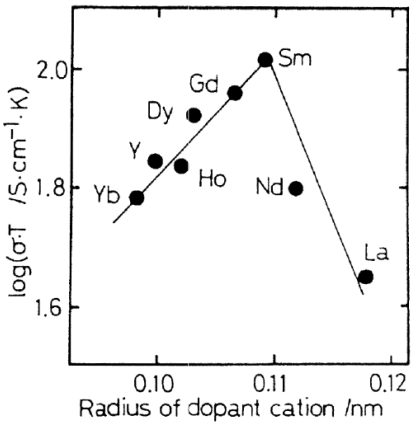

Figure 2.15. Dependence of ionic conductivity for $(CeO_2)_{0.8}(LnO_{1.5})_{0.2}$ at 800°C on a radius of dopant cation.[87]

The main problem associated with the doped ceria electrolytes is the partial reduction of Ce^{4+} to Ce^{3+} under the reducing condition of anode. This has two main disadvantages. First, it induces electronic conduction which causes a partial internal electronic short circuiting in a cell and thus lower cell OCV and efficiency, and second, it generates nonstoichiometry and expansion of the lattice which can pose significant challenges to the mechanical stability of the electrolyte.[75] As shown in Figure 2.16, the electronic conductivity at the anode side is greater than the ionic conductivity at temperatures >550°C.[75] Such issue can be circumvented by depositing a thin layer of zirconia or barium cerate or $LaGaO_3$ at the anode side.[89-92] However, the performance of resultant cells is relatively poor due to the formation of reaction products with low conductivity at the interface between different layers as well as differences in thermal expansion of the electrolytes, resulting in micro-cracks. Correspondingly, doped ceria can only be used as an electrolyte at temperatures of ≤ 500°C.

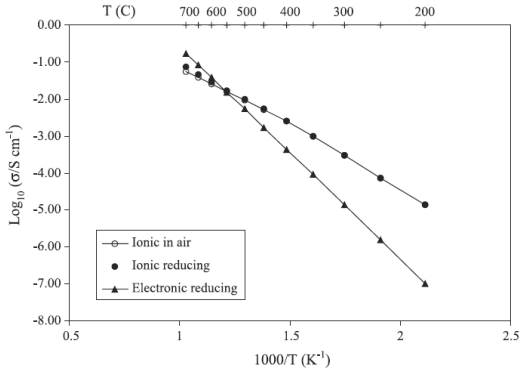

Figure 2.16. Ionic conductivity of $Ce_{0.9}Gd_{0.1}O_{1.95}$ in air and in reducing atmosphere ($10\%H_2$, $2.3\%H_2O$).[75]

Another electrolyte material with the fluorite structure is the Bi_2O_3 family. Different from zirconia and ceria, 25% of oxygen sublattice is empty. Four polymorphs of Bi_2O_3, α, β, γ, and δ-phases, have been reported. Only the cubic δ-phase shows very high conductivity. However, this phase is not stable at lower temperatures; it transforms to low-conductivity monoclinic α-phase at approximately 730°C and melts at its melting point of around 825°C. Correspondingly, a lot of work has been undertaken to stabilize the cubic phase to room temperature. Many scholars studied the structural characteristics and electrical conduction behavior of doped Bi_2O_3. Jiang and Wachsman[93] found that Bi_2O_3 doped by 25 mol% of Dy, Ho, Y, Er, Tm, and Yb exhibited an face-centered cubic (FCC) structure whereas larger-radii rare-earth oxides (Gd throught La) resulted in formation of the rhombohedral phase. The size of the cubic cell was cation-radius dependent, and the lattice parameter increased linearly with increasing cation radius. The electrical conductivity of 20% Er doped Bi_2O_3 (20ESB) can reach as high as 0.41 and 0.021 S cm^{-1} at 800 and 500°C, respectively.[94] Later, Jiang et al. found that Bi_2O_3 co-doped with Dy_2O_3 and WO_3 (DyWSB) exhibits a higher conductivity than that of 20ESB. The conductivity of $(BiO_{1.5})_{0.88}(DyO_{1.5})_{0.08}(WO_3)_{0.04}$ is 0.57 and 0.043 S cm^{-1} at 800 and 500°C, respectively.

[94] Such high conductivity is originated from the high polarizability of the dopants and thus to achieve a stable disordered anion lattice and a high mobility. One of the problems with such Bi_2O_3-based electrolyte is the aging behavior. [93, 95-98] The conductivity of doped Bi_2O_3 decreases with time when it is annealed below 600°C (Figure 2.17). The aging rate is temperature dependent and most rapid around 500°C. Below 500°C, the aging rate is typical of thermally activated processes, increasing with increasing temperature. The electrical conductivity of ESB was decreased by ~25 folds after annealing at 500°C for 100 h. [98, 99] However, above 500°C, the aging rate decreases with increasing temperature. Moreover, at and above 600°C, the conductivity of 20ESB is essentially unchanged with time. [95, 96] For 25 mol%Y-doped Bi_2O_3, however, the conductivity still decreases with time when it is annealed at 650°C. The structural transition from cubic to rhombohedral phase is responsible for the decay at temperatures above 600°C based on XRD results. Both differential scanning calorimetry (DSC) and transmission electron microscopy (TEM) diffraction show that the aging process is related with the ordering of oxygen vacancies by an order-disorder transition below 600°C. Huang et al. [100] found that adding appropriate amount of CeO_2 into Y-doped Bi_2O_3 can inhibit the phase transformation and thus retaining electrical conductivity. Such a Ce- and Y-co-doped Bi_2O_3 showed no sign of degradation in electrical conductivity for ~400 h at 600°C, whereas that of the Y-singly doped Bi_2O_3 declined by about one order of magnitude.

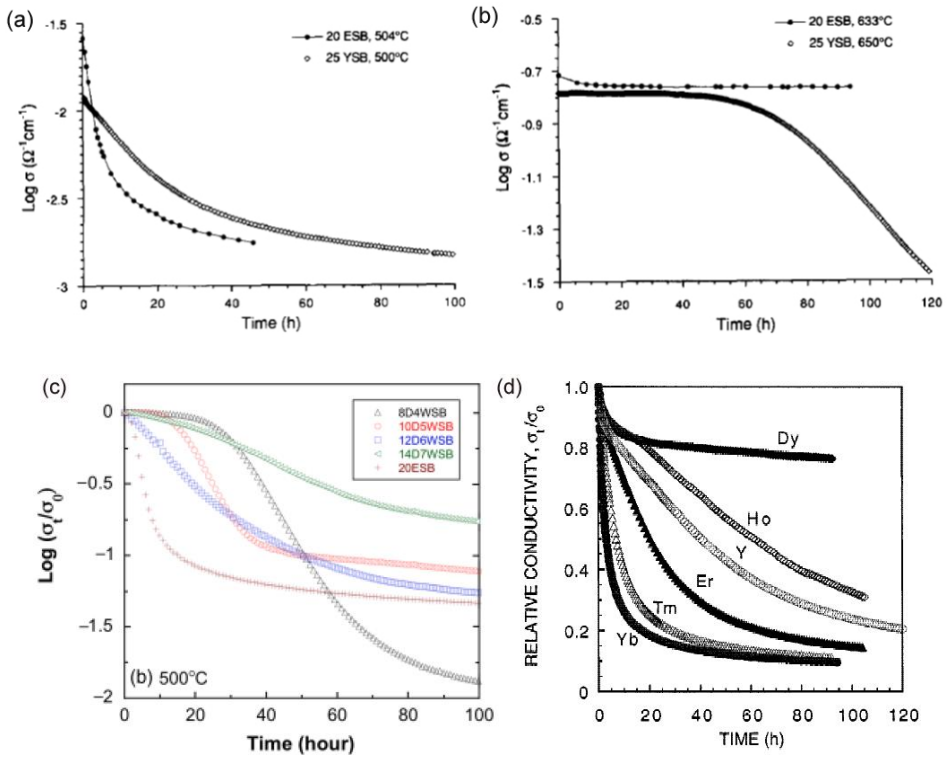

Figure 2.17. Effect of aging at 500°C (a, c, d) and (b) 600°C on conductivity. [93, 97, 98]

A second problem with Bi_2O_3-based electrolyte is that it can be easily reduced to metallic bismuth at the anode operating condition of SOFC.[95] Such issue can be partly overcome by utilizing a bi-layer electrolyte structure, such as GDC/ESB with GDC at the fuel side and ESB at the air side (Figure 2.18a).[101] In this configuration, the ESB layer bocks the electronic conduction from the GDC layer and a sufficiently thick GDC layer prevents decomposition of ESB. As shown in Figure 2.18c, the interfacial *p*(O2) can be controlled by varying the thickness ratio of the two component layers. Thus, the open circuit voltage (OCV) is strongly dependent on the thickness ratio of the two layers. Thicker GDC layer, higher OCV. With the bilayer electrolyte, not only the OCV increases compared with that with GDC single layer, but also the electrochemical activity of the cathode increases, which can be ascribed to the enhanced oxygen dissociation and surface

oxygen exchange rate at the cathode/ESB interface,[102] leading to higher power output (Figure 2.18b). Nevertheless, the lower OCV compared with the theoretical ones still poses significant challenges for the wide application of such bi-layer electrolyte based SOFC. Furthermore, as aforementioned, the long-term stability of electrical conductivity of Bi_2O_3-based materials at temperatures lower than 600°C still needs to be resolved before possible wide application.

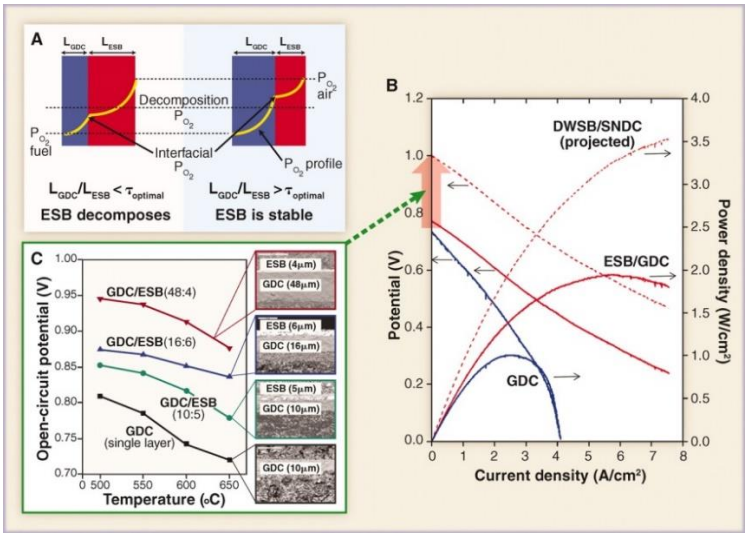

Figure 2.18. (A) Schematic of ceria/bismuth oxide bilayer concept demonstrating the effect of relative thickness on interfacial oxygen partial pressure and ESB stability. (B) I-V and I-P curves for SOFCs with GDC single-layer and ESB/GDC bilayer electrolytes at 650°C using 90 sccm of H_2/3%H_2O as fuel and dry air as the oxidant. With ESB/GDC bilayer electrolyte, a power density of ~2W cm^{-2} at 650°C was achieved because of higher OCV and reduced cathodic polarization. Assuming higher OCV (~1 V) by controlling total thickness and thickness ratio of more conductive DWSB/SNDC bilayer electrolyte, the projected maximum power density is ~3.5 W cm^{-2} under the same conditions. (C) Effect of total thickness and thickness ratio of bilayer electrolyte on OCV.[101]

2.2.1.2 $LaGaO_3$-based electrolyte materials

In 1994, Ishihara et al. reported a completely new perovskite electrolyte LSGM9182 with electrical conductivity slightly lower than Bi_2O_3, wide ionic conduction dominating $p(O_2)$ range (1-10^{-20} atm) and neglegible electronic conductivity.[103] The Goodenough

group later studied the preparation, structural characteristics, and electrical conduction behavior of the $LaGaO_3$-based materials systematically.[104, 105]

The ideal perovskite ABO_3 is cubic structure (Figure 2.19a). The real perovskite structure generally deviates from the ideal cubic structure, the degree of which can be evaluated by tolerance factor *t*,

$$t = (r_A + r_O)/\sqrt{2}(r_B + r_O) \quad (2\text{-}5)$$

where r_A, r_B, and r_O are ionic radius of A, B-site cations, and oxygen anion (1.40 Å), respectively, which are generally Shannon empirical ionic radius. The structure exists as perovskite when *t* is in the range of 0.77-1.1. *t* is unity for ideal cubic perovskite structure with all oxygen atoms being equal. *t* deviates from unity with increasing structural distortion. Meanwhile, the oxygen in the equatorial plane and axis vertex become unequal, which results in the difficulty of oxygen migration and thus lower ionic conductivity. The lattice free volume (V_f) can also exert influence on the migration of oxygen anion, which is defined as the difference between the lattice volume and the sum volume of all composed ions. The larger the V_f, the easier the migration of oxygen anion. The critical radius (r_c) for perovskite is the effective radius of the triangular cavity formed by two A-site cations and one B-site cation, as shown in Figure 2.19b, which can be theoretically calculated according to

$$r_c = \frac{-r_A^2 + \frac{3}{4}a^2 - \sqrt{2}ar_B + r_B^2}{2r_A + \sqrt{2}a - 2r_B} \quad (2\text{-}6)$$

where r_A, r_B and *a* are ionic radius of A, B-site cations and the lattice parameter, respectively. Generally, r_c does not exceed 1.10 Å, less than the ionic radius of oxygen

anion (1.40 Å). The larger the r_c, the easier the oxygen migration. Thus, the oxygen anion must relax during migrating across this critical cavity, which contributes to the main activation energy.

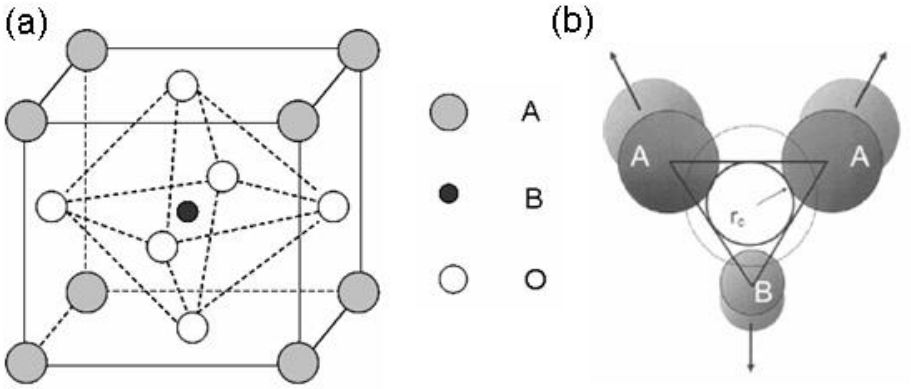

Figure 2.19. Perovskite structure (a) and its corresponding critical radius (b).

Hayashi et al. summarized the electrical conductivity of reported perovskite type electrolytes and analyzed the relationship between electrical conductivity and structural parameters. They found that the maximum electrical conductivity can be achieved at $t \approx 0.96$ with $LaGaO_3$-based material.[106] Theoretical calculation revealed that Sr and Mg are the best dopants for La and Ga-sites, respectively. Cu^{2+} and Hg^{2+} can also be candidate dopants for Ga-site.[107] One of the advantages of the $LaGaO_3$-based materials is their high ionic conductivity. The ionic conductivity depends on the doping level at the La and Ga sites. As shown in Figure 2.20,[104] the region of highest oxide ion conductivity falls in the ranges of $0.125 \leq x \leq 0.25$ and $0.125 \leq y \leq 0.25$ at 800°C, which shrinks differently along the x and y axis to the ranges $0.15 \leq x \leq 0.20$ and $0.125 \leq y \leq 0.175$ at 702°C and $0.145 \leq x \leq 0.16$ and $0 \leq y \leq 0.06$ at 595°C. The highest conductivity ionic conductivity was found in $La_{0.8}Sr_{0.2}Ga_{0.83}Mg_{0.17}O_{3-\delta}$, 0.166, 0.079, and 0.026 S cm^{-1} at 800, 702, and 595°C, respectively.[104] Slight cobalt doping can further increase the electrical conductivity of

$La_{0.8}Sr_{0.2}Ga_{0.8}Mg_{0.115}Co_{0.085}O_{3-\delta}$ with negative influence on the electrolytic domain.[108] One disadvantage for $LaGaO_3$-based material is it is rather hard to prepare pure phase, $SrLaGa_3O_7$ and $La_4Ga_2O_7$ always exist as impurities.[104] It is worth noting that LSGM is a good proton conductor with protonic conductivity of 0.014 S cm^{-1} at 600°C in water vapor containing H_2 atmosphere.[109]

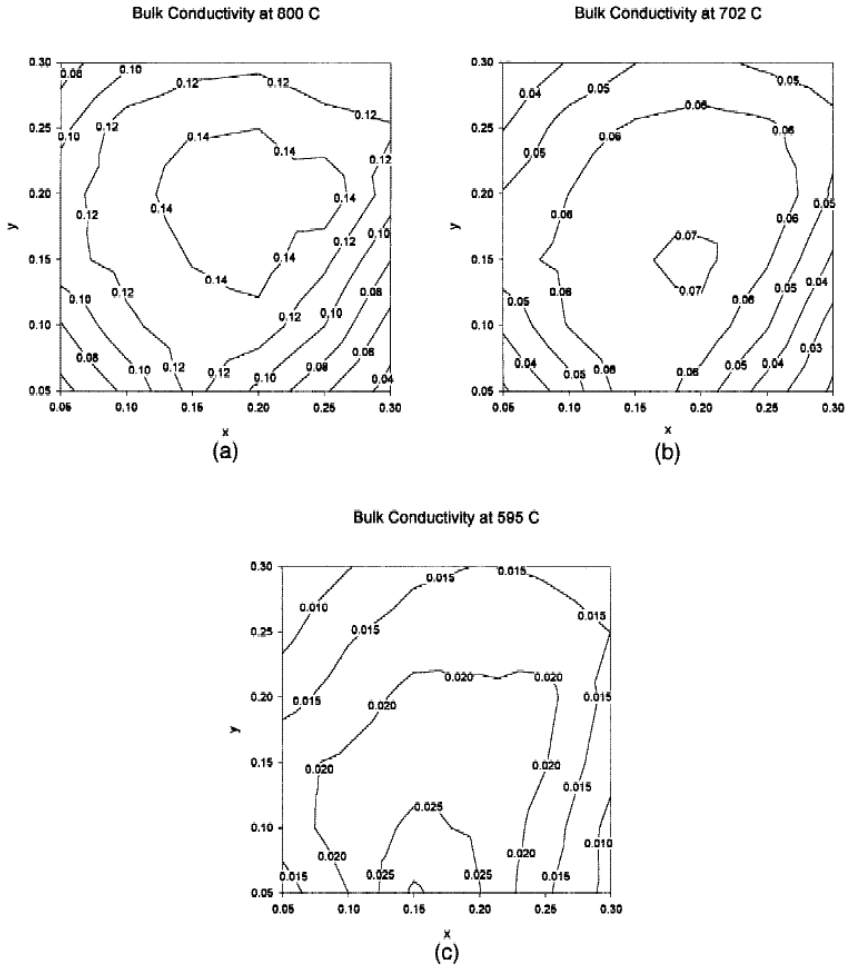

Figure 2.20. Isoconductivity diagram of $La_{1-x}Sr_xGa_{1-y}Mg_yO_{3-0.5(x+y)}$.[104]

2.2.1.3. Hydroxyapatite based electrolyte

Hydroxyapatite type electrolyte materials are attracting increasing attention in very recent years. The ideal general formula for hydroxyapatite is $(M_1,M_2)_{10}(XO_4)_6O_2$ with $La_{10}(SiO_4)_6O_3$ showing higher electrical conductivity.[110] Compared with the general

formula, there are excess positive charges at the M_1 and M_2 sites in $La_{10}(SiO_4)_6O_3$, which can be compensated by oxygen anion. Because all the normal oxygen sublattices have been occupied, the excess oxygen anion can only be accommodated in the interstitial sites. It is these interstitial oxygen anions that are responsible for oxygen ionic conduction in hydroxyapatite, which is different from the oxygen vacancy mechanism in the oxide ion electrolytes discussed above. The $La_{10}(SiO_4)_6O_3$ structure is composed of isolated SiO_4 tetrahedrons with La^{3+} and O^{2-} distributing along special directions, as shown in Figure 2.21a.[111] Two channels are formed with the distribution of SiO_4 tetrahedrons; the larger one is occupied by La1 and O4, the smaller one La2. The neutron diffraction revealed that the excess oxygen reside at the normal oxygen sites along [001] direction and the near interstitial sites. In addition, not all the normal oxygen sublattices are occupied; there are still some oxygen vacancies.

The electrical conductivity of hydroxyapatite with perfect stoichiometry is very low. High electrical conductivity can only be achieved by deviating from the stoichiometry. The electrical conductivity of materials of this family is very sensitive to the stoichiometry of cations and anions. Generating La vacancy in La2 channel,[111, 112] doping Sr at La-site,[113] partial replacing Si with Al and Fe[114] can improve the electrical conductivity. The electrical conductivity of Al doped $La_{9.5}(Ge_{5.5}Al_{0.5}O_{24})O_2$ was 0.16 S cm^{-1} at 800 ^oC and its oxygen ionic transference number is higher than 0.99 over the $p(O_2)$ range of 0.21 -10^{-20} atm.[114] The results of atomic simulation showed that the electrical conductivity of La-deficient $La_{9.67}(SiO_4)_6O_2$ is high with low activation energy because the oxygen anions migrate through the interstitial mechanism along the c-axis in the form of sinusoidal wave, as shown in Figure 2.21b.[111]

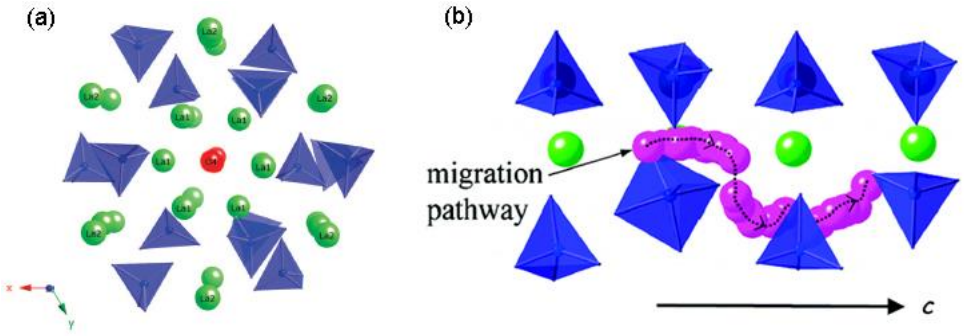

Figure 2.21. Schematic structure of $La_{9.67}(SiO_4)_6O_{2.5}$ (a) and interstitial oxygen migration routes (b).[111]

From the perspective of commercial applications, SOFCs based on CeO_2-based and CeO_2-based/Bi_2O_3-based bilayer electrolytes are less attractive due to their intrinsically high electronic conduction and mechanical issues upon exposure to reducing atmospheres although they show excellent performance in lab-scale button cells [101, 115]. The LSGM-based SOFCs face the same problems given its high cost, high chemical reactivity with conventional electrode materials, and low mechanical strength [116-118]. Therefore, ZrO_2-based SOFCs still remain the main stream of commercial SOFCs development, although their ionic conductivity is lower compared with other oxide ion conductors, as shown in Figure 2.22.

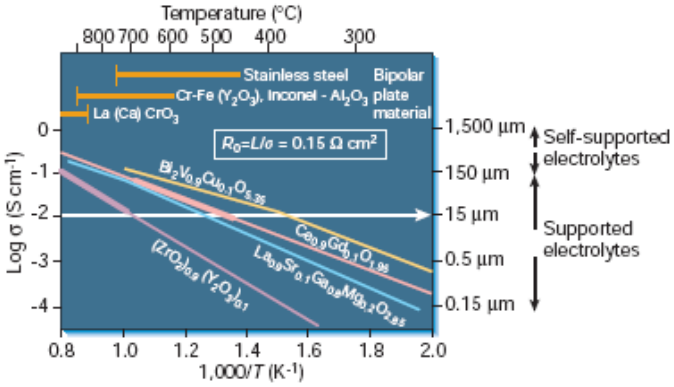

Figure 2.22. Comparison of several oxygen ionic conducting electrolytes.[17]

2.2.2 Proton conducting electrolytes

Different from the oxide ion defects, the proton defect is not inherent in the high temperature protonic conductors (HTPC), which can be introduced from the surrounding hydrogen and water vapor. The protonic defect does not exist as single proton, but in the electron cloud of oxygen denoted as $OH_O^{\cdot}$. The defect reactions are:[119-121]

$$H_2+2O_O^{\times}+2h^{\cdot}=2OH_O^{\cdot} \quad (2\text{-}7)$$

$$H_2O+V_O^{\cdot\cdot}+O_O^{\times}=2OH_O^{\cdot} \quad (2\text{-}8)$$

Increasing results show that the protonic defect is mainly generated according to (2-8). The existence of oxygen vacancy is paramount for the formation of protonic defect, which can be introduced by doping with cations of lower valence. Take $BaCeO_3$ as an example,

$$M_2O_3 \xrightarrow{2BaCeO_3} 2Ba_{Ba}^{\times}+2M_{Ce}^{'}+V_O^{\cdot\cdot}+8O_O^{\times} \quad (2\text{-}9)$$

In the ideal case, there should be

$$[OH_O^{\cdot}]=[M_{Ce}^{'}] \quad (2\text{-}10)$$

Because the water vapor takes part in the hydration reaction (eqn. 2-8), $p(H_2O)$ is believed to have an influence on the protonic conductivity; oxygen ionic conduction appears in dry conditions. Due to its exothermic nature, the protonic concentration decreases, concentration and mobility of oxygen ionic defect increase with increasing temperature, resulting in decreased protonic conductivity and increased oxygen ionic conductivity, which is more significant in $BaCeO_3$-based materials probably related with structural symmetry.[122] At high $p(O_2)$, electronic hole also appears, but the electronic conduction is very limited at low temperature and in water vapor-containing atmospheres. Four types of charge carriers can co-exist in the proton conductor. Bonanous and his

colleagues [123, 124] proposed a numerical solution of the concentration of those charge carriers for arbitrary oxygen and water vapor partial pressures and the results are shown in Figure 2.23.

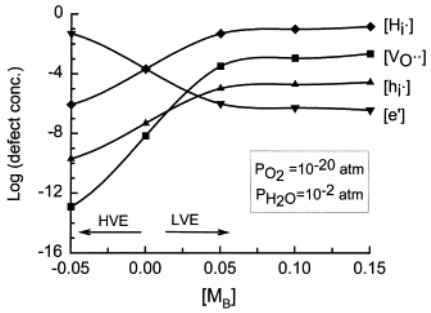

Figure 2.23. Simulated concentrations of four defects for an extended range of doping levels with high valence element (HVE) and low valence element (LVE).[124]

The variation of electrical conductivity with $p(O_2)$ can be expressed as

$$\sigma = \sigma_{ion}^{0} + \sigma_{n}^{0} p_{O_2}^{-1/4} + \sigma_{p}^{0} p_{O_2}^{1/4} \qquad (2\text{-}11)$$

where σ and σ_{ion}^{0} are total and ionic conductivity, respectively. σ_{n}^{0} and σ_{p}^{0} are *n* (*q*) and *p*-type conductivity at $p(O_2)$ of 1 atm, respectively. Such electrical conduction behavior of HTPC has been extensively proved by experiments.[124-126] As shown in Figure 2.24,[124] the electrical conductivity increases with $p(O_2)$ when $p(O_2)$ is higher than 10^{-5} atm, typical *p*-type conduction behavior. The protonic conduction dominates over $p(O_2)$ of $10^{-20} \sim 10^{-5}$ atm. The electrical conductivity increases with decreasing $p(O_2)$ over $p(O_2)$ of less than 10^{-20}; there are controversies about the conduction mechanism in this $p(O_2)$ range. Most investigators ascribed it to electronic conduction but Phillips et al. suggested it was still dominated by protonic conduction.[125] The thermoelectric power investigation on $SrCe_{0.95}Y_{0.05}O_{2.975}$ showed that the conduction mechanism in this $p(O_2)$ range was the same with that dominated by ionic conduction, and the electrical conductivity exhibited isotopic effect,[124, 127] which is a strong evidence of protonic conduction.

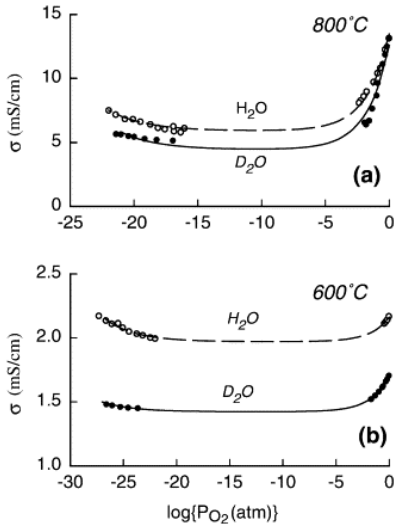

Figure 2.24. Conductivity in $Sr_{0.995}Ce_{0.95}Y_{0.05}O_{\xi}$ in $N_2/O_2/H_2O$ and $N_2/H_2/H_2O$ atmospheres and the corresponding deuterium containing ones measured at two temperatures. The partial pressures of H_2O or D_2O vapour were maintained at about 0.01 atm.[124]

However, there is no consensus on the proton conduction mechanism in HTPCs. The general mechanisms include: proton migration according to Grotthus mechanism at low temperature, which is replaced by Vehicle mechanism with increasing temperature. At very low temperature (lower than Debye temperature), the local tunning mechanism dominates. It is dominated by the Grotthus mechanism at the working temperature of intermediate temperature SOFC.[128, 129] According to this mechanism, the proton migrates from one oxygen to another by means of lattice vibration, as shown in Figure 2.25.[130]

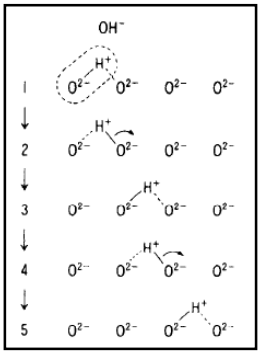

Figure 2.25. Grotthus mechanism for proton migration. [130]

Kreuer[119] proposed that the migration of proton includes two steps, i.e., rotational diffusion of protonic defect and the transfer to oxygen nearby. That is, only proton exhibits long-range diffusion while oxygen remains at their original lattice site, as shown in Figure 2.26.[119] Several experimental results[131, 132] and quantum molecular dynamic simulation[133, 134] showed that the rotational diffusion is very fast; the transfer between oxygens is the rate-determining step (RDS). For example, the time-scale for rotational diffusion is 10^{-12}-10^{-13} s whereas it is 10^{-9} s for proton transfer. [134, 135] However, the infrared spectra results of $BaZrO_3$-based materials inferred that the proton transfer is the RDS.[135] Later, Gomez et al.[136] studied the influence of octahedron distortion on proton location and transition state in $BaTiO_3$, $BaZrO_3$, $CaTiO_3$ and $CaZrO_3$. They proposed that the O-O distance decreased with increasing octahedron distortion, which facilitated the proton migration through new routes such as inter-octahedron, while the proton transfer between oxygens is still the RDS.

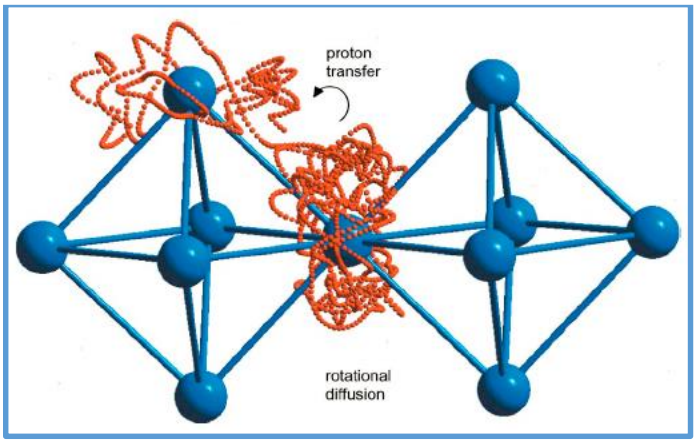

Figure 2.26. Proton migration includes rotational diffusion and proton transfer between oxygen atoms. [119]

2.2.2.1 Ba/$SrCeO_3$-based proton conductors

$SrCeO_3$ and $BaCeO_3$-based materials are the earliest studied perovskite proton conductors by Iwahara et al. in 1980s.[120, 121] Because the smaller lattice parameter and

higher lattice distortion, the migration of proton in $SrCeO_3$ is more difficult than that in $BaCeO_3$.[119] But the former exhibits higher proton transference number. The electrical conductivity of $BaCeO_3$ was widely studied. Various dopants have been employed to increase the protonic conductivity, such as Y, Sm, Gd, Nd.[121, 137-141] The electrical conductivity of 20%Sm-doped $BaCeO_3$ is 0.017 S cm^{-1} at 600°C in wet 5%H_2/Ar.[142] The electrical conductivity is very sensitive to preparation procedures. Many controversies exist in literature on the electrical conductivity even for samples with nominally identical compositions. Stevenson et al. reported that the electrical conductivity of Gd-doped $BaCeO_3$ decreases at a doping level of higher than 15%,[138] whereas Taniguchi et al. observed that the electrical conductivity of similar materials increased with dopant content up to 25%.[137] These discrepancies may originate from the differences in processing procedures (1600°C for Stevenson et al. vs. 1650°C for Taniguchi et al.), which results in subtle variations in microstructure and composition, and in turn influences the conduction behavior. Many studies have been performed on the influence of stoichiometry on electrical conductivity. Ma et al. found that the electrical conductivity of Ba-deficient $Ba_{0.95}Ce_{0.9}Y_{0.1}O_{3-\delta}$ was higher than that of stoichiometric and Ba-excess composition.[139] Similar result was reported by Kikuchi et al. on $Ba_{0.975}Ce_{0.8}Gd_{0.2}O_{3-\delta}$.[140] However, Shima and Haile reported that the Ba-excess Gd-doped $BaCeO_3$ showed the highest electrical conductivity.[141] The reasons are unclear while the migration of doping elements from B- to A-site will reduce the concentration of oxygen vacancy and thus lower conductivity. Regarding to whether the doping element is at the A- or B-site, the theoretical calculation indicated that smaller dopant such as Yb, Y, Gd has a greater tendency to reside at the Ce-site whereas larger dopant such as La tends to reside at the Ba-site. Nd is an amphibious

element, residing at both Ce and Ba sites.[143-145] Wu et al.'s results based on extended X-ray absorption fine structure confirmed the theoretical calculation.[146]

The main problem with cerate-based proton conductors is their poor chemical stability in acidic gas and water containing atmospheres, forming carbonate and hydroxides according to

$$BaCeO_3+CO_2=BaCO_3+CeO_2 \quad (2\text{-}12)$$

$$BaCeO_3+H_2O=Ba(OH)_2+CeO_2 \quad (2\text{-}13)$$

The low chemical stability of $BaCeO_3$ is related to its high basicity on one hand; on the other hand, $BaCeO_3$ itself is thermodynamically unstable, which decomposes into BaO and CeO_2 at temperatures lower than 631°C.[147] The reaction with CO_2 and H_2O is not only associated with thermodynamic factors, but also dynamic factors. The experimental results with reaction of powdered BCY10 with CO_2 are in accordance with the above thermodynamic prediction. The stability of dense BCY10 electrolyte, which is covered by electrode, was improved.[148] The cell voltage degradation rate of single cell with $BaCe_{0.8}Gd_{0.2}O_{3-\delta}$ electrolyte was 24%/1000 h with 80% H_2/ 20% CO_2 as fuel but it was only 7%/1000 h with pure H_2 as fuel under a discharge current density of 100 mA cm^{-2} at 800 °C.[149] The reaction of $BaCeO_3$ with H_2O is also associated with the form of water (gas vs. liquid). The 20 mol% Gd-doped $BaCeO_3$ was observed to be stable in water vapor at 600 and 700°C for 1000 h but unstable when heated in water at 85°C with the formation of $Ba(OH)_2$.[150] Bhide and Virkar studied the reaction of $BaCeO_3$ with H_2O in detail.[151] In water vapor, the $BaCeO_3$ was covered with the reaction product. The water vapor must enter the lattice, which is a sluggish step, to achieve further reaction. Therfore, the enter of water vapor into the lattice is to introduce protonic defects rather than damage the chemical

stability although strucutral viariations are possible. In liquid water, however, the produced $Ba(OH)_2$ can be dissolved in water; meanwhile, its porous structure cannot prevent the further reaction with H_2O, which is an interface controlled process. Accordingly, the chemical stability in liquid water is much worse.

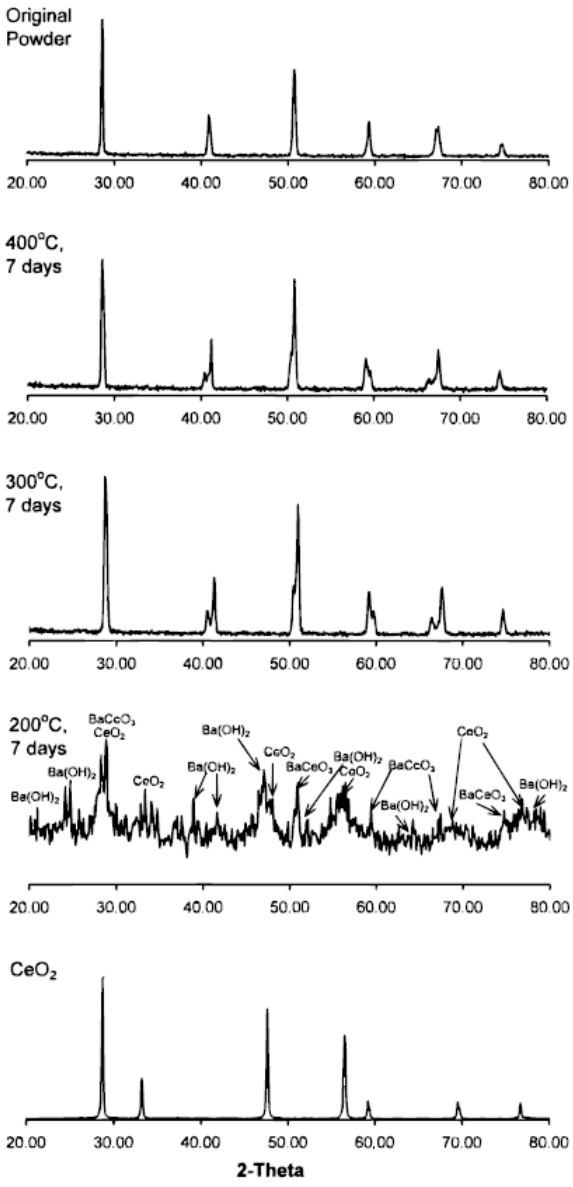

Figure 2.27. A comparison of the XRD patterns of 20 mol% Gd-doped $BaCeO_3$ powder exposied to water vapor over a range of temperature, with the origianal as-calcined powder.[151]

The chemical stability of $BaCeO_3$-based materials can be enhanced by partical replacement of Ce with elements of higher electronegativity such as Zr, Zn,[152] Nb,[153] In.[154] For example, the $BaCe_{0.5}Zr_{0.3}Y_{0.16}Zn_{0.04}O_{2.88}$ remained stable after the TGA measurement in pure CO_2 up to 1200°C while its total conductivity in wet 5% H_2 was 3.14 mS cm^{-1} at 400°C and over 10 mS cm^{-1} above 600°C.[152] An accompanying issue with improved chemical stability is reduced electrical conductivity. The electrical conductivity decreased by one order of magnitude for In-doped $BaCeO_3$ compared with Y-doped $BaCeO_3$, although the former exhibits higher stability and solubility.[154]

2.2.2.2 Ba/$SrZrO_3$

Compared with cerates, the zirconates show better chemical stability. $BaZrO_3$ is the cubic perovskite with the highest lattice constant. The high structural symmetry, large lattice constant (>0.42 nm for Y-doped $BaZrO_3$ (BZY)), and the covalency of the Zr/O bond reduced the Zr/H-repulsive interaction and therefore higher mobility of protonic defects. Yttrium is found to be the best dopant for $BaZrO_3$ because Y-doping does not perturb the electronic distribution of oxygen, i.e., the basicity of oxygen remains constant, in spite of the large ionic radius difference between Y^{3+} and Zr^{4+} (0.89 vs. 0.74 Å). The Y-doped $BaZrO_3$ shows the lowest activation energy and the activation energy does not change with doping level. [119] High proton mobility and entropically stabilized protonic defects, even at high dopant level, lead to the enormous proton conductivity of this material. At temperatures below about 700°C and a water partial pressure of 23hPa, its bulk conductivity exceeds the oxide ion conductivity of the best oxide ion conductors (Figure 2.28).[119] The high bulk protonic conductivity, high chemical stability, and a wide ionic domain make BZY an interesting parent compound for SOFCs.

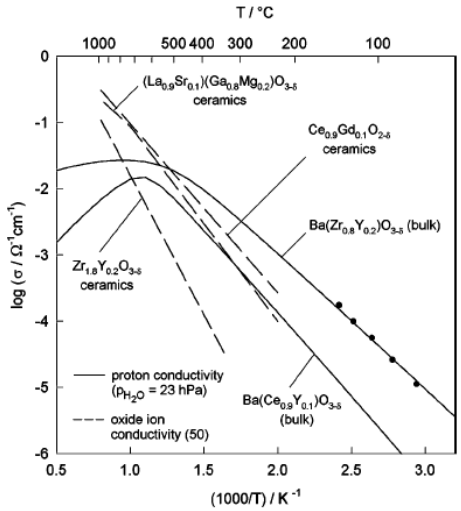

Figure 2.28. Bulk conductivity of 20Y:$BaZrO_3$ compared with the proton conductivity of 10Y:$BaCeO_3$ and the oxide ion conductivity of the oxide ion conductors.[119]

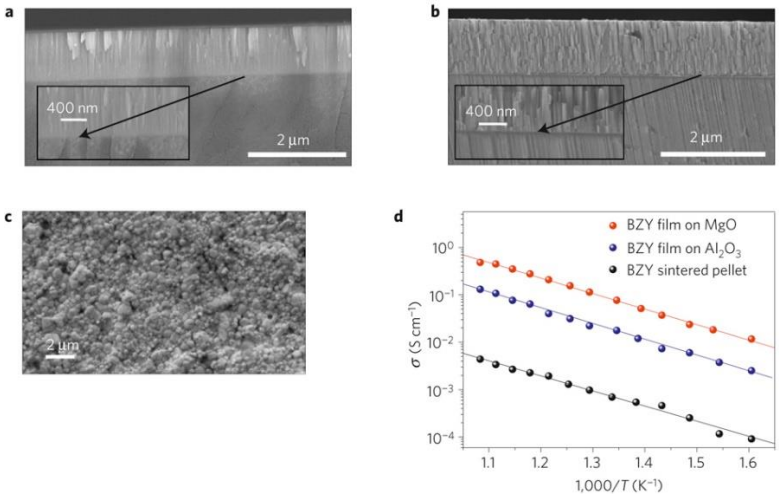

Figure 2.29. (a-c) Cross-section FE-SEM images of a BZY film on MgO (a), on sapphire (b) prepared by pulsed layer deposition (PLD) and a BZY sintered pellet (c). (d) The Arrhenius plots of the conductivity measured in wet 5%H_2/Ar for the three samples. The highly textured grain boundary-free BZY film grown on the MgO substrate presents conductivity values about two orders of magnitude larger than the total conductivity of sintered pellets of the same material.[155]

The greatest challenge facing this material is its poor sinterability, leading to huge grain boundary resistance and thus low total electrical conductivity, 1-4 orders of magnitude lower than the bulk conductivity (Figure 2.29).[119, 155] Correspondingly, a lot of work has been devoted to improve the sintering activity of this material. Tao and Irvine [152]

found that addition of ZnO can significantly improve the sintering process. They studied the shrink behavior of BZY20 with and without ZnO (Figure 2.30). Both samples started shrinking at ~1000^{o}C; however, with ZnO addition, shrinkage is accelerated and most notably a second, faster sintering mechanism initiates just below 1300^{o}C. The total shrinkage of the ZnO-added sample was 15.17%, which is almost ten times that of BZY20 (1.76%). After sintering at 1325^{o}C for 10 h, the BZY20 was quite porous, with ~68% relative density compared to the ZnO-added sample (96% relative density). Elemental analysis revealed that zinc is uniformly distributed in the sample. The enhanced sintering probably proceeds through a liquid-assisted process, which facilitates the diffusion of atoms.[156, 157] Furthermore, the ZnO addition improves the chemical stability of BZY samples. Tong and his group members proposed a reactive sintering to try to combine the phase formation, densification, and grain growth into single high-temperature sintering step.[158, 159] They studied a series of transition elements and found that NiO, ZnO, CoO and CuO are effective.[159] Further study reveals that the rapid and full densification of NiO-modified BZY pellets at relatively temperature of 1350^{o}C is due to the formation of the impure phase BaY_2NiO_5 and its subsequent role as a sintering aid. The dramatic further growth after densification is facilitated by the partial decomposition of the BaY_2NiO_5 (located primary at the grain boundaries) and its incorporation into the cubic perovskite structure of BZY.[158] Duan et al. fabricated single SOFC by such solid state reactive sintering with addition of NiO in one step and achieved very promising performance.[160] However, a potential problem with such approach is very possible introduction of electronic conduction and even short circuiting in the electrolyte due to the reduction of NiO to Ni metal.

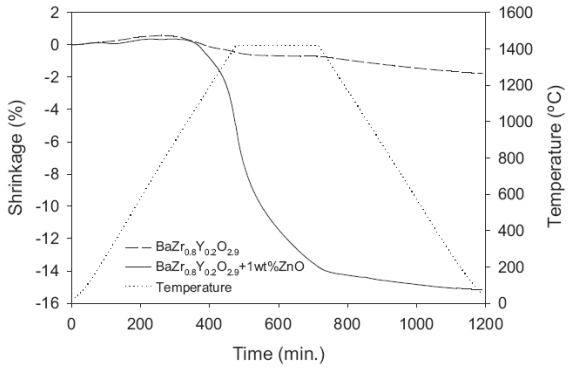

Figure 2.30. Shrinkage of green 13 mm diameter cylinders about 10 mm in length of $BaZr_{0.8}Y_{0.2}O_{3-\delta}$ and $Ba_{0.97}Zr_{0.77}Y_{0.19}Zn_{0.04}O_{3-\delta}$ as a function of firing temperature. The samples were heated at 3°C min^{-1} from room temperature to 1450°C, held isothermally at 1450°C for 4 h, and cooled down at 3°C min^{-1} to room temperature.[152]

Besides addition of sintering aid, Fabbri et al.[161] reported that by doping Pr in BZY can significantly enhances its sinterability without impairing the chemical stability. The shrinkage of $BaZr_{0.7}Pr_{0.1}Y_{0.2}O_{3-\delta}$ (BZPY02) started at about 950°C, which is around 200°C lower than that of the shrinkage onset for the BZY pellet. At 1600°C, the final shrinkage for BZPY02 was almost doubled that reached for BZY (11.5%), this same shrinkage value was already obtained at about 1350°C for BZPY02. The Haile group developed a fabrication protocol based on chemical solution synthesis of precursor materials and subsequent reactive sintering to obtain large grained BZY20.[162] A combination of incomplete calcination, such that some amount of barium carbonate remains prior to sintering and nanometric powders of the perovskite phase appears to be necessary for enhanced grain growth. The sample with grain size of 1 μm provides total electrical conductivity of 0.01S cm^{-1} at 400°C, very close to the bulk conductivity. However, this process needs very careful control of the synthesis procedure, which is not applicable for wide application. Based on the results above, addition of sintering aid seems to be the most effective strategy to obtain dense BZY samples at lower temperatures.

Considering that the $BaCeO_3$-base materials exhibit lower chemical stability but higher electrical conductivity whilst $BaZrO_3$-based materials higher chemical stability but lower electrical conductivity, it is natural to prepare $BaCeO_3$-$BaZrO_3$ solid solution to obtain better performance.[163-166] The Zr content is generally 40 mol% for Y-doped $BaCeO_3$ to obtain desirable stability.[165] $BaCe_{0.2}Zr_{0.6}Gd_{0.2}O_{3-\delta}$ and $BaCe_{0.4}Zr_{0.4}In_{0.2}O_{3-\delta}$ remained stable for 200 h in boiling water, 4000 h in water vapor [166] The partial replacement with Zr improves the chemical stability, but the electrical conductivity decreases due to reduced lattice volume.[163, 165] Zuo et al.[164] reported that BCZY712 showed excellent stability in 2% CO_2 for 168 h at 500°C. However, their testing condition is relatively mild, which cannot be compared with other reports. Later study found that BCZY712 can still react with 3% CO_2 at 600°C for only 3 h.[167] The very recent report found that the resistance of BCY20 to CO_2 can be greatly improved by coating with a layer of BZY (~ 600 nm in thickness) by pulsed layer deposition without impairing the electrical conductivity, [168] which provides a new approach to modify the chemical stability.

Besides cerate and zirconates, there are other types of proton conductors. Their properties are summarized in Table 2.1.

Table 2.1 Properties and current research status of several HTPCs.

HTPC	Properties	Research status
$BaCeO_3$-based	High protonic conductivity; relatively high mechanical strength; phase transition orthorhombic-trigonal-cubic from low to	The most studied HTPC since 1988, its structure, protonic conduction behavior and chemical stability has been systematically investigated; no concensus on

	high temperature; poor chemical stability.	influence of factors on the protonic conduction behavior; advanced techniques such as EXAFS are being empolyed to study its protonic conduction properties; improving its chemical stability is still a hotspot.
$BaZrO_3$-based	High bulk conductivity; excellent chemical stability; difficult to densification due to its refractory nature; small grain size and thus large grain boundary resistance.	Kreuer reported that its bulk conductivity was very high, it is an actively studied material now. Adding sintering additive such as ZnO, co-doping, reactive sintering, PLD, synthesizing nanopowders [174], etc. have been used to obtain dense samples with large grains. The grain boundary conduction is determined by space charge layer .
$SrCeO_3$-based	High protonic transference number; low electrical conductivity; poor chemical stability	The first perovskite material that was found to exhibit protonic conduction. There is less research on it because its low electrical conductivity.
$Sr/CaZrO_3$-based,	Low protonic conductivity; good chemical	Less study on them in recent years;, but they can emploed for

$Ba/Sr/CaTiO_3$-based	stability	mechanism study.
$LaNbO_4$-based	Low protonic conductivity	Proposed by Norby et al. in 2006. The present research focuses on how to improve its conductivity and structural characteristics.
$La_2Zr_2O_7$-based	Low protonic conductivity; difficult to densification	To improve its protonic conductivity.
$Ba_3Ca_{1.18}Nb_{1.82}O_{9-\delta}$	High protonic conductivity; good chemical stability; low dehydration temperature	Many researches on it in the following several years sinced it was first reported in 1994, much lesss reports on it now.

2.3. Cathode materials

The porous cathode of SOFCs functions as a catalyst to reduce molecular oxygen to oxygen ions while conducting electrons. First, molecular oxygen diffuses into porous structure and adsorb on the surface of cathode. Due to the conducting nature of cathode material, the adsorption will take place on electrode/gas interface (DPBs) or electrolyte/electrode/gas interface (TPBs). This step requires a high surface area with sufficient porosity in order to ensure a rapid diffusion of molecular oxygen and adsorption rate. Second, the adsorbed oxygen species is reduced by the electrons in the cathode. This step requires the cathode to possess high electronic conductivity, for example, higher than

100 S cm^{-1}[169]. After molecular oxygen is fully reduced to oxide ions, the third step is the transport of oxide-ion through the cathode/electrolyte interface and incorporate into electrolyte lattice. The overall ORR can be expressed by:

$$O_2(g) + 4e' + 2V_O^{\cdot\cdot} = 2O^{2-} \quad (2\text{-}14)$$

Furthermore, the cathode materials should have a good thermal expansion coefficient (TEC) match with the electrolyte. Since the fabrication and operation undergo repeated heating and cooling processes, the cathode/electrolyte interface can subject to a large internal stress if a mismatch TEC exists. This internal stress can further cause delamination between cathode and electrolyte, which leads to severe cathode performance degradation over time [170]. Also, the cathode materials should have good chemical compatibility with other cell components, especially the electrolyte. Once reaction happens between the cathode and electrolyte, the product may affect charge transfer by introducing an additional resistance, which also degrades performance [171]. The tolerance of cathode materials to environmental impurities is critically important to real-world operation of SOFC stacks. For instance, Cr contamination from metal interconnects (such as stainless steel) at elevated temperatures can poison the cathode performance via a well-established Cr-vapor transport and oxidation/reduction mechanism [172].

2.3.1 ORR mechanism

There are two possible pathways for ORR depending on the nature of cathode materials. One pathway is the surface of cathode. Molecular oxygen is adsorbed and travels along the surface of cathode to reach the electrolyte/electrode/gas interface (TPBs) where ORR takes place. Surface pathway is almost the only way to reduce oxygen for a poor ionic conductor, such as LSM, since they lack of sufficient oxygen vacancy to transport the oxide

ions. Another pathway is the bulk, which happens on MIEC cathodes. For MIEC cathodes, after the adsorption of molecular oxygen, adsorbed oxygen species can be reduced on the entire electrode/gas surface (DPBs) and the formed oxide ions can travel through the bulk of cathode to arrive at the interface of cathode and electrolyte. It is noteworthy that MIEC can have both pathways in parallel to reduce oxygen molecules. Therefore, MIEC is the promising candidate for IT-SOFCs. The above two transport mechanism are shown in Figure 2.31. A popular ORR mechanism with several elementary steps can be viewed as[173]:

$$O_{2(g)} \leftrightarrow 2O_{ad} \tag{2-15}$$

$$O_{ad} + e' \leftrightarrow O'_{ad} \tag{2-16}$$

$$O'_{ad} \leftrightarrow O'_{TPB} \tag{2-17}$$

$$O'_{TPB} + e' \leftrightarrow O^{2-}_{TPB} \tag{2-18}$$

$$O^{2-}_{TPB} + V^{\cdot\cdot}_{O,electrode} \leftrightarrow O^{\times}_{O,electrolyte} \tag{2-19}$$

The reaction models of different cathode materials are illustrated in Figure 2.31.[174] To reduce the cathode polarization loss, the most effective approach is to increase the oxygen ionic and electronic conductivity of cathode materials, leading to larger TPBs and thus higher catalytic activity, which can be achieved by the use of MIEC and/or composite cathodes composed of electronic conducting and oxygen ionic conducting phases. An ideal cathode material should also have good chemical and TEC compatibility with the electrolyte, and good chemical and structural stability under operating conditions.

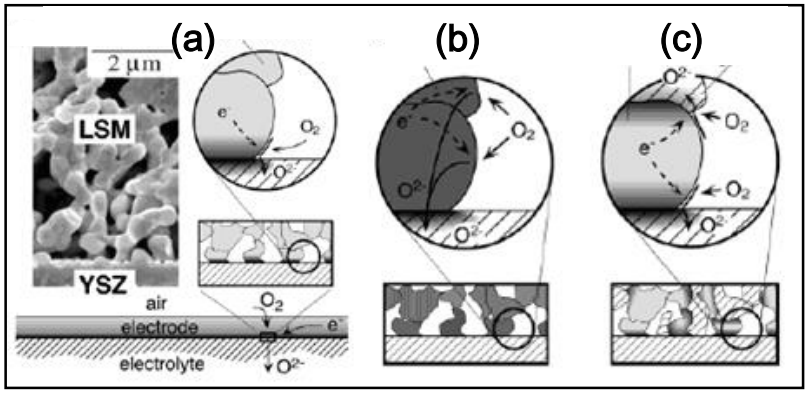

Figure 2.31. Schematic reaction models of different cathode materials. (a) Single-phase electronic conductor; (b) Single-phase mixed conductor; (c) composite of ionic and electronic phases.[174]

2.3.2 LSM-based cathodes

The commercialized cathode material for SOFC-O is $LaSrMnO_{3-\delta}$ (LSM), which shows good TEC compatibility with YSZ electrolyte and high electronic conductivity (>100 S cm^{-1}) at 800-1000°C. This material is very beneficial for the dissociation of oxygen molecules at the surface. One characteristics of this materials is its ORR activity can be improved by anodic and cathodic polarization (Figure 2.32). Such phenomena have been widely found, but the reason for such improvement has not reach consensus yet. Jiang et al.[175-178] proposed the incorporation of SrO and MnO_x into LSM lattice with the concomitant removal of cation vacancies, and improvement in the microstructure and morphology of LSM for the activation effect. Horita et al. studied the LSM/YSZ interface by secondary-ion mass spectroscopy and attributed the enhancement of the LSM electrode under cathodic current/potential treatment to the surface diffusion of oxygen vacancies on the LSM surface, which extends the active reaction sites from TPB to the bulk surface for the electrochemical reduction of oxygen.[179-181]

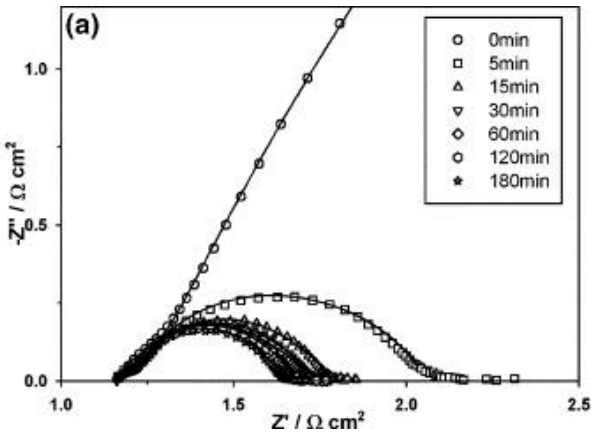

Figure 2.32. Initial impedance response for the ORR on a freshly prepared LSM electrode under a cathodic current passage at 200 mA cm^{-2} at 800°C in air.[175]

Its ionic conductivity, however, is very low, which results in sharp degradation of performance with decreasing temperature although it can exhibit a certain oxygen ionic conductivity under polarization conditions.[182] In order to use it as cathode material for intermediate temperature SOFC, an effective method is to introduce oxygen ionic conducting phase, such as YSZ, GDC, Bi_2O_3 to decrease the polarization loss. By switching YSZ with GDC, Murray and Barnett [183] showed that ASR at 700°C was reduced from 7.28 Ω cm^2 for pure LSM to 2.49 Ω cm^2 for LSM-YSZ and further to 0.75 Ω cm^2 for LSM-GDC cathode. While the reduction in ASR by adding an ionic conducting phase into LSM is undoubtedly due to the increased TPBs, the lowest ASR exhibited by LSM-GDC is conceivably attributed to the one-order of magnitude higher ionic conductivity of GDC than YSZ (*e.g.* 3.1×10^{-2} *vs.* 3.2×10^{-3} S cm^{-1}@600°C and 7.9×10^{-2} *vs.*1.8×10^{-2} S cm^{-1}@750°C) [184]. In other words, the electrical conductivity of the ionic conducting phase critically determines the ORR performance of a composite cathode. Wachsman's group [101, 102] reported a much reduced cathodic polarization resistance at intermediate temperatures by adding ESB into LSM. The ASR of the LSM-ESB cathode on GDC electrolyte is 10.56, 3.31, 1.11, 0.44, and 0.19 Ω cm^2 at 500, 550, 600, 650, and 700°C, respectively. The

maximum power density of a single SOFC using such cathode and ESB/GDC bilayer electrolyte reached 1,013 mW cm^{-2} at 650°C [102]. The follow-up work also confirmed improved intermediate-temperature performance with LSM-Bi_2O_3 composite cathode.[185-191] Li *et al.* reported that the 50%ESB-infiltrated LSM yielded ASR of 0.22 and 0.48 Ω cm^2 at 700 and 650°C, ~35 fold lower than those of pure LSM. [188] Jiang *et al.* showed that the ASR can be significantly reduced by infiltrating the LSM scaffold with yttrium-stabilized Bi_2O_3 (YSB), *i.e.* decreasing at 600°C from 85.2 Ω cm^2 for pure LSM to 4.95 Ω cm^2 for 20%YSB-infiltrated LSM and further to 1.08 Ω cm^2 for 50%-YSB infiltrated LSM. [187]

Besides the optimization of traditional cathode materials, many MIECs have been developed such as LSCF, BSCF, A_2BO_4-type, $AA'B_2O_5$-type. Here the latter three kinds of materials are briefly reviewed.

2.3.3 LSCF-based cathode materials

$La_{0.6}Sr_{0.4}Co_{0.8}Fe_{0.2}O_{3-\delta}$ (LSCF) has been a fabulous cathode for SOFCs, with a good compromise between high electronic and ionic conductivity, good catalytic activity, and improved stability at temperature above approximately 600 ℃. Beyond 600°C, LSCF behaves as a mixed ionic electronic conducting electrode, its cathode activity being stimulated by the formation of oxygen vacancies with increasing cathode overpotential. However, below 600 ℃ oxygen ion conductivity falls, due to the charge compensation domination by hole compensation instead of oxygen vacancy, and cathode behavior can be interpreted in terms of the classical triple-phase-boundary model.[192] A-site deficiency and high strontium content had a particularly positive effect on cell performance. Especially the LSCF with more than 40% Sr on the A-site (L55SCF, L58SCF) showed high power

densities (@0.7 V: 1.23 W/cm^2 at 800 ℃, 1.0 W/cm^2 at 750 ℃ and 0.7 W/cm^2 at 700 ℃, respectively), which is almost twice the power density of LSM/YSZ cells.[83] The dopant Fe reduces the TEC down to 15.3 × 10^{-6} K^{-1}, improving thermomechanical stability with respect to the GDC electrolyte (12.5 × 10^{-6} K^{-1}). Fabrication LSCF/GDC composites cathode can further reduce the TEC and increase ionic conductivity and thus result in lower ASR value, 0.17 Ω cm^2 at 600 ºC for LSCF-GDC (40:60wt%). [193]

Surface modification is an effective approach to enhance cathode functionality while retaining advantageous qualities of each constituent material. Deposition of nano-scaled particles on LSCF can effectively lower ASR. For single-phase LSCF, Marinha et al. used electrostatic spray deposition (ESP) to deposit nano-scaled LSCF particle on LSCF backbone together with an optimized LSCF current collection, ASR as low as 0.13 Ω cm^2 at 600ºC.[194] On the other hand, infiltration is an effective way to introduce nanostructure and a wide active materials no matter how high reactivity among other components in SOFC. Infiltration strategies could be an inherently functional infiltrate (specifically infiltration of an electro-catalyst onto the MIEC backbone) and a skeletal infiltrate (specifically infiltration of a catalyst/electrode material onto an electrolyte scaffold such as YSZ or doped ceria). Liu et al. infiltrated $La_{0.4875}Ca_{0.0125}Ce_{0.2-\delta}$ into LSCF backbone and the cathodic polarization resistance was reduced by ~60% (to ~0.076Ω cm^2) at 750 ℃, shown as Figure 2.33.[195] Shah infiltrated LSCF into porous GDC, which produced polarization resistance as low as 0.24 Ω cm^2 at 600 ℃.[196] Nevertheless, the fine microstructures tend to suffer coarsening at temperatures above 700ºC, which limits the operation temperature of nanostructured cathodes.

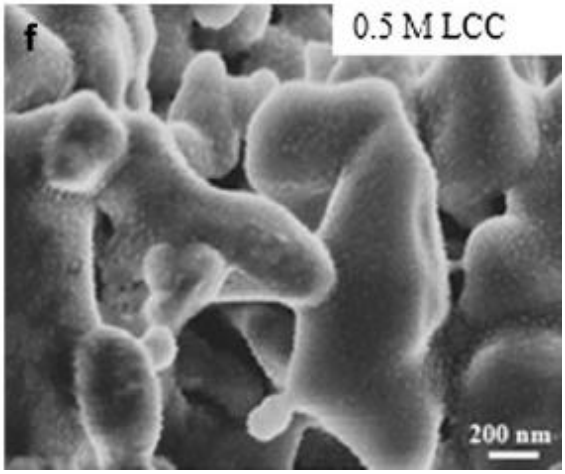

Figure 2.33. SEM of LCC infiltration into LSCF cathode.[195]

LSCF-based cathodes have severe performance degradation over time, typically at a rate of 0.05% per hour.[197] There are several possible degradation mechanisms, such as Cr poisoning, sulfur poisoning, coarsening and Sr surface segregation. The enrichment of Sr at the cathode surface may deactivate sites for ORR and hence increase cathode resistance.[198] This phenomenon occurs in many Sr-substituted perovskite materials like LSM, LSC, and LSCF. [197]

2.3.4 BSCF-based cathode materials

The BSCF material as cathode for SOFC was first reported by Shao and Haile in 2004.[115] The single cell in the form of Ni-Sm_2O_3-CeO_2|$Sm_{0.2}Ce_{0.8}O_2$|BSCF delivered P_{max} of 1010 and 402 mW cm^{-2} at 600 and 500 ^oC, respectively, exceeding the performance of SOFC with other cathode materials. The ASR are 0.055-0.071 and 0.51-0.61 Ω cm^2 at 600 and 500^oC, respectively. The excellent catalytic activity and oxygen transport ability render it a hotspot; numerous studies have been devoted to it in the following cathode studies.

Nevertheless, these impressive performances, which result from the fastest bulk transport and exchange rate, are companied by a low thermal stability, a high TEC (24 ×

10^{-6} K^{-1}), and the lattice instability. The recent study showed that it transformed from cubic to hexagonal structure below 850ºC, leading to degradation of performance. The good kinetic and bulk oxygen transport properties of BSCF seem to coincide with its low stability, as all these properties have the same underlying origin (a large size mismatch between A- and B-site cations). Thus, the substitution of cobalt ion by more chemically stable ions, such as Ti, is expected to decrease the TEC of the compounds and improve the chemical stability with CeO_2-based materials.[199] $Ba_{0.6}Sr_{0.4}Co_{1-y}Ti_yO_{3-\delta}$ (BSCT) oxides showed a TEC of about 14×10^{-6} K^{-1} at $y = 0.2$, which results in a good physical compatibility of BSCT with GDC electrolyte. Wei et al. synthesized and examined BSZF as a new cobalt-free cathode for IT-SOFCs.[200] The electrical conductivity was relatively low, with a maximum value of 9.4 S cm^{-1} at about 590 ℃, mainly caused by the high concentration of oxygen vacancy and the doping of bivalent zinc in B-sites. At 650 ℃ and under open circuit condition, symmetrical BSZF cathode on an SDC electrolyte showed polarization resistances (R_p) of 0.48 and 0.35 Ω cm^2 in air and oxygen, respectively. In addition, BSCF easily reacts with CO_2 below 900ºC, forming carbonate, which makes the long-term stability a challenge.

2.3.5 A_2BO_4-based cathode materials

The K_2NiF_4-type A_2BO_4 material is one member of the Ruddlesden-Popper ($A_{n+1}B_nO_{3n+1}$, $n \geq 1$) family. It is composed of ABO_3 perovskite layer and AO rock-salt layer with interstitial oxygens residing between the layers, as shown in Figure 2.34. A-site is lanthanide elements such as La, Nd, Sm, and Pr; doping with alkaline earth elements such as Sr can improve its electrical conductivity. B-site is transition metal elements, e.g., Ni, Co, Fe, Mn, Cu, etc. La_2NiO_4 is the typical material of this structure. Due to high

concentration of interstitial oxygen, both oxygen vacancy in the ABO_3 layer and the interstitial oxygen contribute to the oxygen ionic conductivity, which improves the oxygen ionic conductivity and surface oxygen exchange. The TEC of A_2BO_4-type materials is low ($10\text{-}14\times10^{-6}$ K^{-1}) because of its anisotropic structure (xy plane and axis direction), which is close to TEC of the present electrolyte materials. Furthermore, its catalytic activity in oxidizing atmospheres is fairly high.

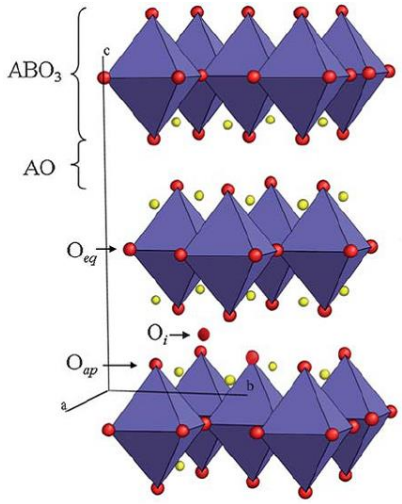

Figure 2.34. Schematic structure of A_2BO_4-based materials.

Nevertheless, the power density of SOFC with La_2NiO_4-based cathode is low, which is probably derived from the reaction between La_2NiO_4 and the electrolyte (YSZ, CGO, LSGM), resulting in the formation of poor electrical conducting phase, which impedes the transport of electrons and ions at the interface. Hernandez et al. investigated the compatibility of La_2NiO_4 with GDC and YSZ, and found that $La_3Ni_2O_7$ and $La_2Zr_2O_7$ impurities were formed after treatment at 900°C. Caronna et al. studied the reaction between La_2CuO_4 and LSGM, and partial dissolution was observed after treatment at 1000 °C. Sayers et al. reported that the ASR of symmetrical cells with La_2NiO_4 electrode and GDC electrolyte was 7.4 Ω cm^2 at 700°C; it decreased to 1.0 Ω cm^2 after introducing an

additional La_2NiO_4 layer between La_2NiO_4 electrode and GDC electrolyte. The P_{max} of single SOFC with $La_{1.2}Sr_{0.8}Co_{0.8}Ni_{0.2}O_{4+\delta}$-GDC cathode was 350 mW cm^{-2}.

2.3.6 $AA'B_2O_5$-based cathode materials

For simple perovskite ABO_3, when the A-site is doped with A', the distribution of A and A' at the A-site is disordered. However, when they are distributed orderly, i.e., the AO and A'O layers distribute alternatively as $[BO_2]$-[AO]-$[BO_2]$ -[A'O] along the c axis, the simple ABO_3 transform into A-site ordered layer perovskite $AA'B_2O_6$. Because the oxygen in the AO layer can be partially or completely removed with the formation of oxygen vacancy, both $[BO_6]$ octahedron and $[BO_5]$ square pyramid exist in this structure, as shown in Figure 2.35.

For $AA'B_2O_{5+\delta}$ ($0 < \delta < 1$), A is lanthanide elements such as La, Pr, Nd, Gd; A' is Ba or Sr; B is transition metal elements, e.g., Co, Fe, Cu. The oxygen vacancy distributes in the LnO layer with the formation of 2D plane for oxygen transportation, decreasing the bond strength of B-O, which significantly enhances the oxygen ionic conductivity, surface oxygen exchange and bulk diffusion processes.

$GdBaCo_2O_{5+\delta}$ (GBCO) is the earlier studied material among the $AA'B_2O_{5+\delta}$family. The oxygen diffusion coefficient is as high as 10^{-5} cm^2 s^{-1} at 600°C and the ionic conductivity is 0.01 S cm^{-1} at 500°C [41]. Chang et al. first studied the feasibility of GBCO as cathode for SOFC-O. The ASR was 0.53 Ω cm^2 at 645 °C for symmetrical cells with GBCO cathode and CGO electrolyte, which can be decreased with microstructure optimization [42]. These results indicate that GBCO can be potential cathode for SOFC-O^{2-}. Tarancón et al. [43] reported that P_{max} of single cell (Ni-YSZ/YSZ/GBCO) was 250 mW cm^{-2} at 800°C with 5% H_2 as fuel. The addition of porous YSZ layer between cathode and electrolyte further

enhanced P_{max} to be 500 mW cm^{-2}. Later, Kim et al. found that the oxygen bulk diffusion coefficient and surface exchange coefficient of $PrBaCo_2O_{5+\delta}$ (PBCO) were 2-3 orders of magnitude higher than that of GBCO. The ASR was only 0.15 Ω cm^2 at 600°C for PBCO-GDC composite cathode with GDC electrolyte, which showed its great potential as cathode for SOFC-O^{2-} [44]. Further investigation [45] revealed that the polarization resistance of PBCO cathode was mainly ascribed to the oxygen diffusion across the interface between cathode and electrolyte, and the electronic conduction at the electrode surface. The P_{max} of single cell with SDC electrolyte was 620 and 165 mW cm^{-2} at 600 and 450°C, respectively, the degradation of which with temperature was obviously lower than cells with other cathode materials. Zhou et al. [46] systematically studied the performance of $LnBaCo_2O_5$ and $LnBaCo_2O_5$-SDC composite cathodes. The electrochemical properties decreased with decreasing ionic radius of Ln^{3+} because the electrical conductivity and oxygen bulk diffusion coefficient decreased. The substitution of Sr for Ba will improve the performance [47,48].

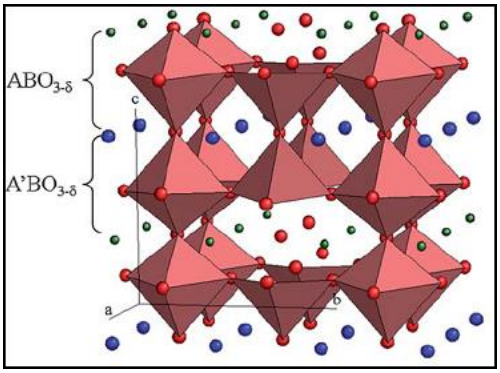

Figure 2.35. Schematic structure of $AA'B_2O_5$.

Compared with other cathode materials, the A_2BO_4 and $AA'B_2O_5$ materials distinguish themselves with high oxygen bulk diffusion and surface oxygen exchange coefficients, as shown in Table 2.2 [49].

Table 2.2 Oxygen bulk diffusion and surface exchange coefficients, and electrical conductivity of several cathode materials.

	D* ($cm^2 s^{-1}$) @ 500 °C	E_A^D (eV)	k* ($cm\ s^{-1}$) @ 500 °C	E_A^k (eV)	σ ($S\ cm^{-1}$) @ 500-750 °C
$La_{0.8}Sr_{0.2}MnO_{3-\delta}$	4.5×10^{-20}	2.80	3.1×10^{-11}	1.30	120-130
$La_{0.8}Sr_{0.2}CoO_{3-\delta}$	9.0×10^{-14}	2.22	2.8×10^{-9}	1.32	1500-1600
$La_{0.5}Sr_{0.5}CoO_{3-\delta}$	1.5×10^{-10}	1.41	3.9×10^{-7}	0.81	1300-1800
$La_{0.6}Sr_{0.4}Co_{0.2}Fe_{0.8}O_{3-\delta}$ -$Ce_{0.8}Gd_{0.2}O_{2-\delta}$	1.2×10^{-10}	1.39	3.3×10^{-9}	1.60	250-300
$Ba_{0.5}Sr_{0.5}Co_{0.8}Fe_{0.2}O_{3-\delta}$	1.2×10^{-7}	0.50	1.1×10^{-6}	1.76	10-55
$La_2NiO_{4+\delta}$	3.3×10^{-9}	0.56	7.0×10^{-9}	0.60	55-65
$La_2CoO_{4+\delta}$	2.5×10^{-8}	0.12	3.2×10^{-6}	0.03	1-5
$GdBaCo_2O_{5+\delta}$	2.8×10^{-10}	0.60	7.5×10^{-8}	0.81	550-925
$PrBaCo_2O_{5+\delta}$	3.6×10^{-7}	0.48	6.9×10^{-5}	0.67	400-700

2.4 Computational methods

Computational study by *ab initio* methods has a wide application in SOFC study, such as the effects of doping-induced defects and energy barrier for ionic diffusion. Calculations are particularly valuable to study the cases where experimental methods are difficult or cannot be directly carried out. Like solving the defect problem as oxygen vacancies formation, Carter et al.[201] performed an analysis on $LaMO_3$ (M = Cr, Mn, Fe, Co) materials, providing a basis for design principles for SOFC cathode materials from easily measurable or computable properties. Morgan et al.[202] used *ab initio* energetics and

empirical modeling to develop a defect model for $LaMnO_3$ to predict defect concentrations, obtaining results in good agreement with experimental results. Maier et al.[203] verified the most probable reaction mechanisms for ORR on LSM cathode materials using DFT calculations, and found a correlation between the reaction mechanism and point defect concentrations. Asta et al.[204] studied the dopant-defect interactions in proton conductor Sr-doped $LaPO_4$, concluding that dopant binding stabilized the proton incorporation, lowering the proton transport kinetic rate. Once the DFT model is accurately setup, due to its inherent parameter-free nature, it is reliable in providing fundamental understanding of material properties at the atomic-level.

2.4.1 Density functional theory

Quantum mechanics with the Schrödinger equation describes the location and energy of a system consisted of low-mass particles. Solutions to the Schrödinger equation with one electron are known for various potentials. However, the problem becomes analytically intractable for systems containing N electrons. The wavefunction quickly grows in complexity due to 3N degrees of freedom. Hence, approximation approach is necessary to get viable solutions that reasonably describe the material of interest. Density functional theory (DFT) is one of the powerful tools among the approximate quantum mechanical methods developed by Hohenberg, Kohn and Sham.[205, 206] They proved two theorems as the foundation of DFT: the ground-state electron density determines the potential of a system; the electron density acts as the variational quantity instead of the electron wavefunction. Thus, the approximation of the ground-state electron density can be achieved with a simple expression

$$E[\rho] = T[\rho] + V_{ext}[\rho] + V_{ee}[\rho] \quad (2\text{-}20)$$

where $E[\rho]$ is the total energy of the system. ρ is single electron density; $T[\rho]$ is the kinetic energy; $V_{ext}[\rho]$ is the potential energy from the external field from nuclei; $V_{ee}[\rho]$ is the electron-electron interaction energy. In this equation, the functional T and V_{ee} are unknown. To solve this problem, Kohn and Sham proposed an approximations that the ground state density of a fully interacting many-body system is equal to that of a fictitious system of N non-interacting system, in which the kinetic energy and electron density can be calculated exactly from the set of orbitals. The classical coulombic interaction is dominated by the electron-electron interaction, referred as Hartree energy ($V_{Hartree}$). The Equation (2-20) can be written in Kohn-Sham approach,

$$E[\rho] = T_s[\rho] + V_{ext}[\rho] + V_{Hartree}[\rho] + E_{xc}[\rho] \quad (2\text{-}21)$$

Here $T_s[\rho]$ is the kinetic energy of a system of non-interacting electrons; $E_{xc}[\rho]$ is the only unknown term. Combining with Equation (2-20) yields

$$E_{xc}[\rho] = (T[\rho] - T_s[\rho]) + (V_{ee}[\rho] - V_{Hartree}[\rho]) \quad (2\text{-}22)$$

Here the term $E_{xc}[\rho]$ is called exchange-correlation functional, which includes the exchange and correlation energy of electrons. For the exchange energy, the wavefunction of a many-electron system produces a spatial separation between electrons that have the same spin and thus reduces the Coulomb energy of the electronic system. The reduction in the energy is called exchange energy, corresponding to the term $(V_{ee}[\rho] - V_{Hartree}[\rho])$. For correlation effect, if electrons of opposite spins are spatially separated, the Coulomb energy of the electronic system is reduced, while the kinetic energy of the electrons increases. The correlation energy (E_{corr}) corresponds to the term $(T[\rho] - T_s[\rho])$. E_{corr} of many-electron system is extremely difficult to calculate since wavefunction of the system depends on the coordinates of all the electrons. Therefore it is commonly approximated from models.

2.4.2 Exchange and correlation functionals

2.4.2.1 Local density approximation (LDA)

Kohn and Sham proposed that system in solids state can be close to the limit of the homogeneous electron gas.[205] In this limit, it is known that the effects of exchange and correlation are local. They proposed a method to calculate local density approximation (LDA), in which the exchange-correlation energy is simply an integral over the entire space with the exchange-correlation energy density at each point being assumed to be the same as in a homogeneous electron gas with that density. $E_{xc}[\rho]$ can be defined by

$$E_{XC}[\rho] = \int dr \rho(r)\, \varepsilon_{XC}(r) \tag{2-23}$$

where $\varepsilon_{XC}(r)$ is assumed to depend only on the density at point r, which actually should be affected by other points. Thus, $\varepsilon_{XC}(r)$ becomes localized,

$$\varepsilon_{XC}^{LDA}(r) = \varepsilon_{XC}^{LDA}\big(\rho(r)\big) \tag{2-24}$$

The assumption is reasonable wherever the density varies slowly in space. Indeed, it has successfully predicted many measurable quantities such as the ground state geometries, vibration and phonon frequencies, and moments of the density.[207] LDA gives ionization energies of atoms, dissociation energies of molecules, and cohesive energies with accuracies of 10-20% and bond lengths and geometries of solids and molecules with an accuracy of $\sim$ 1%.[208] However, LDA fails on systems that are dominated by electron-electron interaction effects.[209] Besides, LDA systematically underestimates excited state energies and the band gaps in semiconductors and insulators, overestimates the cohesive energies, gives the wrong ground state of some magnetic materials and fails to appropriately describe the Van der Walls interactions.[210]

2.4.2.2 Generalized gradient approximation (GGA)

To overcome the inaccuracy, incorporating the local gradient of the density by replacing $\varepsilon_{XC}(r)$ with $\varepsilon_{XC}(\rho, |\nabla\rho|)$ can improve the LDA methodology. This better method is the generalized gradient approximation (GGA)[211-214]. The basic premise of the GGA includes the spatial variation in the electron density close to that of real materials. In general, the GGA improves substantially over the LDA, particularly for dissociation energies, improved cohesive energies, and more accurate predictions of magnetic properties. Usually, LDA underestimates bond length by 1-2 %, GGA tend to slightly overestimate it.

However, in some cases GGA overcorrects the deficiencies of the LDA and leads to an underbinding.[210] There are many different ways to include electron density gradient in a GGA functional leading to many different GGA functionals[215]. The next major advance came with the inclusion of a fraction of Hartree-Fock exact exchange (HF) in the functional, as described by Becke in the early 1990s. New functionals hybrid the exact results for the exchange part of the functional with approximations of the correlation part and become the most commonly used functionals in DFT calculations based on spatially localized basis functions.[216] This work has led to the development of B3LYP, the most widely used of all the functionals. B3LYP have been extremely successful in predictions of properties of small molecules listed in Table 2.3. The mean absolute error represents the precision of the result. In the 55 benchmarking studies, B3LYP gave the best performance among the functionals tested in only four cases. Developing functionals that improve upon B3LYP will clearly provide a significant advance for DFT.

Table 2.3 Typical accuracy for B3LYP calculation on small molecule test sets[217]

Physical Property	Typical Mean Absolute Error	Typical Value in Test Sets
Bond length	0.01 Å	1.1-1.5 Å
Bond angle	1°	110°
Barrier height	3-4 kcal/mol	12-25 kcal/mol
Atomization energies	1-2 kcal/mol (10-20 kcal/mol for metal dimers)	500 kcal/mol (58 kcal/mol for metal dimers)
Binding energies	5-10 kcal/mol	60-80 kcal/mol
Heats of formation	5-20 kcal/mol	50 kcal/mol
Hydrogen bond strengths	0.5-1 kcal/mol	8 kcal/mol

Other widely used non-empirical GGA functionals are the Perdew-Wang functional (PW91) and the Perdew-Burke-Ernzerhof functional (PBE)[218]. Hammer et al. compared LDA, PBE GGA and PW91 GGA functionals by examining CO adsorption on five metal surfaces and NO adsorption on four metal surfaces.[219] In general, for adsorption energies, LDA calculations gives considerably worse results than GGA functionals. The PW91 functional gave root mean square (RMS) deviation between calculations and experimental data of 0.78 eV for CO and 0.52 eV for NO. This RMS deviation decreased slightly to 0.67 and 0.43 eV by the PBE functional.

2.4.3 Basis sets

A judicious choice of basis sets for the expansion of the single particle wavefunctions is important for the solution of the Kohn-Sham equations. A basis set is the set of functions used to describe the shape of the orbitals in an atom. Hybrid functionals introduce a strong divide between DFT calculations based on localized basis sets (atomic orbitals, shorten for AO) and plane waves (PW). The atomic orbitals basis sets are more efficient where localized bonding exists, such as atoms, molecules, and clusters. Since the molecular orbital shapes often resemble those of the atomic orbitals, only a small number of basis functions are needed in the expansion of the wavefunctions. The most popular minimal basis set is the STO-nG. Another family of basis sets, commonly referred to as the Pople basis sets, are indicated by the notation 6-31G. The 6-31G is probably the most popular basis at present. This notation means that each core orbital is described by a single contraction of six GTO primitives and each valence shell orbital is described by two contractions, one with three primitives and the other with one primitive. It gives good geometries and reasonable relative energies.

Plane-wave basis sets are the method of choice for extended crystalline systems, particularly those containing metallic phases. The Kohn-Sham method employing a plane-wave basis set and the pseudopotential (PP) approximation are currently among the most successful techniques in computational material science.[214]

The computational procedure of the *Vienna Ab-initio Simulation Package* (VASP) code [220, 221] includes an iterative solution of the Kohn–Sham equations based on residuum-minimization and optimized charge-density mixing routines,[222] which includes the calculations of the Hellmann–Feynman forces acting on the atoms and of the stresses on

the unit cell. The total energy is optimized with respect to the positions of the atoms within unit cell or supercell. With the use of pseudopotentials, by treating only the valence electrons, can further improve the efficiency and accuracy of plane wave-based DFT calculations.[214] In the pseudopotential approximation, the electronic potential is separated between a core region and a valence region. The strong core potential that includes the Coulombic attraction, the Hartree potential due to the core charge, and a component of the exchange-correlation potential related to the valence-core interaction, is replaced by a pseudopotential whose ground state wavefunction mimics the all electron valence wavefunction outside the selected core radius. Further development of this concept has been made by Blöchl by combining ideas from pseudopotential and Linearized Augmented-Plane-Wave (LAPW) methods in a framework, called the Projector Augmented-Wave Method (PAW).[223] The advantage of *VASP* plane wave calculations is that the complete optimization of lattice relaxation upon vacancy creation, even for large supercells, can be performed much faster with geometry optimizations being carried out with an accuracy 10^{-3} *e*V in the total energy.

2.4.4 DFT modeling for research interest in SOFCs

A number of SOFC research groups have been utilizing DFT-based methods to study properties of materials, interfaces, nanostructure and physical/chemical pathways. For example, in terms of the conductivity of the common YSZ electrolyte material, Pornprasertsuk et al. used a DFT method with LDA and gradient correction by kinetic Monte Carlo to study the oxygen vacancy diffusion mechanism.[224] DFT provided the energy barriers along the minimum energy path for a vacancy to migrate, which examined the effect of dopant concentration on conductivity. Traditional material defect theory would

suggest that conductivity should continue to increase with dopant concentration; however, it has long been recognized that the conductivity no longer increases once approximately 8 mol% Y_2O_3 is reached. Pornprasertsuk identified the migration energy needed to traverse two adjacent tetrahedral containing the Zr-Y and Y-Y common edge as the root of this limitation. Experimental and simulated conductivity versus dopant concentration trends were in good agreement.

Adsorption, dissociation, and pathways associated with catalytic and electro-catalytic processes in heterogeneous electrode structures were explored by Rosmeisl and Bessler using plane-wave DFT with GGA to calculate the stability of H, O, and OH radicals on Pt, Ag, Mn, etc.[225] These materials were treated as anode electro-catalysts interfacing with YSZ for studying the electrochemical oxidation pathways via energy minimization. Oxygen spillover was identified as a dominant pathway, with the electro-catalytic activity linked to the binding affinities of the reactive intermediates. The electro-catalytic activity, defined as the change in free energy for the rate determining step, was found to scale with the experimentally determined binding energy for various catalysts with Ni sitting atop the volcano plot.

In the DFT study of ORR mechanisms, Choi et al.[226] [227] established a surface and interface model for the junction of the electrode and electrolytic materials. One of the topics examined was the adsorption sites and configurations for perovskite cathode materials, as well as the oxygen incorporation step. Mastrikov et al., purposed DFT calculations with PW91 of GGA and plane wave basis set, studied the mechanism of oxygen incorporation into LSM.[203] MnO_2 (0 0 1) was identified as the most stable surface termination for fuel cell conditions. Mechanistically, the rate determining step was identified as the surface

oxygen vacancy encountering an adsorbed O^- via activated surface diffusion of the vacancy, which suggests the need for a higher surface vacancy concentration and mobility. As a part of these efforts, oxygen adsorbates were found to be rather low, which was explained by negative adsorption entropy and electrostatic repulsion, despite the exothermic formation of O^{2-}, O_2^{2-}, and O^- on Mn.

Another DFT application in SOFCs is the understanding of materials stability in the presence of poisons and contaminants. For the stability and degradation mechanisms of Ni in the presence of carbonaceous fuels, Nikolla et al.[228] used DFT with PW91 function set of GGA and identified that alloying the Ni surface can promote the oxidation of C atoms, rather than allowing the formation of strong C-C bonds. To combine with the experimental observation, Sn/Ni alloy was found to improve stability to carbon and adsorption relative to Ni (1 1 1), in the presence of methane, propane, and isooctane with a steam to carbon ratio of 1.5. These demonstrations experimentally exhibited hundreds of hours of stability. Galea et al.[229] performed similar study on Ni and Cu (1 1 1) and (2 1 1), Cu-Ni and Cu-Co alloys in the presence of methane. They found that C adsorbs strongly onto the Ni (2 1 1) surface and grows graphitic carbon over the terrace, while Cu was found to have a very high thermodynamic and kinetic barrier to CH_4 dissociation, which restricts breakdown and contributes to direct electrochemical oxidation. The Cu-Ni and Cu-Co alloys showed that Ni and Co has little effect on surface Cu and that stability is limited by the Cu enrichment of the alloy surface.

CHAPTER 3

STUDY OF $BaZr_{0.8}Y_{0.2}O_{3-\delta}$ – MOLTEN CARBONATE COMPOSITE ELECTROLYTE FOR IT-SOFCS

3.1 Introduction

As aforementioned, $BaZr_{0.8}Y_{0.2}O_{3-\delta}$ (BZY) has good ionic conductivity and chemically stability, but it is hard to sinter into a dense body. To enable BZY sintering at lower temperatures, molten carbonate (MC) was studied as a sintering aid to promote the densification of BZY, while introducing CO_3^{2-} into the ionic conduction, making it a mixed H^+ and CO_3^{2-} conductor. Similar work of combining oxide-ion conductors such as doped-CeO_2 and molten carbonates as an IT-electrolyte has also been reported by other groups with excellent SOFC performance.[230-233] Aiming to understand the role of proton conduction in the conductivity, ionic conduction behavior was particularly investigated in the MC-BZY composite electrolyte by electrochemical and computational mythologies.

First principles approach was used to calculate the energetics of proton transfer in three entities: CO_3^{2-}, Li_2CO_3 crystal and $(Li_2CO_3)_8$ cluster to provide a theoretical ground for the understanding of enhanced ionic conductivity and improved SOFC performance observed in the experiments. A $(Li_2CO_3)_8$ cluster was employed to represent the state of an alkali molten carbonate. To understand the energetics of proton migration across the BZY/MC interface from a DFT perspective, pathways and energetics of proton migration

at the ZrO_2-terminated (100) surface of a pure $BaZrO_3$ and a $BaZrO_3$ with MC were particularly computed and compared.

3.2 Experimental methods

The BZY ($BaZr_{0.8}Y_{0.2}O_{3-\delta}$) electrolyte was synthesized by conventional solid-state reaction. The staring materials were $BaCO_3$ (99.8%, Alfa Aesar), ZrO_2 (99.7%, Alfa Aesar) and Y_2O_3 (99.9%, Alfa Aesar). Stoichiometric amounts of the starting materials were first weighed, intimately mixed and pelletized, followed by firing at 1100^{o}C for 5 h. The calcined pellets were then broken into powders and calcined again at 1300^{o}C for another 5 h. After ball milling, the powders were then blended with ~10 wt% of carbon-black as a pore former, pelletized and finally sintered at 1500^{o}C for 5 h. As-prepared samples were porous and ready for molten carbonate infiltration.

Two molten carbonate systems were selected for this study: Li_2CO_3-38mol% K_2CO_3 (denoted as LK) and Li_2CO_3-48mol%Na_2CO_3 (denoted as LN); these compositions reflects a eutectics. They were first melted and homogenized in a crucible at 650^{o}C for 2 h. The porous BZY pellet pre-loaded in a silver basket were then slowly immersed into the MC. After a roughly 2-h soaking, they were gradually pulled out of the melt and suspended above the crucible before slowly cooling the finance to room temperature. Thus fabricated MC-BZY composites were slightly polished to remove the residual carbonate on the surface. The samples were then ready for microstructural and electrical characterizations.

The phase purity of the BZY powder and MC-BZY composites were examined by X-ray diffraction (XRD) using (D/max-A, Rigaku, Japan), while microstructures of the BZY as well MC-BZY composites were captured by a field emission scanning electron microscopy (FE-SEM, Zeiss Ultra).

The ionic conductivity of the MC-BZY composites were assessed by electrochemical impedance spectroscopy (EIS) on a symmetrical cell configuration consisting of the MC-BZY composite sandwiched by two identical silver-based electrodes and current collectors. The EIS measurements were carried out using an electrochemical workstation (IM6, Zahner) under open-circuit conditions within a frequency range of 10^5 to 0.01 Hz and under a 10 mV of stimulus AC amplitude. The ionic resistance was extracted from the high-frequency intersection of the spectrum with the real-axis. The temperature was varied from 400 to 650ºC, covering the solid-to-liquid transition of the carbonate phase (the melting temperature of the carbonate phase is ~500ºC).

To understand the nature of ionic conduction, the ionic conductivity was also measured in both oxidizing (air) and reducing atmospheres (H_2-N_2 mixture) with a range of varied partial pressures of H_2O and H_2. The different partial pressures of H_2O were generated by a homemade water bubbler system and monitored by an on-line humidity sensor (Vaisala model 332). To verify the involvement of protons in ionic conduction, D_2O was also used as an alternative to H_2O. In addition, the effects of MC loading and MC-type on ionic conductivity were also studied.

3.3 Computational methods

3.3.1 Calculations for CO_3^{2-}, HCO_3^- species and proton migration at interface of carbonate and BZY

All calculations were performed by the Vienna *Ab Initio* Simulation Package (VASP), version 5.3. The projector-augmented wave (PAW) method was used for calculating core and valence electron interactions and the Perdew-Burke-Ernzerhof (PBE) form of the generalized gradient approximation was used for the exchange-correlation interaction.

For CO_3^{2-}, HCO_3^- species and Li_2CO_3 periodic structure, a vacuum layer of 15 Å was applied for CO_3^{2-} and HCO_3^- species, while a 3 × 2 × 2 *k*-point grid for a 96-atom supercell was used for modeling the proton transport properties in Li_2CO_3 periodic structure. The cut-off energy was set to 500 eV. The self-consistent field cycle convergence tolerance was set to 10^{-4} eV and the Hellmann-Feynman force on each atom was minimized to less than 0.02 eVÅ^{-1}. For searching the minimum energy paths and transition states in proton transportation, climbing image-nudged elastic band (CI-NEB) method was applied.

For calculation of proton interfacial migration, a 4 × 4 × 1 Monkhorst-Pack sampling of the Brillouin zone was used. A vacuum layer of 15 Å along the z-axis direction was created to guarantee no interaction between cells. The O $2s^2 2p^4$, C $2s^2 2p^4$, Zr $4s^2 4p^4 5s^2 4d^2$, Y $4s^2 4p^4 5s^2 4d^1$, and Ba $5s^2 5p^6 6s^2$ were taken as the valence electron configurations in the calculations. The cut off energy and force criterion were set to 500 eV and 0.02 eV/Å, respectively. In addition, the D2 method of Grimme was used to calculate the dispersion interaction between carbonate species and surface, where the cutoff radius for pair interactions, global scaling factor optimized at the PBE and damping parameter were 15.0 Å, 0.75 and 20.0, respectively. The saddle points and migration pathways of the minimum energy were sought by the nudged elastic band (NEB) method. Spin-polarized and dipole corrections have been taken into account. Besides, calculations on energetics and pathways of proton migration were on an 8-layer asymmetrical slab at the ZrO_2-terminated (100) surface. An asymmetrical slab was chosen to maintain a stoichiometric and neutral unit cell, which is an acceptable approach in the study of similar systems.

3.3.2 Calculations of energetics of $(Li_2CO_3)_8$ and $[(Li_2CO_3)_8H]^+$ clusters

Calculations of energetics of $(Li_2CO_3)_8$ and $[(Li_2CO_3)_8H]^+$ clusters were performed by Gaussian 09 suite of quantum programs, including the geometry optimization, transition state search and intrinsic reaction coordinate (IRC) calculations. The geometries were optimized by using the generalized gradient approximation (GGA) based hybrid functional of B3LYP in combination with the full-electron basis set with polarization functions of 6-31G(d) to obtain accurate results. B3LYP has been proven to be reliable in treating electronic exchange and correlation over a wide range of molecular systems. The vibrational frequencies of each cluster were calculated at the same computational level as the geometry optimization, ensuring that the structures are located at a true minimum on the potential energy surface and the transition state is a first-order saddle point on the potential energy surface. All resultant energies contained the zero-point energy (ZPE) corrections. In addition, the interactions between proton and carbonate ions are orbital overlap and electrostatic interactions. Therefore, the dispersive interactions can be ignored in our calculations.

3.4 Results and Discussion

3.4.1 XRD patterns and microstructures

The XRD patterns of BZY synthesized at 1500^{o}C for 5 h is shown in Figure 3.1 (a), indicating two cubic phases, which were reported as $BaZrO_3$ and $BaZr_{0.95}Y_{0.05}O_{3-\delta}$ perovskite phases[234]. Besides, the XRD patterns of BZY-LN composite fired at 650^{o}C is shown in Figure 3.1 (b); the additional peaks compared to BZY's can be identified as LN carbonate[235]. Rietveld refinement of XRD patterns was done to pure BZY and BZY/molten carbonate samples. For both samples, the mole ratios of $BaZrO_3$ to

$BaZr_{0.95}Y_{0.05}O_{3-\delta}$ were consistent in 59:41. Besides, pure $BaZrO_3$ exhibited a cubic structure with a lattice parameter a=4.2021 Å and a=4.1999 Å after infiltration, while $BaZr_{0.95}Y_{0.05}O_{3-\delta}$ showed a cubic structure with a lattice parameter a=4.2366 Å and a=4.2358 Å after infiltration. The merely changed lattice parameter indicated no reaction between BZY and molten carbonate.

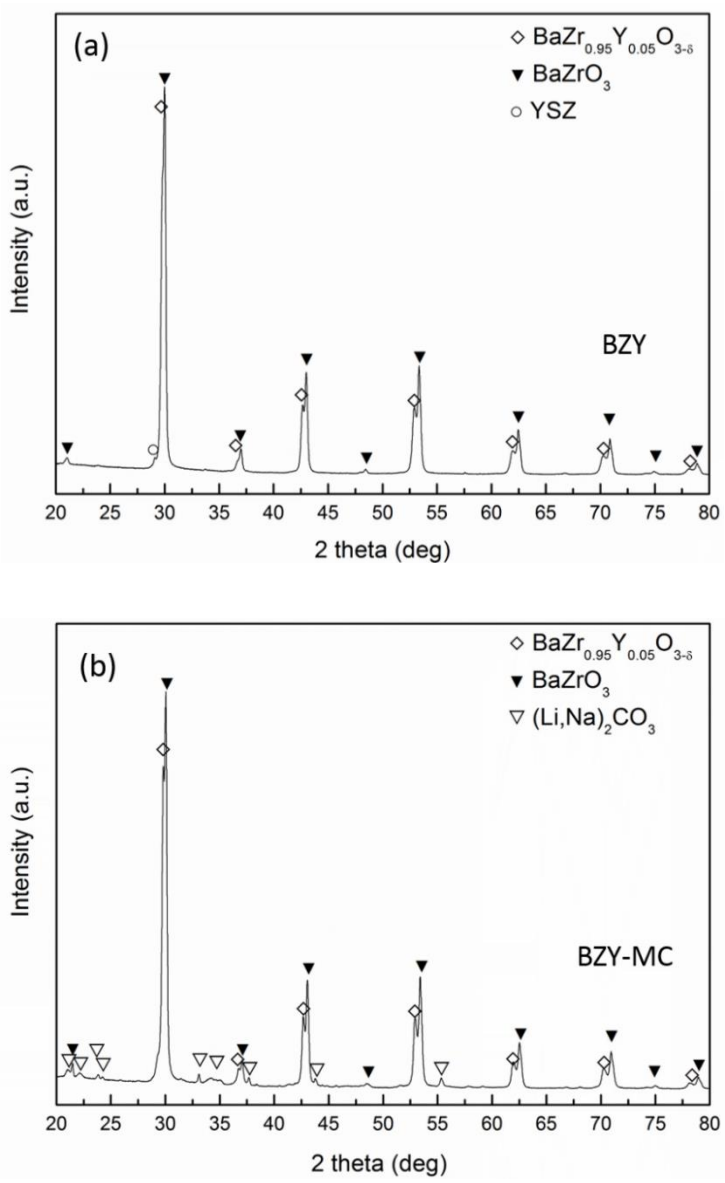

Figure 3.1. XRD pattern of (a) BZY sintered at 1500 ^{o}C for 5h and (b) BZY-MC fired at 650 ^{o}C.

The microstructures of BZY and MC-BZY composite are shown in Figure 3.2 (a) and (b), respectively. It is evident that BZY even after sintering at 1500^{o}C contains poorly connected grains, indicating the refractory nature of BZY materials. By contrast, Figure 3.2 (c) and (d) of MC-BZY composite show a rather dense microstructure with MC phase filling the pores.

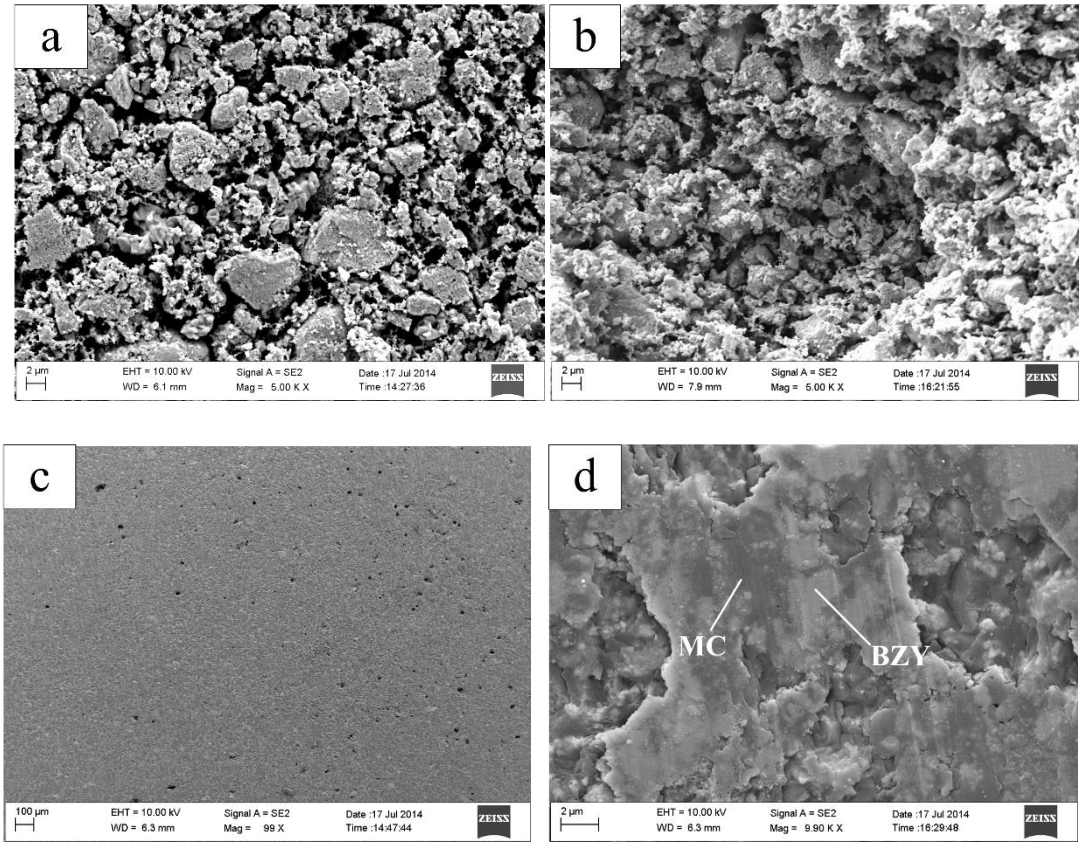

Figure 3.2. SEM images of (a) surface and (b) cross-section of BZY sintered at 1500^{o}C; (c) surface and (d) cross-section of a Li-Na carbonate/BZY composite prepared at 650^{o}C.

3.4.2 Electrochemical impedance spectroscopy

3.4.2.1 Conductivity *vs* MC loading

The effect of MC loading on ionic conductivity of a LK-BZY is shown in Figure 3.3. Since the MC loading is determined by the initial porosity in BZY, different contents of carbon-black pore former were used during preparation of porous BZY. Figure 3.3 clearly

indicates that higher MC loading (or higher initial porosity in BZY) results in a higher ionic conductivity over the entire temperature range tested. This is an expected result as the primary conductor in MC-BZY is the MC phase. In practice, however, the high conductivity of the MC phase could be limited by the amount of MC that can be retained within the BZY skeleton, analogous to the case of MC in $LiAlO_2$ matrix for commercial molten carbonate fuel cells.

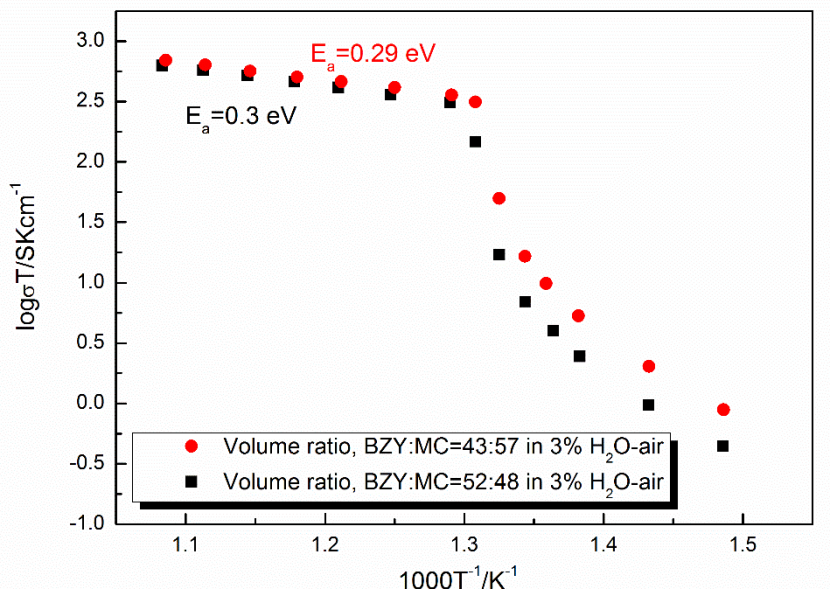

Figure 3.3. Ionic conductivity *vs* temperature in LK-BZY composites at different MC loadings.

3.4.2.2 Conductivity *vs* MC type

The effect of MC type, *i.e.* LK *vs* LN, on ionic conductivity of MC-BZY is shown in Figure 3.4. To ensure a fair comparison, the MC loading of the two samples was fixed at 48 vol%. Clearly, LN-BZY has a higher conductivity than LK-BZY at t>500^{o}C. This observation is consistent with the literature showing higher conductivity for LN than LK system [236]. Therefore, the LN system was selected for the subsequent electrical characterization.

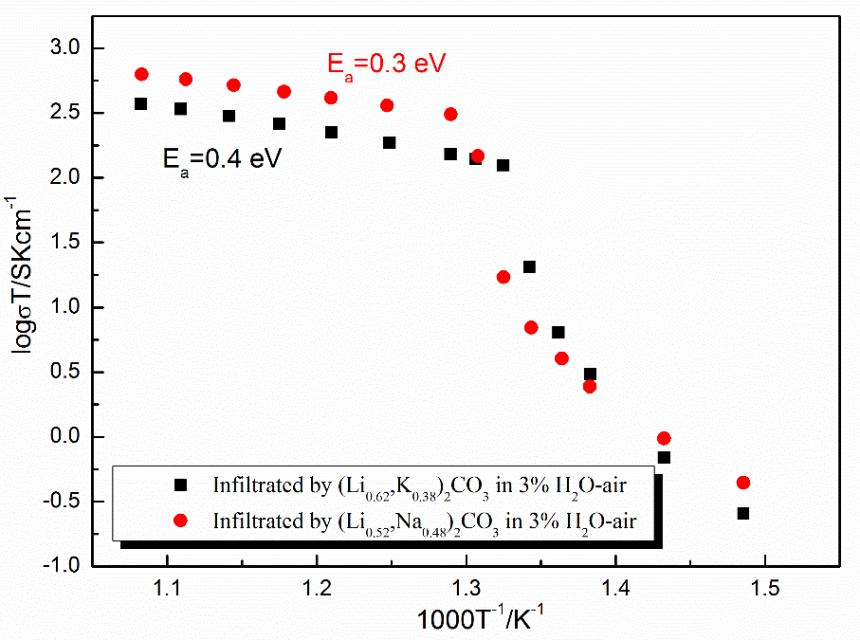

Figure 3.4. Conductivity comparison of LK/BZY and LN/BZY vs temperature in 3%H_2O-air.

3.4.2.3 Conductivity *vs* atmosphere

Figure 3.5 shows the conductivity of a LN-BZY with a MC loading of 57 vol% measured in both oxidizing and reducing atmospheres. It is evident that conductivity measured in reducing 3%H_2O-(5%H_2–N_2) is higher than that measured in oxidizing 3%H_2O-air over the entire temperature range. The result suggests that the enhanced conductivity by H_2 should be associated with the MC phase since the BZY's conductivity above the melting temperature is negligible compared to the MC phase. The almost identical activation energy between the LN-BZY and pure LN supports this assertion.

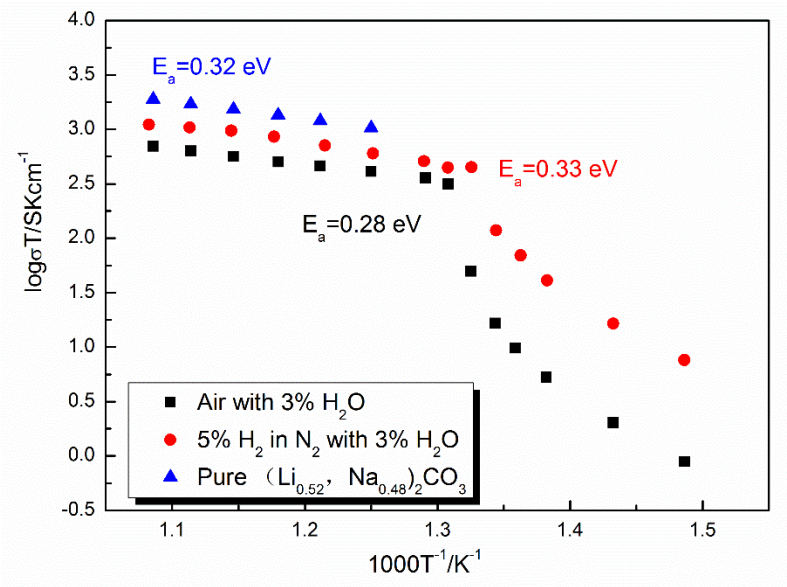

Figure 3.5 Conductivity *vs* temperature of a LN-BZY composite measured in 3%H_2O-air and 3%H_2O-(5%H_2-N_2)

3.4.2.4 Conductivity *vs* P_{H_2O}

To further investigate the feasibility of proton conduction, the conductivity of a LN-BZY composite with a MC loading of 57 vol% was measured as a function of partial pressure of H_2O (P_{H_2O}) at 600°C; the results are shown in Figure 3.6. First, the conductivity in reducing 5%H_2-N_2 is nearly twice as high as that in air under each P_{H_2O}, which agrees with Figure 3.5 measured under P_{H_2O} =0.03 atm. Second, the conductivity increases with P_{H_2O}. Third, the dependence of conductivity on P_{H_2O} is almost the same for the two gas compositions. These observations again suggest that the proton conduction be associated with the MC phase and protons be originated from either H_2O or H_2 or both.

From a defect chemistry point of view, the enhanced proton conductivity by H_2 and H_2O can be understood by the following reaction (in Kröger-Vink notation):

$$H_2O_{(g)} + V_O^{\bullet\bullet} + (CO_3)^{\times}_{CO_3} = (OH)^{\bullet}_O + (HCO_3)^{\bullet}_{CO_3} \qquad (3\text{-}1)$$

here $V_O^{\bullet\bullet}$ denotes oxygen vacancies in BZY; $(OH_O^{\bullet})$ represents hydroxyl defect residing on

oxygen lattice of BZY; $(CO_3)^{\times}_{CO_3}$ is a regular carbonate-ion; $(HCO_3)^{\bullet}_{CO_3}$ is the new proton conducting species residing on carbonate-ion. From reaction (3-1), it is evident that increasing partial pressure of H_2O can increase the concentrations of $(OH^{\bullet}_{O})$ and $(HCO_3)^{\bullet}_{CO_3}$, ultimately leading to an increase in conductivity by protons. It is also inferred from Figure 3.6 that $(HCO_3)^{\bullet}_{CO_3}$ residing on carbonate-ion is the dominant charge carrier for proton conduction. It is worth mentioning that reaction (3-1) implicates a synergetic proton transfer between BZY and MC, in which both $V^{\bullet\bullet}_{O}$ and $(CO_3)^{\times}_{CO_3}$ play an important role. The details on the proton transfer mechanism will be discussed in the following.

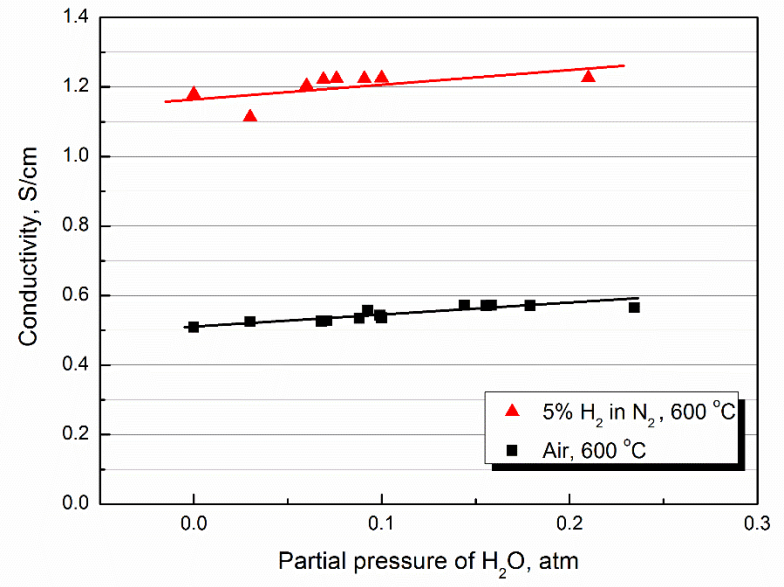

Figure 3.6. Conductivity of LN-BZY composite vs P_{H2O} at 600°C.

3.4.2.5 Conductivity *vs* P_{H_2}

To understand the enhanced conductivity by H_2, the conductivity of LN-BZY composite was measured over a range of partial pressure of H_2 (P_{H_2}) at 600°C; the result is shown in Figure 3.7. Note that the conductivity shown here is lower than that in Figure 3.6. This is caused by the lowered MC loading in the sample, *viz.* 48 vol% for Figure 3.7

vs 57 vol% for Figure 3.6. The defect chemistry reaction leading to the increased concentrations of $(\mathrm{OH}_{\mathrm{O}}^{\bullet})$ and $(\mathrm{HCO}_3)_{\mathrm{CO}_3}^{\bullet}$, and thus the conductivity can be expressed by:

$$H_2 + V_O^{\bullet\bullet} + O_O^{\times} + (CO_3)_{CO_3}^{\times} = (OH)_O^{\bullet} + (HCO_3)_{CO_3}^{\bullet} \qquad (3\text{-}2)$$

here $O_O^{\times}$ is the regular oxygen lattice in BZY. Again, $(\mathrm{HCO}_3)_{\mathrm{CO}_3}^{\bullet}$ is the dominant charge carrier over $(OH)_O^{\bullet}$ because MC is the primary ionic conductor at 600°C. The synergy of proton transfer between BZY and MC phase will be further discussed in the following.

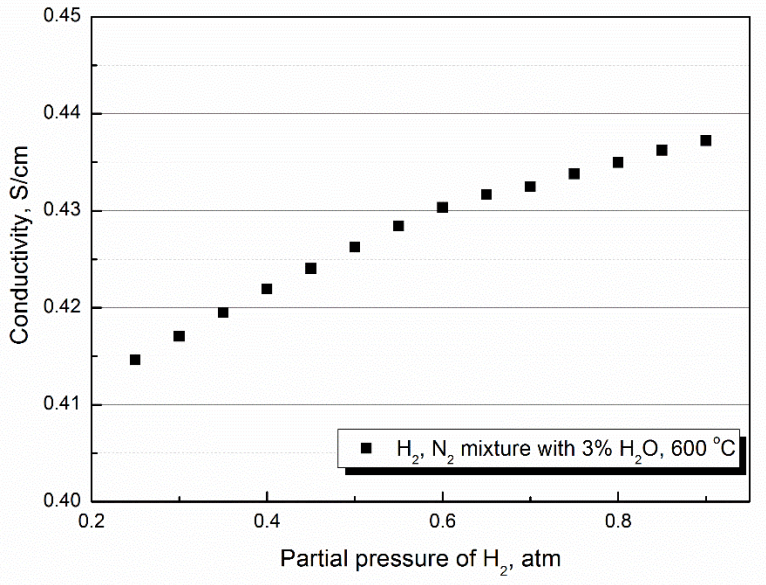

Figure 3.7. Conductivity of a LN-BZY composite vs P_{H2} at 600°C

3.4.2.6 Conductivity in D_2O

To verify whether H in H_2O is one of the proton sources, we measured conductivity in the presence of D_2O. Figure 3.8 compares the conductivities measured in air saturated with 3%H_2O and 3%D_2O. The conductivity difference for the two gases is small but visible, suggesting the nature of proton conduction. As aforementioned, proton species $(\mathrm{HCO}_3)_{\mathrm{CO}_3}^{\bullet}$ is the primary source for the observed enhanced conductivity in both H_2O and H_2 containing atmospheres.

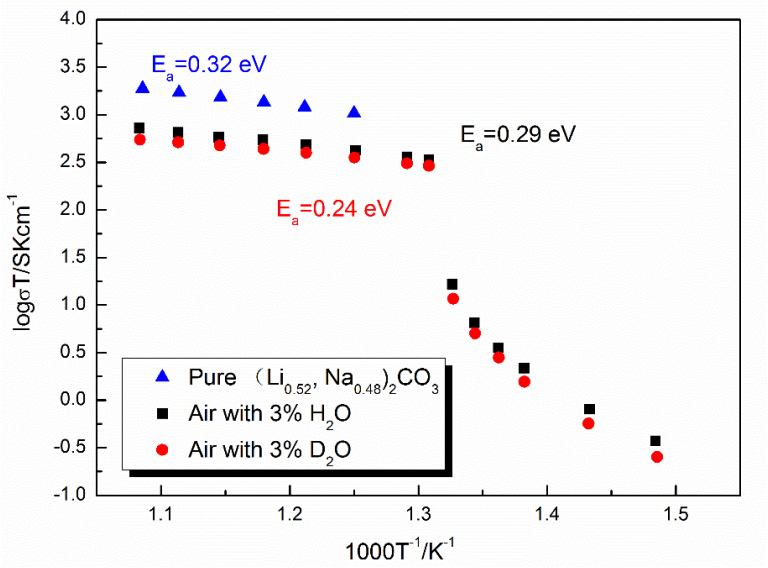

Figure 3.8. Conductivity of LN-BZY *vs* temperature in 3%H_2O-air and in 3%D_2O-air.

As indicated by reaction (3-1) and (3-2), the creation of proton species $(HCO_3)^{\bullet}_{CO_3}$ replies upon the presence of $V_O^{\bullet\bullet}$ and $O_O^{\times}$ in the BZY. In other words, proton transfer across the composite is synergetic between BZY and MC. To illustrate it, Figure 3.9 shows a schematic of the synergetic proton transfer in the atmospheres containing H_2O or H_2 or both. Note that $(HCO_3)^{\bullet}_{CO_3}$ is considered the prime proton conducting species accompanying the major carbonate-ion conduction.

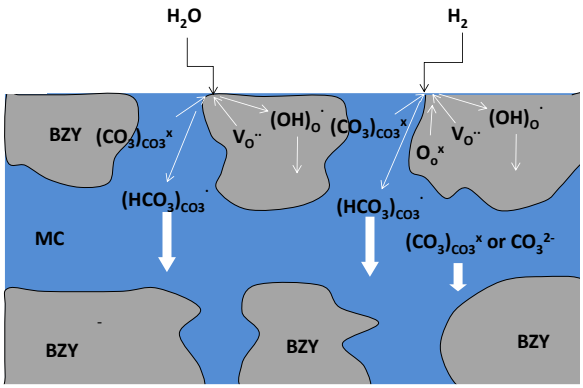

Figure 3.9. Schematic of synergetic proton conduction in BZY-MC composite electrolyte

3.4.3 DFT modeling of MC/BZY enhanced proton conductivity

3.4.3.1 Proton migration in CO_3^{2-} in gas phase HCO_3^-

The optimized structures of CO_3^{2-} and HCO_3^- species are shown in Figure 3.10 (a) and (b). Both structures are in a planar geometry. For CO_3^{2-} of D3h symmetry, the calculated C–O bond lengths are 1.295 Å and O–C–O bond angles are 120°, which are in accord with the literature results of 1.306 Å and 1.309 Å. Addition of proton to the CO_3^{2-} forms planar HCO_3^- of C_s symmetry, where the bond angle of H–O–C is 101.2° and the bond length of O–H is 0.976 Å.

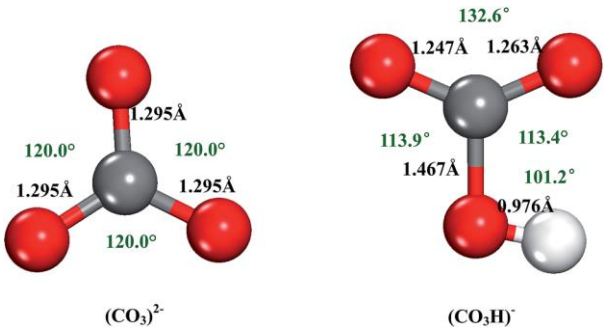

Figure 3.10. The optimized structures of CO_3^{2-} and HCO_3^- species. The grey, red, and white balls represent the carbon, oxygen, and hydrogen atom, respectively.

Figure 3.11 (a) and (b) indicate the H^+-migration in a CO_3^{2-}. There are two representative motions: planar transfer between two oxygen atoms and rotation along one oxygen atom. The first motion is shown in Figure 3.11 (a), where H^+ migrates from O1 to O2. During this transfer, the bond between O1 and H^+ is first broken, followed by H^+ moving toward the mirror position between O1 and O2, namely the transition state. The bond between O2 and H^+ is then reformed, completing the H^+-transfer. The energy barrier for this motion was 0.89 eV.

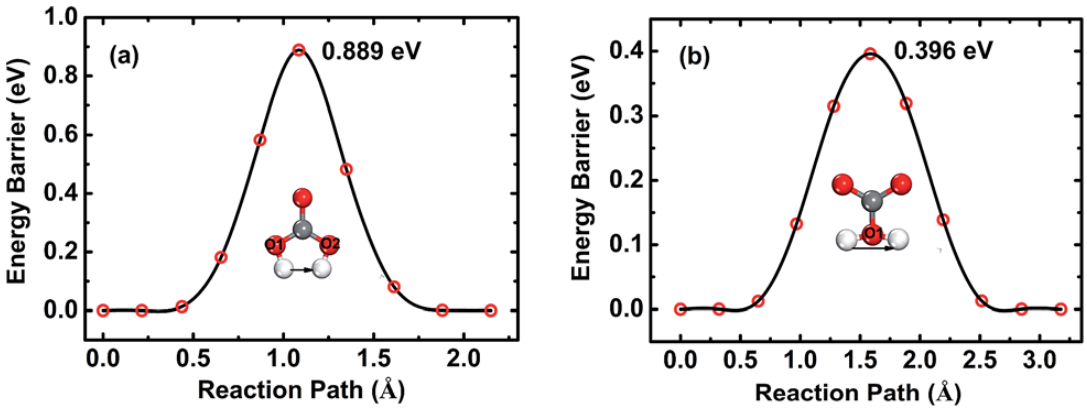

Figure 3.11. The energy barrier of proton transfer in the CO_3^{2-} ionic cluster. (a) H^+-transfer between O1 and O2, (b) H^+-transfer via rotation along the O1. The grey, red, and white balls represent the carbon, oxygen, and hydrogen atom, respectively.

Figure 3.11 (b) shows H^+-rotation around O1 atom. The bond length between O1 and H^+ is fixed to 0.976 Å in the calculation. H^+ rotates from the left side of O1, passes through the transition state above the O1 atom and reach the right side of O1. The calculation reveals the rotation process has an energy battier of 0.396 eV, which is more energetically favorable than the intra-oxygen transfer path. Thus, both paths of low energy barriers imply low thermal energy (or low temperature) for H^+-migration in CO_3^{2-}.

3.4.3.2 Proton migration in Li_2CO_3 crystal

The H^+ migration in solid carbonate was modeled for studying H^+ migration direction. Lithium carbonate (Li_2CO_3) has a monoclinic structure and C2/c space group. The optimized crystal structure of a Li_2CO_3 is shown in Figure 3.12. There are four formula units in a primitive cell shown in Figure 3.12 (a). The calculated lattice parameters are a=8.397 Å, b=5.019 Å, c=6.311 Å; α=90.0°, β=114.5°, γ=90.0°. To simulate the H^+-transfer in Li_2CO_3, a supercell containing a $1 \times 2 \times 2$ cell is constructed and shown in Figure 3.12 (b).

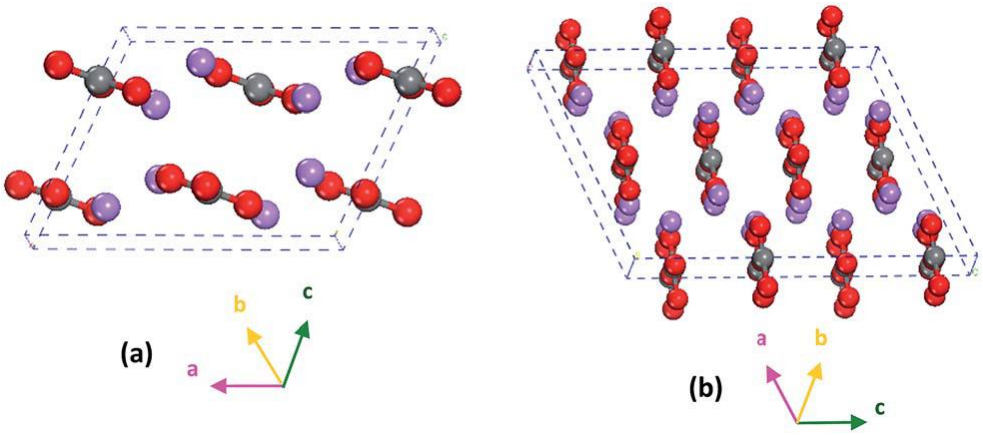

Figure 3.12. The optimized triclinic crystal structure of Li_2CO_3

There are eight representative migration pathways of H^+-transfer along $a[100]$, $-a[\bar{1}00]$, $b[010]$, $-b[0\bar{1}0]$, $c[001]$, $-c[00\bar{1}]$ and $ca[101]$, $-ca[\bar{1}0\bar{1}]$ directions considered, as shown in Figure 3.13-3.16, respectively. Basically, there are three possible motions of H^+ in the crystal: (1) rotation, H^+ rotating around one oxygen ion in a carbonate; (2) intra-carbonate ion transfer, H^+ moving between different oxygen ions in a carbonate; (3) inter-carbonate ion transfer, H^+ moving between different oxygen ions in different carbonates. In Figure 3.13, the possible H^+ locations were marked with small case letter a, b, c, etc. ,and capital T and R indicated H^+ transfer between oxygen and H^+ rotation, respectively. For all the migration paths, the calculated energy barriers are summarized in Tables 3.1-3.3.

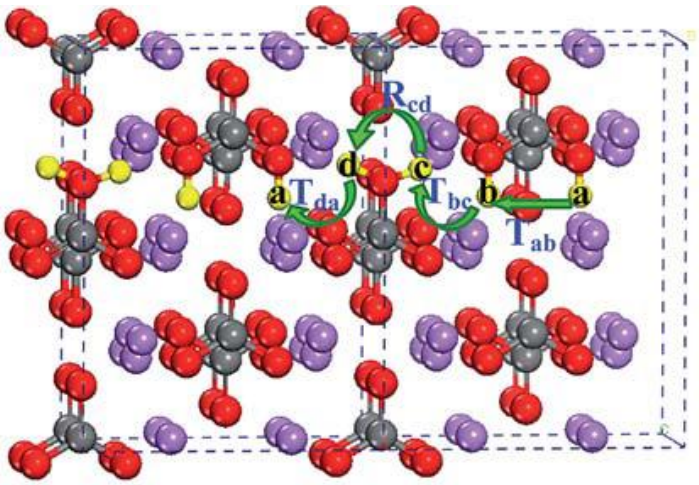

(a) a [100] ← H Li C O

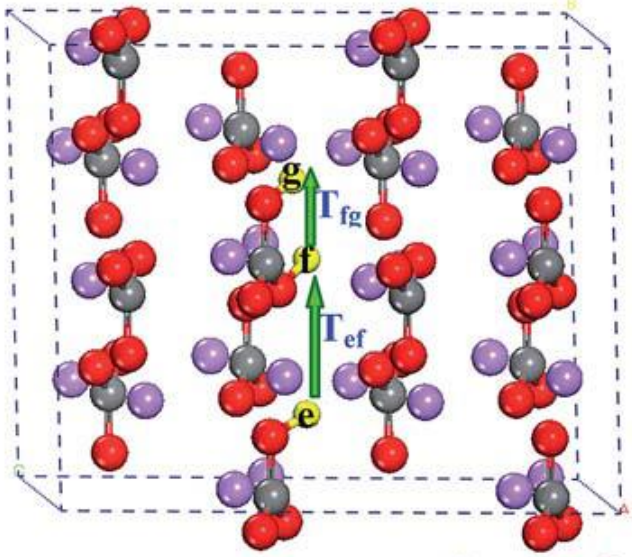

(b) → b [010] H Li C O

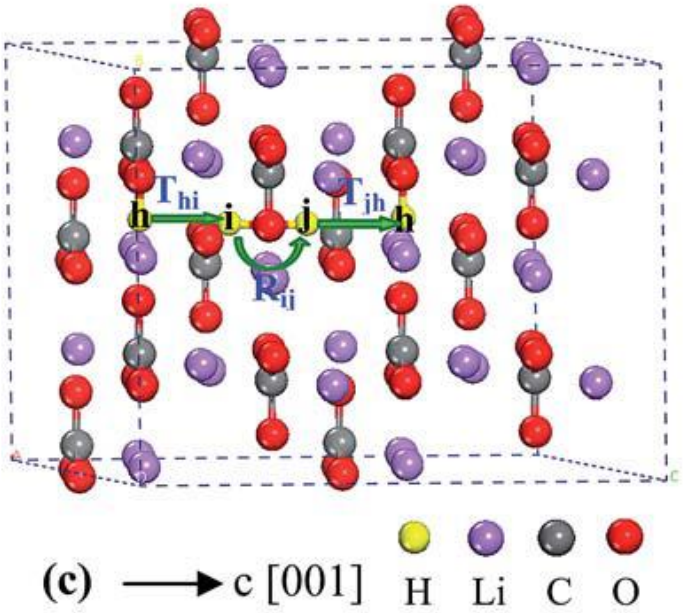

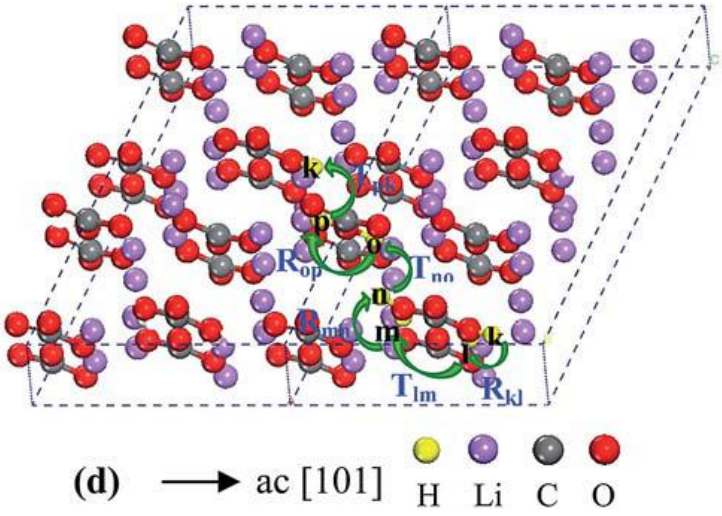

Figure 3.13. Schematic of H^+-transfer along (a)[100], (b) [010], (c)[001] and (d) [101] directions, respectively. The primitive cell is indicated by dashed lines.

For the migration path along $a[100]$, shown in Figure 3.13(a), H^+ moved via four sub steps: intra-carbonate transfer (T_{ab}), inter-carbonate transfer (T_{bc}), rotation (R_{cd}) and inter-carbonate transfer (T_{da}). In Table 3.1, the result shows the highest energy barrier is 0.9 eV and 0.85 eV corresponding to forward and backward direction, respectively.

In path along $b[010]$, shown in Figure 3.13(b), H^+ moved via inter-carbonate transfer (T_{ef}) and intra-carbonate transfer (T_{fg}). From the calculation, the intra-carbonate transfer in $[010]$ had a high energy barrier of 1.10 eV.

In path along $c[001]$, shown in Figure 3.13(c), H^+ moved via three steps: inter-carbonate transfer (T_{hi}), rotation (R_{ij}) and inter-carbonate transfer (T_{jh}). The highest energy barriers are only 0.34 eV along $c[001]$ and 0.48 eV along $-c[00\bar{1}]$, respectively.

In path long $ca[101]$, shown in Figure 3.13(d), H^+ moved via rotation (R_{ij}), intra-carbonate transfer (T_{fg}), rotation (R_{ij}), inter-carbonate transfer (T_{hi}), rotation (R_{ij}), inter-carbonate transfer (T_{hi}). From Table 3.3, path in $[101]$ had a high 1.13 eV energy barriers and 0.91 eV along $[\bar{1}0\bar{1}]$, respectively.

By comparison, $c[001]$ and $-c[00\bar{1}]$ directions are more energetically favorable to H^+ migration in Li_2CO_3 lattice. This preference is due to the crystallographic positions of carbonate ions to the unit cell's *c*-axis. In the unit cell shown in Figure 3.12, carbonate ion plane is perpendicular to c-axis, the direction $[001]$ and $[00\bar{1}]$. It is geometrically convenient for rotational H^+-transfer, and there is enough space for carbonate ions adjusting their position when H^+ transfers between them. Therefore, in other directions, the carbonate ion plane is almost parallel, which makes H^+ prefer to transfer between oxygen atoms other than rotation. This result corresponds well to the previous calculation of H^+ transfer in single carbonate ion.

Table 3.1 Energy barriers of H^+ migration along $a[100]$ and $-a[\bar{1}00]$ directions

$a[100]$	T_{ab}	T_{bc}	R_{cd}	T_{da}
Energy Barrier (eV)	0.85	0.78	0.58	0.90

$-a[\bar{1}00]$	T_{ad}	R_{dc}	T_{cb}	T_{ba}
Energy Barrier (eV)	0.79	0.58	0.84	0.85

Table 3.2 Energy barriers of H^+ migration along $\boldsymbol{b}[\mathbf{010}]$ and $-\boldsymbol{b}[\mathbf{0\bar{1}0}]$ directions

$b[010]$	T_{ef}	T_{fg}
Energy Barrier (eV)	0.37	1.10
$-b[0\bar{1}0]$	T_{gf}	T_{fe}
Energy Barrier (eV)	0.83	0.60

Table 3.3 Energy barriers of H^+ migration along $\boldsymbol{c}[\mathbf{001}]$ and $-\boldsymbol{c}[\mathbf{00\bar{1}}]$ directions

$c[001]$	T_{hi}	R_{ij}	T_{jh}
Energy Barrier (eV)	0.33	0.20	0.34
$-c[00\bar{1}]$	T_{hj}	R_{ji}	T_{ih}
Energy Barrier (eV)	0.21	0.48	0.18

Table 3.4 Energy barriers of H^+ migration along $\boldsymbol{ac}[\mathbf{101}]$ and $-\boldsymbol{ac}[\mathbf{\bar{1}0\bar{1}}]$ directions

$ca[101]$	R_{kl}	T_{lm}	R_{mn}	T_{no}	R_{op}	T_{pk}
Energy Barrier (eV)	1.13	0.84	0.32	0.11	0.49	0.02
$-ca[\bar{1}0\bar{1}]$	T_{kp}	R_{po}	T_{on}	R_{nm}	T_{ml}	R_{lk}
Energy Barrier (eV)	0.12	0.49	0.02	0.54	0.84	0.91

3.4.3.3 Proton migration in $(Li_2CO_3)_8$ cluster

Since the study considers molten carbonate, a $(Li_2CO_3)_8$ cluster representing the disordered molten carbonate model was built to calculate H^+ transfer energy, shown in Figure 3.14. Firstly, $(Li_2CO_3)_8$ cluster was rationally optimized. In the cluster, each Li^+ is bonded to three O^{2-} from different carbonate ions, while each O^{2-} is bonded to two Li^+. This coordination is corresponding to the crystal structure of Li_2CO_3. After optimization, the average bond length between Li^+ and O^{2-} is 1.948 Å, which is very close to experimental values of 1.960 Å[237]. Besides, an *ab initio* molecular dynamics (AIMD) study found that the volume expansion of Li_2CO_3 is only 3% at 1300 K (theory melting point is about 1000 K), hence the calculated Li-O bond length can be used in the molten carbonate.

The H^+ migration in $(Li_2CO_3)_8$ cluster was then modeled. The migration process begins from breaking the bond between Oa and H^+, and ends with building the bond between Ob and H^+, as shown in Figure 3.14. With the confirmed transition state, intrinsic reaction coordinate (IRC) method was used find the reaction route to finalize accurate structures of reaction and product, as shown in Figure 3.14 (b) and (d). The H^+ marked in white color bonds with Oa as the reactant and bonded with Ob as the product. The IRC calculations specify that the bond between H^+ and Oa is slightly elongated from 1.018 Å to 1.237 Å with an energy barrier of 0.08 eV. The conversion from TS into product is rather quick. The H^+ separates from Oa and moves towards Ob. Meanwhile, the bond length of H^+-Oa increases from 1.237 Å to 1.399 Å, whereas the bond length of H^+-Ob reduces from 1.170 Å to 1.069 Å, thus completing a single H^+-transfer process. Besides, the low energy barrier from TS to product suggests a reversible H^+ migration, which reveals H^+ migration in molten carbonate is very feasible.

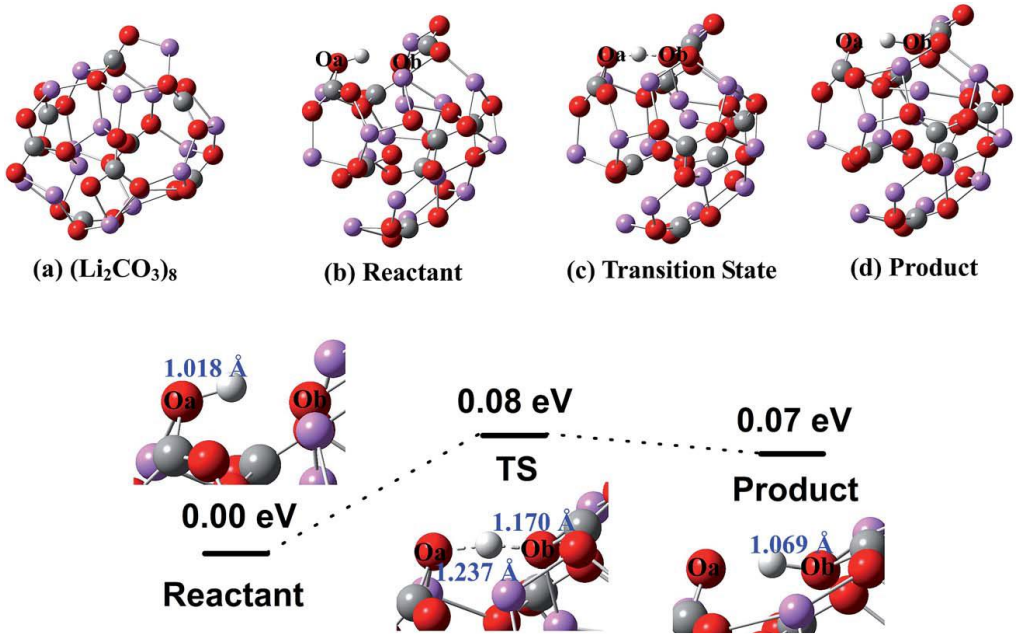

Figure 3.14. The schematic of (a) $(Li_2CO_3)_8$ cluster and the structural states of (b) beginning, (c) transitioning and (d) ending phases of H^+ transfer in a $[(Li_2CO_3)_8H]^+$ cluster with the relative energies. The purple, grey, red, and white balls represent the lithium, carbon, oxygen, and hydrogen atom, respectively.

3.4.4 DFT modeling of interfacial proton migration between BZY and molten carbonate

3.4.4.1 Adsorption of proton on the ZrO_2-terminated surface

The structure of BZY was first optimized, yielding a lattice constant of 4.25 Å, which is in good agreement with the experimental 4.20 Å [238] and theoretical 4.24 Å [239]. Proton adsorption site was examined on the ZrO_2-terminated surface. There were five available adsorption sites, as shown in Figure 3.15 (a) on the top of O atom (upright), T_O, (b) on the top of O atom (tilted toward Zr atom), $T_{O\text{-}Zr}$, (c) on the top of O atom (tilted toward hollow site), $T_{O\text{-}hollow}$, (d) on the top of Zr atom (upright), T_{Zr}, (e) on the top of hollow site, T_{hollow}. After a full relaxation, the results show that $T_{O\text{-}hollow}$ (Figure 3.15(c)) is the most favorable adsorption site, which agrees with the hypothesis of the proton defects formation [240]. On

this site, proton forms covalent bond with the lattice oxygen atom titling toward the hollow site, at which the proton has a short distance between its adjacent oxygen atoms, which forms a stable adsorption.

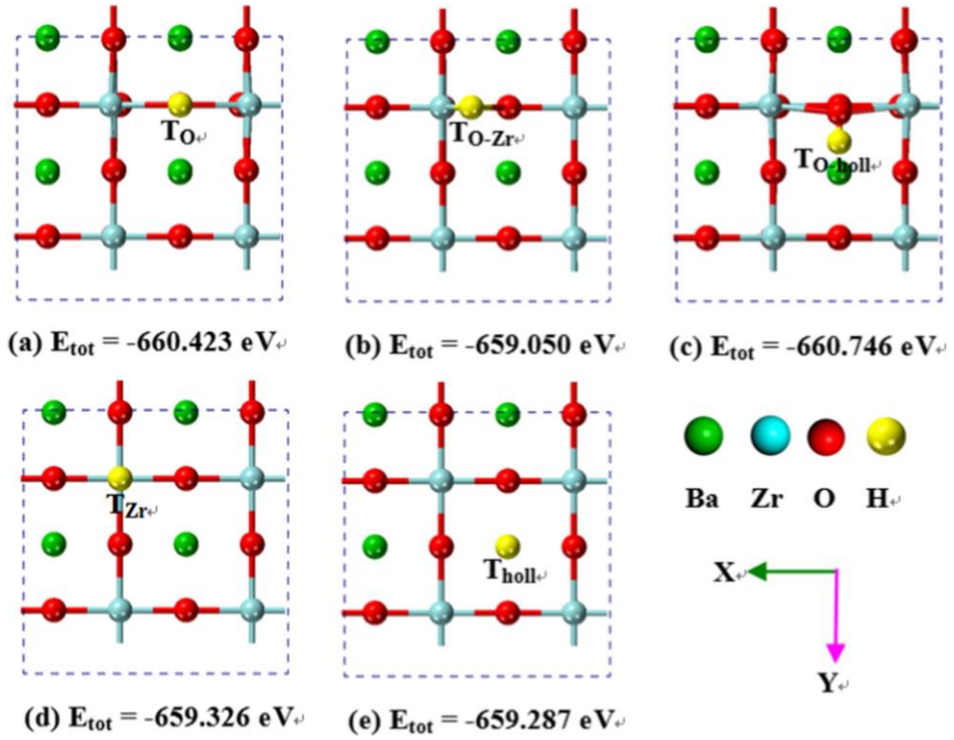

Figure 3.15. The optimized structures (top view) with total energy of proton adsorbed on ZrO_2-terminated surface (100). (a) on the top of O atom (upright), T_O, (b) on the top of O atom (tilted toward Zr atom), $T_{O\text{-}Zr}$, (c) on the top of O atom (tilted toward hollow site), $T_{O\text{-}hollow}$, (d) on the top of Zr atom (upright), T_{Zr}, (e) on the top of hollow site, T_{hollow}.

3.4.4.2 Proton migration on the ZrO_2-terminated surface

Since DFT packages are not able to treat the electronic state of proton separately from the supercell, which means that charge can only be applied to the whole cell. Before modelling proton migration path, it is necessary to examine the charge impact to the system. The tests were two NEB calculations of proton rotation around an oxygen atom with one positive charge and without charge. The results show ab energy barrier of 0.34 eV with charge and 0.33 eV without charge, which are almost identical. Hence, it is reasonable to apply one positive charge evenly on the system.

Figure 3.16 shows possible migration pathways and corresponding energy profiles along X-direction (a, b), Y-direction (c, d), XY direction (e). In X-direction, two routes were considered, linear path 1 to 2 (Path-1) and curved path 1 to 3 to 4 to 2 (Path-2), as shown in Figure 3.16 (a) and (b), respectively. Path-1 is a one-step transfer having an energy barrier as high as 1.660 eV. Path-2 includes three steps: I and III refer to proton moves between adjacent oxygen atoms with a sequential O-H^+ bond breaking and reforming, with an energy barrier of 0.567 eV; II refers to proton rotation around an oxygen atom maintaining the O-H^+ bond, with an energy barrier of 0.326 eV. Thus, Path-2 has the overall energy barrier of 0.567 eV, which agrees with the measured activation energy of 0.3 – 0.65 eV for H^+ transfer in $BaZrO_3$ and BZY [241-243]. Besides, the H^+ transfer is the rate-determining step, which is supported by other studies [241, 244-246]. Hence, the curved path is more favorable for H^+ migration along the X direction.

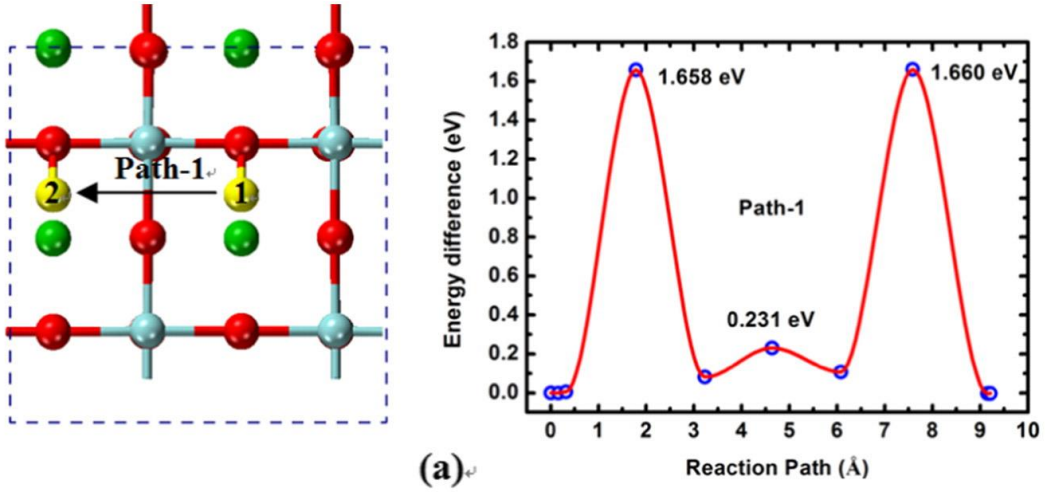

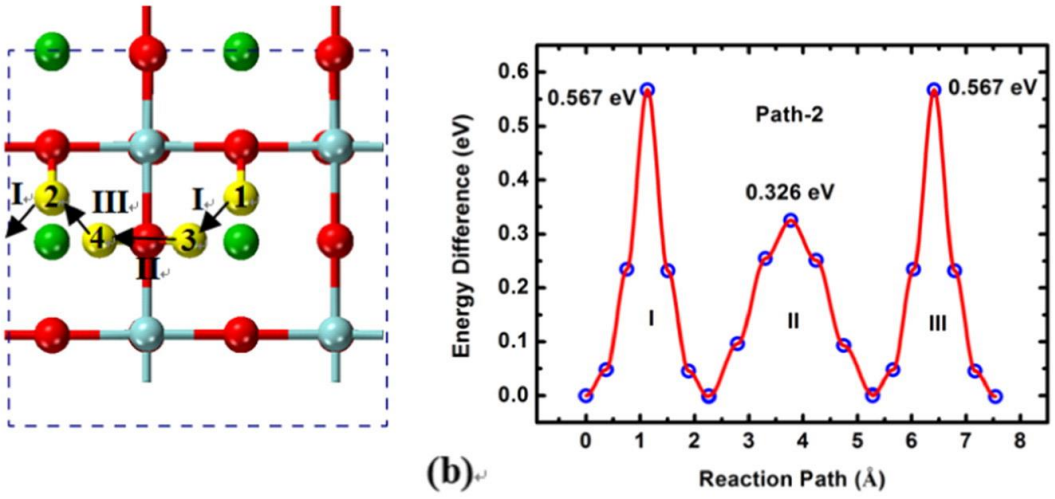
I
2
III
I
1
4
3
II
0.567 eV
Path-2
0.326 eV
0.567 eV
Energy Difference (eV)
Reaction Path (Å)

(b)

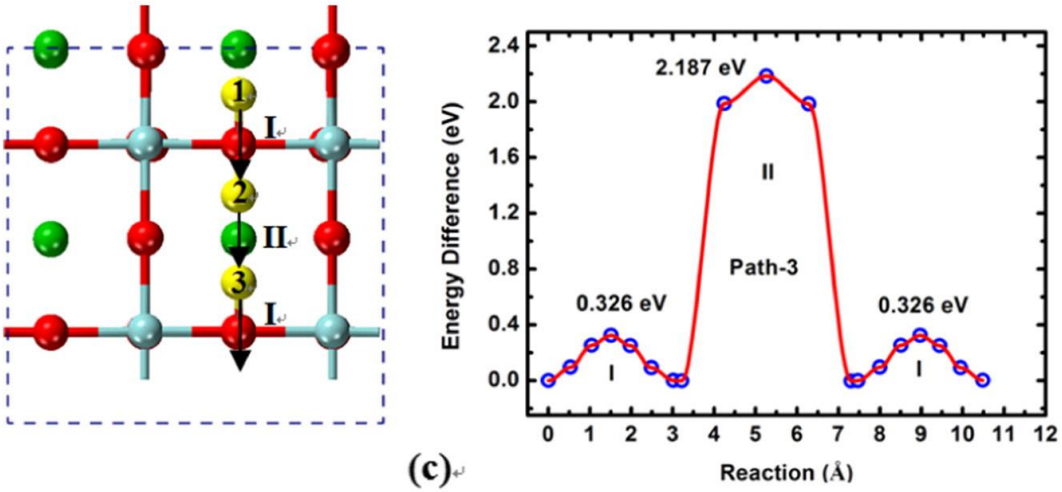
1
I
2
II
3
I
2.187 eV
II
Path-3
0.326 eV
0.326 eV
Energy Difference (eV)
Reaction (Å)

(c)

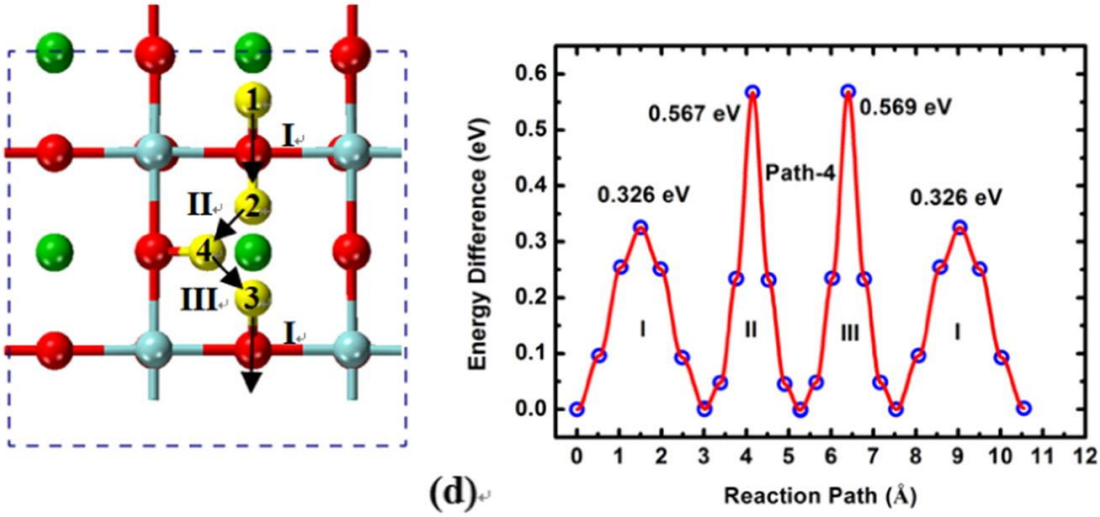
1
I
II
2
4
III
3
I
0.567 eV
0.569 eV
Path-4
0.326 eV
0.326 eV
Energy Difference (eV)
Reaction Path (Å)

(d)

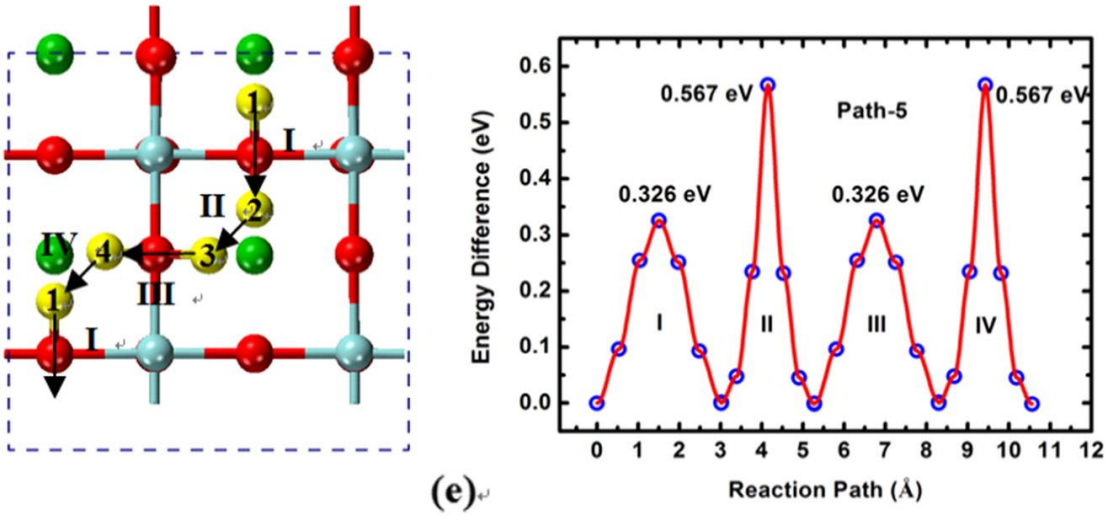

Figure 3.16. Migration pathways and energy profiles for H+ migration along X direction (a and b), Y direction (c and d), and XY direction (e). The migration pathways are marked with arrows.

In the Y direction, there are also two pathways, marked as Path-3 and Path-4, as shown in Figure 3.16 (c) and (d). In Figure 3.16 (c), Path-3 includes a H^+ rotation step (I) and then a transfer step (II) via the top of hollow site. From the calculation, step (I) has a low energy barrier of 0.326 eV. However the transfer step (II) has a very high energy barrier of 2.187 eV, which prohibits H^+ migration. On the other hand, Path-4 in Figure 3.16 (d) consists of a H^+ rotation step and two transfer steps having the same energetic profiles as Path-2 due to the cubic crystal structure. Thus, the curve path in Y direction is also the preferred pathway for H^+ migration.

In the viewpoint of symmetry, XY direction as the Path-5 was also considered, as shown in Figure 3.16 (e). Such pathway includes two H^+ rotation steps (I and III) and two H^+ transfer steps (II and IV). Obviously, it is also limited by the transfer steps no matter how many steps are consisted. Hence, the overall energy barrier is also 0.569 eV.

Overall, H^+ migration on ZrO_2-terminated (100) surface prefers a curved pathway containing a proton rotation and transfer as the elementary steps.

3.4.4.3 Proton migration on the ZrO_2-terminated surface with Y-doping

Proton migration on Y-doping ZrO_2-terminated (100) surface was also modeled. Substitution of Zr by Y introduces oxygen vacancies, where the proton defect forms. The dopant ion and oxygen vacancy can form defect clusters. In a neutral trimer cluster, there is two possible oxygen vacancy positions: nearest and a distant V site. The calculated energy of cluster with a distant V site is 0.227 eV higher than the closest situation. Hence, only the closest V site next to Y was considered. The model of Y-doping ZrO_2-terminated (100) surface is shown in Figure 3.17 (a). The oxygen vacancy was created in OA site and occupied by OH^-. Thus, H^+ migrated from the OH^-. As concluded in previous section, H^+ migration of curve pathway has the lowest energy barrier. Thus, the pathway on Y-doping ZrO_2-terminated (100) surface was along Y-direction via 1 to 2 to 3 to 4 to 5 position. The four steps are: step I and IV for H^+ rotation around OA and OB; step II and III for H^+ transport between adjacent OA, OA and OB, respectively. The calculated energy profiles of four steps are 0.266, 0.533, 0.523 and 0.340 eV, respectively, as shown in Figure 3.17(b). The total energy barrier of 0.533 eV is very close to 0.567 eV of pure $BaZrO_3$. Hence, the doping of Y has mere effect on the energy barrier of H^+ migration on ZrO_2-terminated (100) surface. Using pure ZrO_2-terminated (100) surface to study MC effect on H^+ migration is reasonable.

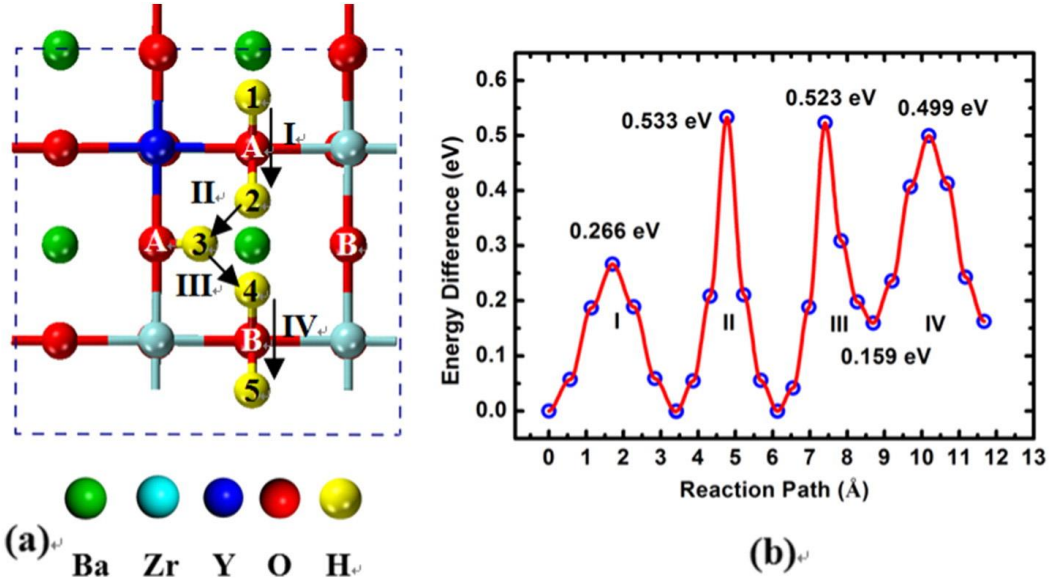

Figure 3.17. Migration pathways and energy profiles for H^+-migration along Y direction at Y-doped ZrO_2-terminated (100) surface.

3.4.4.4 Proton migration at the ZrO_2-terminated surface/MC interface

To understand the enhanced proton conductivity phenomenon in MC/BZY composite, H^+ migration through the interface between MC and ZrO_2-terminated (100) surface were modeled. Firstly, the stable adsorption position of carbonate ion should be found. Figure 3.18 (a) to (c) shows a carbonate ion was adsorbed on the ZrO_2-terminated (100) surface with different tilt angles. The calculated adsorption energies indicate the parallel configuration has the lowest energy compared by the titled and vertical configurations. Then, a model of four carbonate ions on the unit cell was optimized to study the coverage adsorption structure, as shown in Figure 3.18 (d). The calculated structure shows the coverage of carbonate ions on ZrO_2-terminated (100) surface could be high enough to provide sufficient bridging for protons transport and the plane of carbonate ions would slightly title up, which is different from the single carbonate ion. However, the co-adsorption of carbonate is a dynamic process occurring at high temperature. Thus, the adsorption structure with the lowest energy would be prevalent.

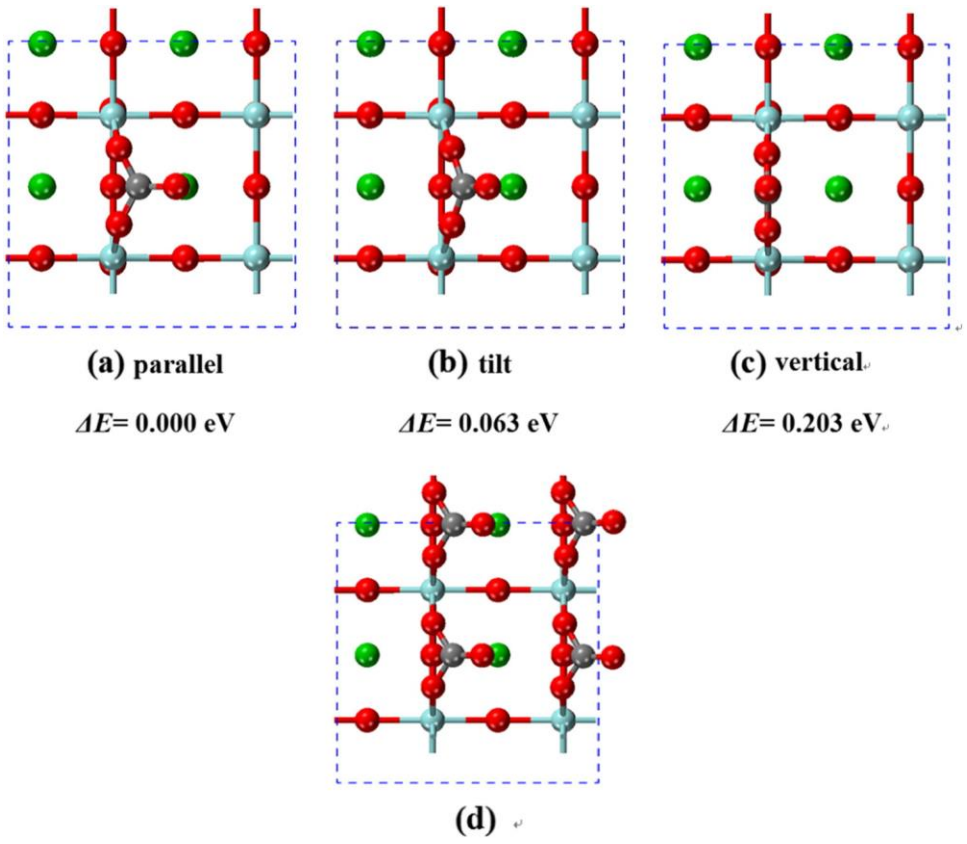

Figure 3.18. The optimized adsorption structures and relative energy.

To verify the effect of MC, the H^+ migration along Y-direction on MC and ZrO_2-terminated (100) interface was designed to compare with the energy barrier of H^+ migration along Y-direction on pure ZrO_2-terminated (100) interface, as shown in Figure 3.19 (a) and (b). The pathway has four steps: step I for H^+ rotation around an oxygen atom of ZrO_2-terminated (100); step II for H^+ transfer from ZrO_2-terminated to carbonate ion; step III for H^+ rotation around an oxygen of carbonate ion; step IV for H^+ transfer from carbonate ion to ZrO_2-terminated (100) surface. In this pathway, the carbonate ion acts like a bridge linking proton position 1 and 2. Figure 3.19 (c) shows the calculated energy barriers for each steps, 0.326 eV (I), 0.281 eV (II), 0.332 eV (III) and 0.061 eV (IV), respectively. Thus, the step III of H^+ rotation in carbonate ion becomes the rate limiting step and the overall

energy barrier is 0.332 eV. Compared to the energy barrier of H^+ migration without MC, the carbonate ion significantly reduced the energy barrier from 0.567 eV to 0.332 eV by alternating the H^+ transfer of high energy barrier with H^+ rotation in carbonate ion of low energy barrier. More importantly, the result is in excellent agreement with the activation energy of 0.33 eV obtained from the conductivity measurement of MC/BZY composite.

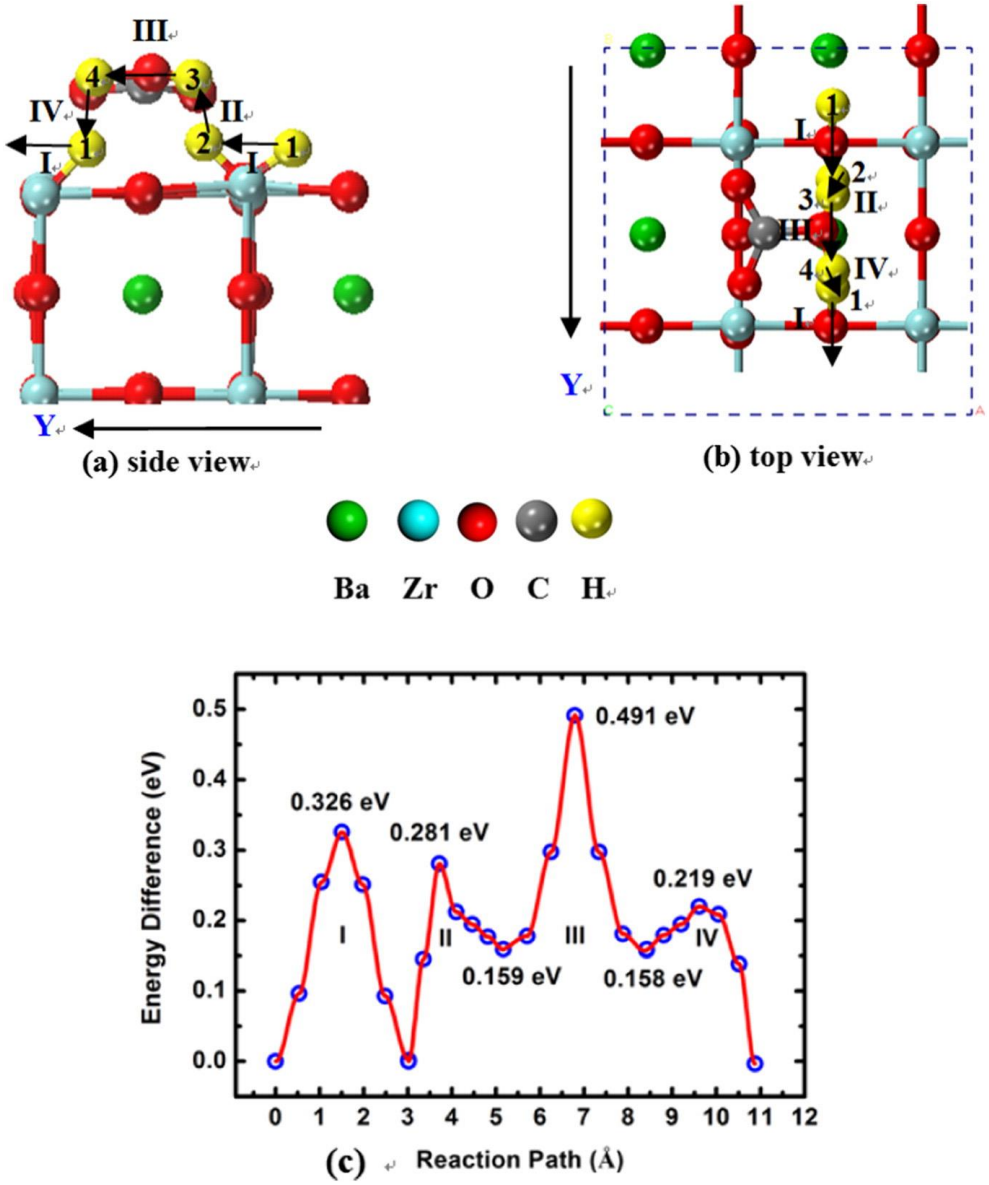

Figure 3.19. Migration pathways along Y-direction with the aid of molten carbonate, (a) is side view and (b) is top view and energy profiles (c) for proton migration.

3.5 Conclusion

The MC-BZY composite electrolyte has been evaluated experimentally and computationally to understand the enhanced conductivity and improved SOFC performance. The ionic conductivity of the composite above 500^{o}C was affected by the loading and type of MC. More importantly, the sample exhibited nearly a factor of two higher conductivity in H_2-containing atmosphere than in air. The dependences of conductivity on partial pressures of H_2 and H_2O, as well as the type of H (H *vs* D) suggested that proton conduction can take place, primarily in the MC phase. A defect chemistry model was proposed to explain the synergetic proton transfer between BZY and MC phases.

First-principles DFT modeling further investigated proton transfer in a carbonate ion, lithium carbonate crystal and lithium carbonate cluster. The results show that proton rotation around an oxygen of carbonate ion is more energetically favorable than transfer between oxygen atoms, revealing the feasible path of proton migration relying on the orientation of carbonate ions. The migration pathways in lithium carbonate crystal were also modeled. The calculated energy profiles showed that the [001] and [00$\bar{1}$] directions (along *c*-axis) were the lowest energy barrier pathways, which was originated from the crystallographic orientation of carbonate ion perpendicular to *c*-axis, further facilitating proton rotation. The $(Li_2CO_3)_8$ cluster model was used to simulate the disordered molten carbonates. The calculated energy profile showed an extremely low proton migration energy barrier.

The proton migration at the interface of $BaZrO_3$ and molten carbonate were also studied. At ZrO_2-terminated (100) surface of $BaZrO_3$, proton moves via a curved path with an energy barrier of 0.567 eV and the effect of dopant Y on the energy barrier for proton

migration is very small, only lowering the energy barrier by 0.034 eV. With the presence of carbonate ion, proton migration energy barrier becomes as low as 0.332 eV, which agrees well with the activation energy of 0.33 eV obtained by the experiment. The modeling indicates the reduction of energy barrier is resulted from the change of rate-determining step from proton transfer between oxygen atoms to proton rotation around oxygen atom.

CHAPTER 4

CATHODE CATALYTIC PROMOTION BY MOTLEN CARBONATE

4.1 Introduction

As an effort to reduce ORR polarization for IT-SOFCs, molten carbonate (MC) was studied as a catalytic promoter. The hypothesis is that the high oxygen solubility in MC can enhance the adsorption and diffusion of oxygen species, thus further enhance the ORR activity. A range of cathode materials including Ag, Au, $La_{0.8}Sr_{0.2}MnO_{3-\delta}$ (LSM), $La_{0.6}Sr_{0.4}Co_{0.2}Fe_{0.8}O_{3-\delta}$ (LSCF) and $La_2NiO_{4+\delta}$ was added with a controlled amount of MC, followed by symmetrical cell EIS analysis. To evaluate the effect, baseline cells without MC addition were also measured alongside of the MC-added cells.

A number of DFT models have also been built, based on which energetics of oxygen-species migration have also been calculated to support the experimental observations.

4.2 Experimental

Fabrication of symmetrical cells. Symmetrical cells consist of two identical thin porous cathode layers separated by a dense 400 micron thick electrolyte membrane. For gold and silver cathodes, yttrium stabilized ZrO_2 (YSZ) was used as the electrolyte, while for LSM, $La_2NiO_{4+\delta}$ and LSCF with the electrolyte was $La_{0.8}Sr_{0.2}Ga_{0.83}Mg_{0.17}O_{3-\delta}$ (LSGM). The YSZ electrolyte was made from a commercial powder (TZ-8Y, TOSOH Corporation).

The LSGM electrolyte membrane was fabricated by a traditional solid state route. Both powders were pressed into pellets, sintered at 1450 ^{0}C for 5h and finally polished to the required thickness.

The gold and silver porous electrodes were made by screen printing commercial pastes (Heraeus) on both sides of the YSZ electrolyte. After drying in the oven for 12h. The three-layer symmetrical cells were fired at 850 ^{o}C for 10 min for Au and at 500 ^{o}C for 30 min for Ag.

The LSM powder was synthesized by a sol-gel route. $La(NO_3)_3\,6H_2O$ (Alfa Aesar), $Sr(NO_3)_2$ (Alfa Aesar) and $Mn(NO_3)_2\,6H_2O$ (Alfa Aesar) were mixed in a desirable stoichiometry with citric acid and dissolved in deionized water. The molar ratio of metal ions to citric acid was 1:2. Once a clear solution was obtained, the solution was heated to 90^{o}C until the gelation occurred. The gel was further ignited around 200^{o}C. The powder was finally fired at 900^{o}C to achieve a pure and fine LSM powder. The LSM powder was then mixed with organic binder (V-006, Heraeus) to form a uniform slurry. It was screen printed on both side of an LSGM pellet. After drying in the oven for 12h, they were co-fired at 1100 ^{o}C for 2h. Silver paste (Heraeus) and silver meshes were used as current collectors.

$La_2NiO_{4+\delta}$ powder was also synthesized by a sol-gel route. $La(NO_3)_3\,6H_2O$ (Alfa Aesar) and $Ni(NO_3)_2\,6\,H_2O$ (Alfa Aesar) were mixed in a desirable stoichiometry with citric acid and dissolved in deionized water. The molar ratio of metal ions to citric acid was 1:2. Once a clear solution was obtained, the solution was heated to 90^{o}C until the gelation occurred. The gel was further ignited around 200^{o}C. The powder was first fired at 800^{o}C, then grounded and fired at 1000^{o}C again to achieve a pure and fine powder. The powder was

then mixed with organic binder (V-006, Heraeus) to form a uniform ink. It was finally screen printed on both side of an LSGM pellet. After drying in the oven for 12h, they were finally co-fired at 1100^{o}C for 2h. Silver paste (Heraeus) and silver meshes were used as current collectors.

A LSCF commercial ink (fuelcellmaterials) was screen printed on both side of an LSGM pellet. After drying in the oven for 12h, they were co-fired at 1100^{o}C for 2h. Silver paste (Heraeus) and silver meshes were used as current collectors.

Incorporation of Li/Na molten carbonate into porous electrode/cathode were done by two infiltration routes with different precursors. One precursor was aqueous solution of carbonates. In brief, the Li/Na eutectic was prepared by mixing lithium carbonate (99%,Alfa Aesar) and sodium carbonate (99.5%, Fisher Scientific) in the eutectic composition (Li/Na=52/48 in mol%) and melting at 600^{o}C for 1h. The melted carbonate was then milled into fine powders and dissolved in deionized water into a precursor solution for infiltration. A required amount of carbonate precursor solution was infiltrated into the above cathodes of symmetrical cells under vacuum. After the infiltration, the samples were dried out at 100^{o}C overnight. The carbonate loading was controlled by varying concentration of the precursor solution and number of infiltration-drying steps. Another precursor was oxalate aqueous solution. In brief, the Li/Na oxalates were weighted in the molar ratio, Li/Na=52/48, and dissolved in deionized water with the cation concentration of 0.1 mol/L. The infiltration was then carried out dropwise with the oxalate solution on the top of the porous electrode, letting the solution soak into the porous structure, drying, and heating the sample at 550 ℃ in air for 1 h to form carbonate particles after thermal decomposition of acetates. The sample mass before and after each

infiltrating–drying–heating cycle was measured by a balance to determine carbonate loading, which was expressed as the mass ratio of the impregnated material to the porous electrode.

4.3 Computational methods

4.3.1 Calculations of oxygen dissociation in molten carbonate

Calculations were performed in the Gaussian09 suite of quantum programs. Local minimum structures were optimized using the generalized gradient approximation (GGA) based hybrid functional of B3LYP[247, 248] combined with the all electron basis sets and polarization functions of 6-31G(d)[249-252]. The vibrational frequencies were calculated at the same theoretical level, ensuring that the reactant and product structures are located at a true minimum on the potential energy surface (PES), and the transition state is a first-order saddle point on PES as well. The atomic polar tensor (APT) charges were computed through frequency calculations. All resulting energies include the zero-point energy (ZPE) corrections.

4.3.2 Calculations of migration of oxygen in carbonate ion

Calculations of oxygen migration in carbonate were performed in Gaussian09 suite of quantum programs. Local minimum structures were optimized at the generalized gradient approximation (GGA) based hybrid functional of B3LYP[247, 248] combined with all electron basis sets and polarization functions of 6-31G(d).[249-252] The same theoretical level was applied on the vibrational frequencies calculation to verify reactant and product structures being at the true minimum on the potential energy surface, and the transition state is the first-order saddle point on potential energy surface as well. The atomic polar tensor (APT) charges were computed through frequency calculations.

4.3.3 Calculations of dissociation of oxygen and CO_4^{2-} on Ag

Calculations were performed by the Vienna *Ab Initio* Simulation Package (VASP), version 5.3. The projector-augmented wave (PAW) method was used for calculating core and valence electron interactions and the Perdew-Burke-Ernzerhof (PBE) form of the generalized gradient approximation (GGA) was used for the exchange-correlation interaction.

For calculations of oxygen and CO_4^{2-} dissociation on Ag (111) surface, a $5 \times 5 \times 1$ Monkhorst-Pack sampling of the Brillouin zone was used. A vacuum layer of 15 Å along the z-axis direction was created to guarantee no interaction between cells. The O $2s^2 2p^4$, C $2s^2 2p^4$, and Ag $4s^2 4p^6 4d^{10} 5s^1$ electron configurations were taken as the valence electron configurations in the calculations. The cutoff energy and force criterion is 500 eV and 0.02 eV/Å, respectively. In addition, the D2 method of Grimme was used to calculate the dispersion interaction between carbonate species and surface, where the cutoff radius for pair interactions, global scaling factor optimized at the PBE and damping parameter were 15.0 Å, 0.75 and 20.0, respectively. The saddle points and migration pathways of the minimum energy were sought by the nudged elastic band (NEB) method. Spin-polarized and dipole corrections have been taken into account.

4.4 Results and Discussion

4.4.1 XRD graphs of synthesized cathode and electrolyte materials

The phase purity of LSM, $La_2NiO_{4+\delta}$ and LSGM was examined by X-ray diffraction (XRD) using a diffractometer (D/max-A, Rigaku, Japan). The XRD patterns shown below confirm that all materials exhibit single phase as expected.

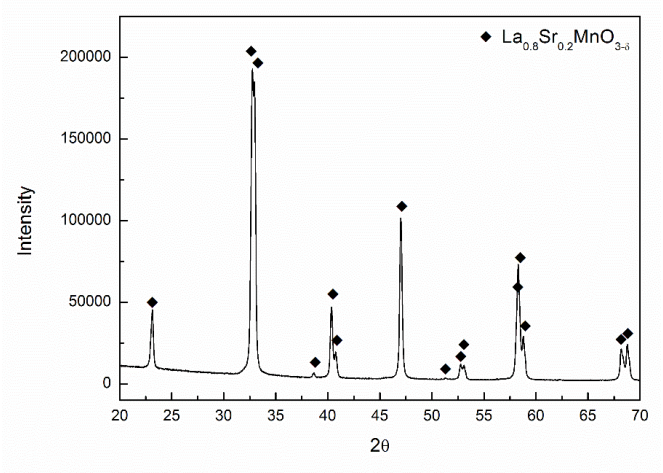

Figure 4.1. XRD pattern of LSM

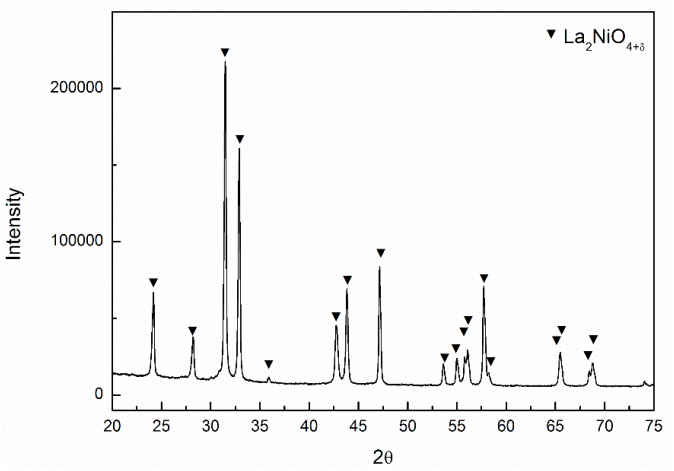

Figure 4.2. XRD pattern of $La_2NiO_{4+\delta}$

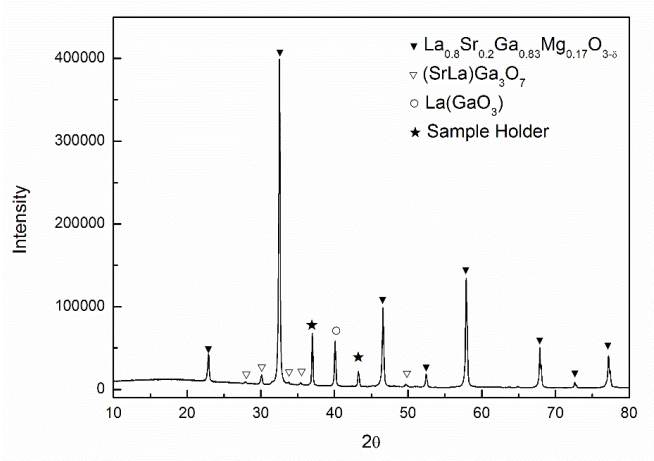

Figure 4.3. XRD pattern of LSGM

4.4.2 Morphology of carbonate and change at elevating temperature

The microstructures and elemental distributions of MC-infiltrated composites were examined by a field emission scanning electron microscopy (FE-SEM, Zeiss Ultra) equipped with an energy dispersive X-ray spectroscopy (EDX) analyzer. Figure 4.4 shows an example of the microstructure after MC-infiltration into LSCF cathode using oxalate precursor. The elemental mappings indicate that the glassy phase is the MC phase and the lighter grain-like phase is the LSCF phase.

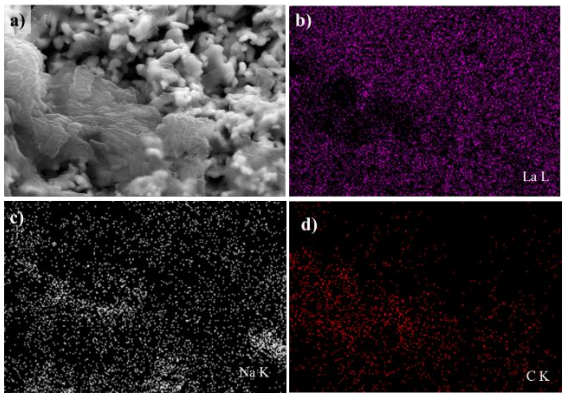

Figure 4.4. Microstructure and elemental distributions of a MC infiltrated LSCF cathode. (a) FESEM image; (b) La mapping; (c) Na mapping; (d) C mapping. Li is too light to be detected by EDX

Figure 4.5 compares the morphology of MC-infiltrated LSCF cathode using two carbonate precursors with different mass loading. In general, there are no significant difference in morphology between the two precursors. The higher MC loading, the more appearance of glassy phase in the microstructure. It is also noted that the carbonate particles are recrystallized in a larger size of few tens micrometers even at a low loading (Figure 4.5(a), (c) and (d)). At higher loading, Figure 4.5(b), the carbonate appears in large and continuous phase.

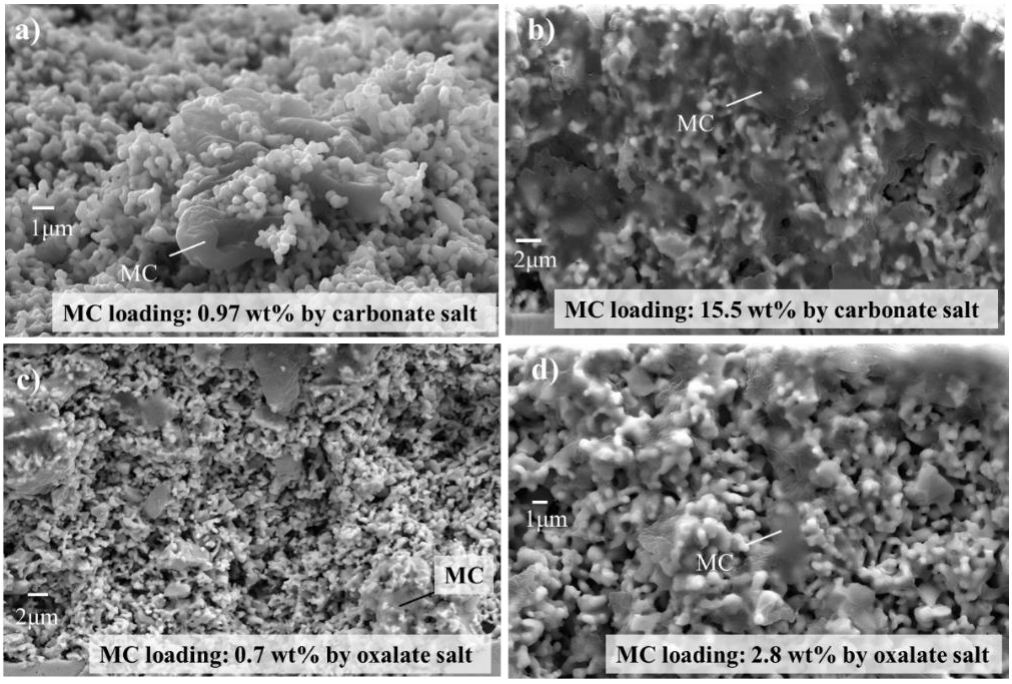

Figure 4.5. SEM images of different MC loading by two precursors: carbonate salt precursor (a) MC loading = 0.97wt%, (b) MC loading = 15.5wt%; Oxalate salt precursor (c) MC loading = 0.7wt%, (d) MC loading = 2.8wt%.

The morphologies of MC-infiltrated LSCF cathode after fired at different temperatures are shown in Figure 4.6. Note that the Li/Na carbonate eutectic mixture (Li/Na= 0.52/0.48) has a melting point around 500ºC.[261] The viscosity of molten carbonate depends on the degree of temperature above the melting point. While the sample was heated up above the melting temperature, Figure 4.6 (b) and (c) show no obsvious difference in the distribution of carbonate phase at 550ºC and 600ºC dwelling for 5 hours. However, at 650ºC for half hour, a part of carbonate phase was found disappeared from the original sites and some nanosized carbonate particles were found precipitated out at the interface of electrolyte and cathode as shown in Figure 4.6(d).

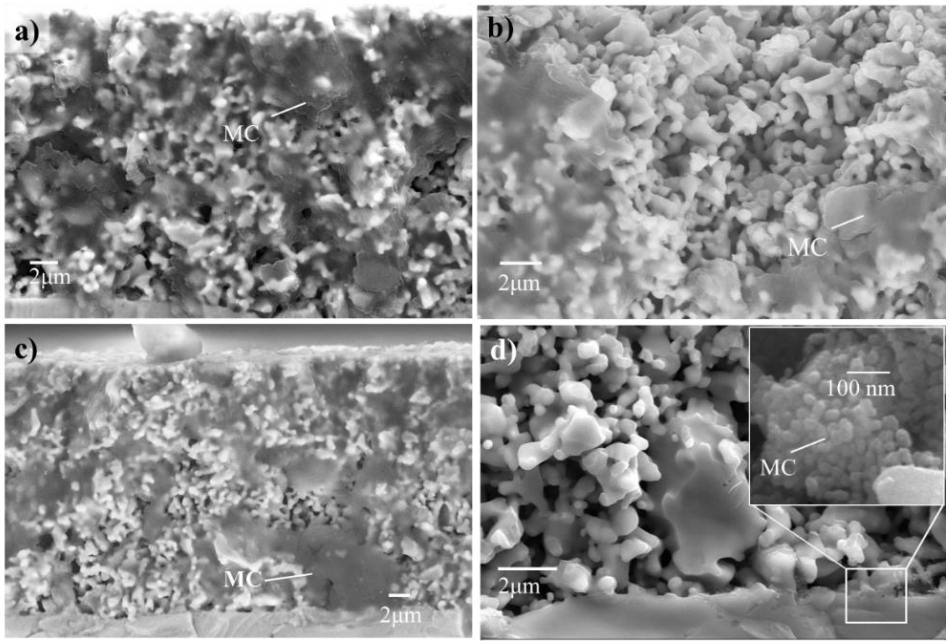

Figure 4.6. SEM images of MC (loading = 15.5wt%) in LSCF at a) room temperature, b) 550^{o}C dwelling for 5 hour, c) 600^{o}C dwelling for 5 hour, d) 650^{o}C dwelling for 0.5 hour.

The effect of thermal history of the cell is shown in Figure 4.7, where EIS spectra of a MC-LSCF cathode after two thermal excursion are displayed. It appears that the polarization resistance (R_P) is lower for the case of direct ramping up from 500^{o}C to 600 ^{o}C than that ramping down from 650^{o}C. There is an obvious change in high-frequency spectrum, which suggests carbonate aggregation or lost had occurred. The observation suggests that the operating temperature for Li/Na-MC-infiltrated LSCF should be below 600^{o}C.

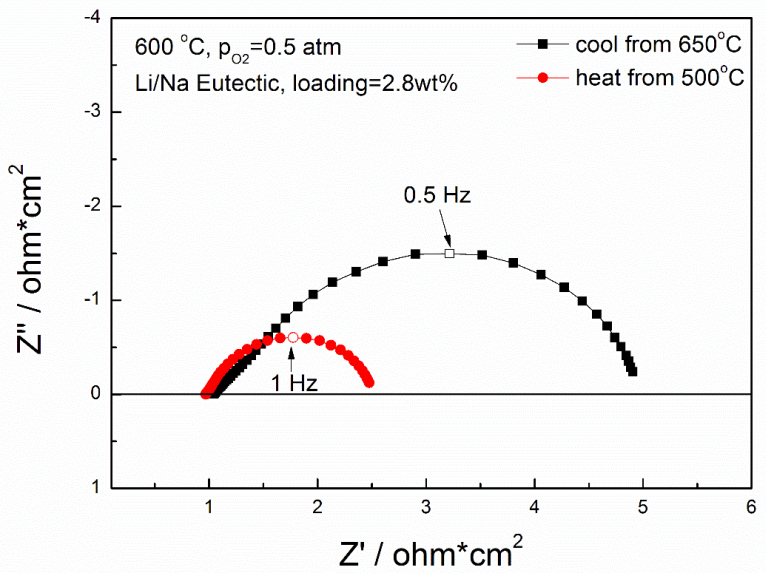

Figure 4.7. EIS spectra of the MC infiltrated cathode measured at 600°C via cool-down route and heat-up route.

4.4.2 Polarization resistance of different cathode materials infiltrated by MC

MC-infiltrated Au cathode. It is well known that Au has no intrinsic catalytic activity for ORR at elevated temperatures. However, after infiltration of MC, Figure 4.8 shows that the MC/gold composite cathode becomes ORR active. The shapes of the spectra also suggests different the electrode processes are drastically different between the two samples.

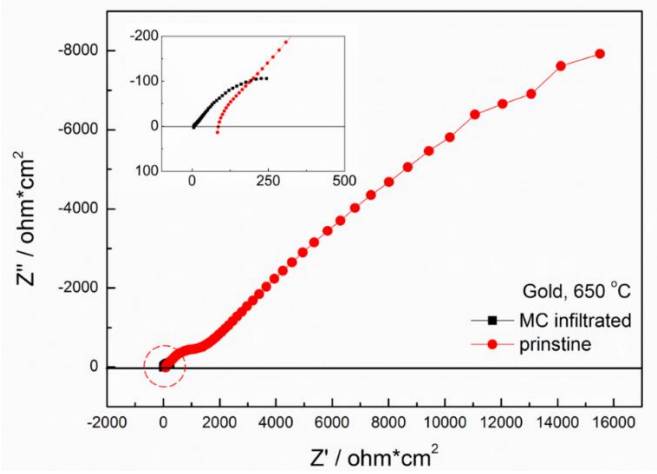

Figure 4.8. EIS spectra of pristine and MC-infiltrated gold cathodes at 650°C

MC-infiltrated Ag cathode. It is well known in the literature that silver has a limited catalytic ORR activity at elevated temperatures. Therefore, it is not surprising to see low R_P for pristine Ag cathode. After infiltration of MC, Figure 4.9 shows that the ORR activity can be further enhanced.

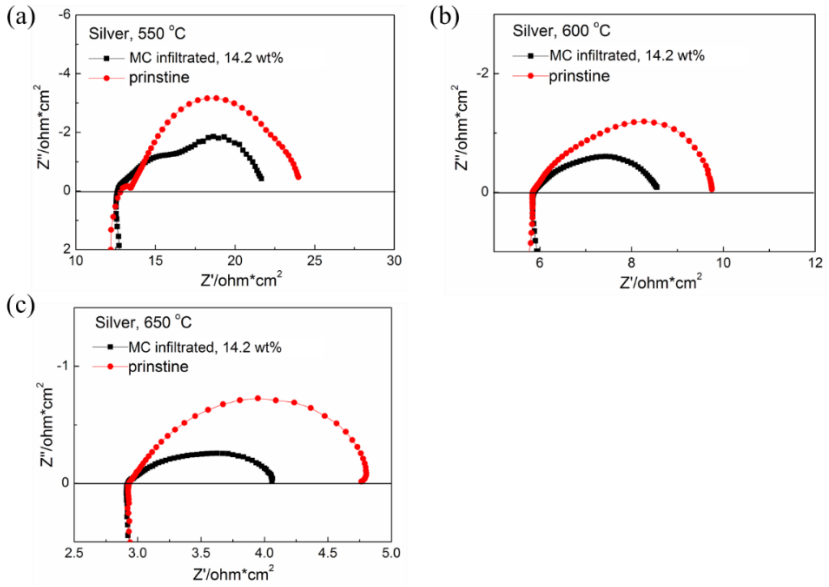

Figure 4.9. EIS spectra result of pristine and MC-infiltrated silver cathodes at (a) 550°C, (b) 600°C, (c) 650°C.

MC-infiltrated LSM cathode. It is knows that the LSM is a poor oxide-ion conductor but excellent electronic conductor at 550-650 °C and does not react with LSGM. Therefore, its ORR activity is expected to be low, which has been confirmed by Figure 4.10. After infiltration of MC into LSM, the ORR activity has been appreciably enhanced. In particular, at 650 °C, the low frequency arc became small compared to the baseline, which infers that MC may have improved oxygen adsorption/diffusion processes.

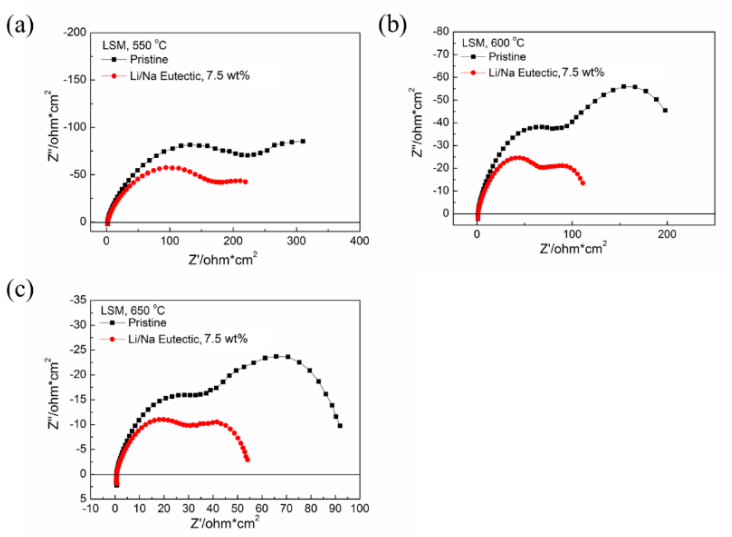

Figure 4.10. EIS spectra result of pristine and MC-infiltrated LSM at (a) 550°C, (b) 600°C, (c) 650°C.

MC-LSCF cathode. As LSCF is a good intrinsic ORR cathode, it is not surprising to see the overall low R_P in Figure 4.11. However, after infiltration of MC, Figure 4.11 shows that there is a further reduction in R_P. More results on the effect of MC loading will be discussed in the next section.

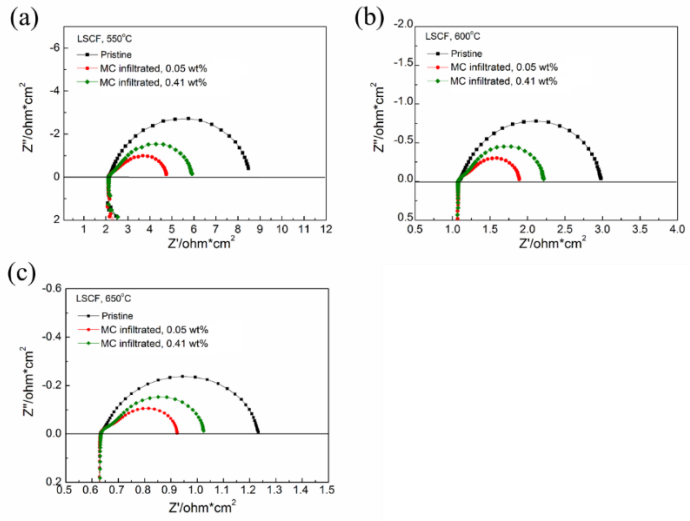

Figure 4.11. EIS spectra of pristine and MC-infiltrated LSCF at (a) 550°C, (b) 600°C, (c) 650°C.

MC-infiltrated La_2NiO_4 cathode. La_2NiO_4 has been reported to exhibit high intrinsic ORR activity due to its mixed conductivity. Therefore, its overall R_P is relatively low as shown in Figure 4.12. After MC infiltration, R_P is further reduced in a similar fashion as LSCF shown in Figure 4.11. A facilitated oxygen adsorption/dissociation/diffusion by MC is hypothesized to be the root cause.

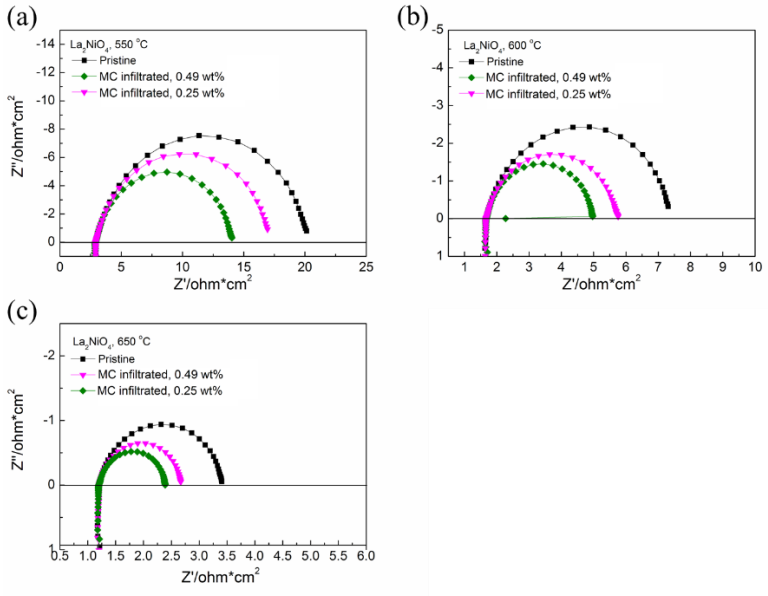

Figure 4.12. EIS spectra result of pristine and MC-infiltrated La_2NiO_4 at (a) 550°C, (b) 600°C, (c) 650°C.

In summary, the beneficial effect on reduction of R_p by infiltration of MC has been observed for all the cathode studied. In the following, we use computational analysis to understand the fundamental reason for the enhancement.

4.4.3 Carbonate loading effect on polarization of resistance

The mass loading effect of MC on R_P of the cathode was preliminarily discussed in the previous section. In all EIS spectra, the total R_P of the pristine cathode is dominated by the high R_P defined as the length on the real-axis between the highest- and lowest-frequency

intercepts. Carbonate effect on reduction in R_p from its original value is significant. A quantified comparison as a function of MC loadings from MC infiltrated LSCF cathode at four temperatures of 500, 550, 600 and 650°C is illustrated in Figure 4.13. The height of bar represents the percentage of R_P in relative to those of the pristine sample. It shows the higher loading leads to a greater reduction in R_p and the reduction percentage is the same from 500 to 600°C, being less temperature-sensitive. While the loading increases to 1.4 wt%, the effect of R_p reduction tends to reach a limit. The lowest R_P obtained at 2.8 wt% represents less than 2% that of the pristine sample within 500-650°C.

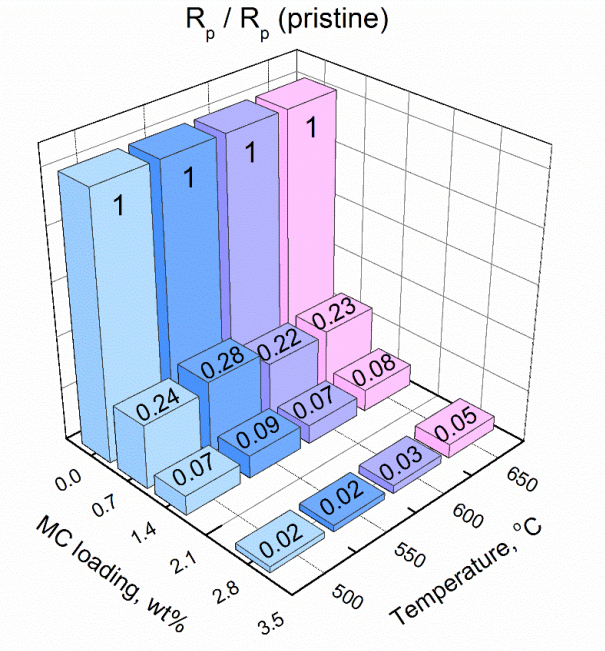

Figure 4.13. The degree of R_P reduction vs the loading of MC into LSCF cathode at 500, 550, 600 and 650°C.

On the other hand, for a given MC loading from 0.7 to 1.4 wt%, Figure 4.14 shows that R_p decreases with increasing temperature, which is a typical thermally-activated polarization process. The degree of reduction between 500 and 550°C is larger than that at higher temperatures, due to its closeness to the melting point of the Li/Na eutectic. However, for

MC loading of 2.8 wt%, R_p increases with temperature from 550 to 650°C, which indicates the high loading and high mobility facilitates aggregation and even loss of MC. Therefore, limited by the infiltration process, the optimal loading is around 1.4 wt%.

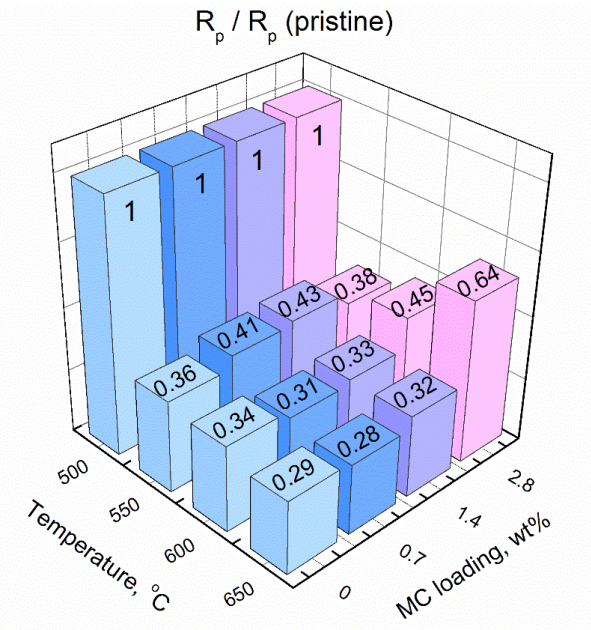

Figure 4.14. The degree of R_P reduction vs temperature at different loading of MC.

The activation energy (E_a) obtained from the Arrhenius plot of $1/R_p$ vs1000/T is shown in Figure 4.15. The E_a of pristine LSCF is 1.53 eV in the temperature range of 500-650°C, consistent with other reported values [262]. After MC infiltration, E_a is reduced to 1.18-1.38 eV. E_a at higher loading is smaller than that at lower loading. According to the Arrhenius equation, the pre-exponential factor A represents the total number of collisions per second, while $e^{\frac{-E_a}{RT}}$ is the probability of a collision happens in the reaction. The lower E_a of MC-infiltrated LSCF suggests MC increases the probability of collision leading to a faster ORR.

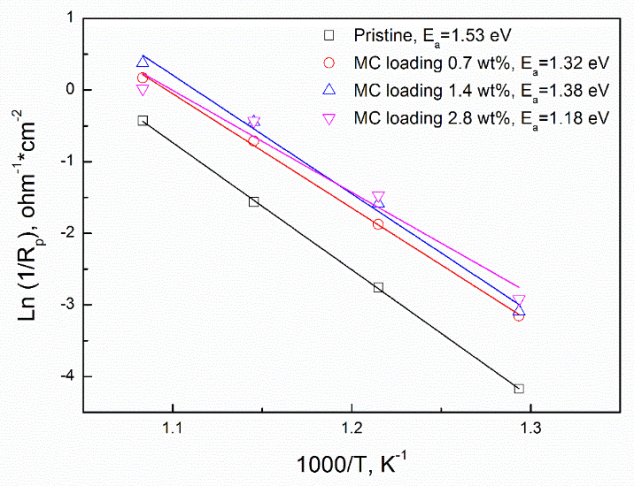

Figure 4.15. Arrhenius plot of R_p as a function of reciprocal temperature for the different MC-loadings into LSCF cathode.

4.4.4 The effect of partial pressure of oxygen on polarization resistance

The dependence of R_P of MC-added LSCF cathode on temperature (T) and partial pressure of oxygen (Po2) was investigated with EIS method to reveal more insights into rate-determining steps of the ORR mechanisms. The symmetrical cells consist of MC-LSCF/LSGM/MC-LSCF and Po_2 and T were varied in a range of 0.05-0.5 atm (some samples in 0.1-1 atm) and 500-650^{o}C, respectively. Figure 4.16 displays the spectra measured at 550^{o}C and different Po_2 without MC loading and with a loading of 1.4 wt%. Generally, an ORR process may consist of several elementary steps, which have different dependence on Po_2, reflected in m of $R = Kp(O_2)^{-m}$. According to the model proposed by Heuveln and Bouwmeester[263], an ORR process includes:

(1) Dissociative adsorption: $O_{2(g)} \leftrightarrow 2O_{ad}$ m=1

(2) Charge transfer: $O_{ad} + e' \leftrightarrow O_{ad}^-$ m=0.375

(3) Surface diffusion: $O_{ad}^- \leftrightarrow O_{TPB}^-$ m=0.25

(4) Charge transfer at TPB: $O_{TPB}^- + e' \leftrightarrow O_{TPB}^{2-}$ m=0.125

(5) Oxygen ion incorporation from TPBs to the electrolyte:

$$O_{TPB}^{2-} + V_{O,electrolyte}^{\cdot\cdot} \leftrightarrow O_{O,electrolyte}^{\times} \qquad \text{m=0}$$

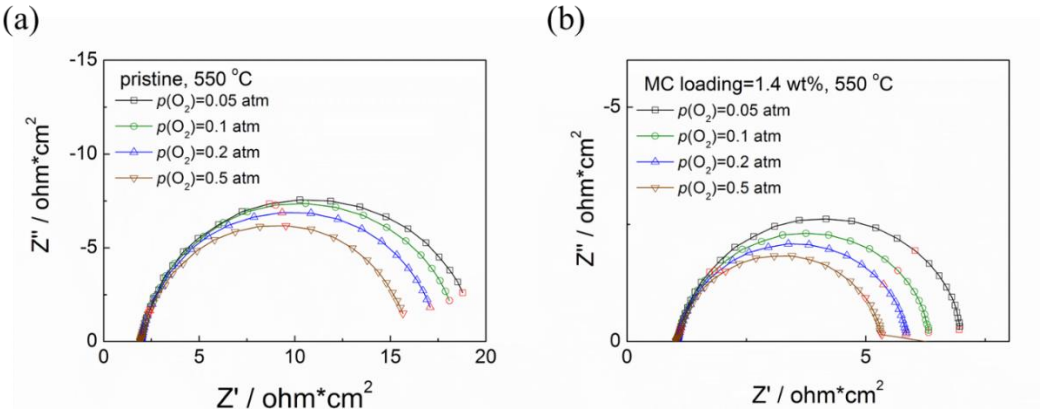

Figure 4.16. Impedance spectra of symmetrical cell LSCF/LSGM/LSCF at 550°C with (a) 0 of MC loading and (b) 1.4 wt% of MC loading. The characteristic frequencies (red symbols) from high to low are 10^3, 10^2, 10, 1, 10^{-1}, 10^{-2} Hz.

As shown in Figure 4.17, the m values for the processes of pristine and MC infiltrated samples are similar. They are either close or below 0.125. For the pristine sample, m value becomes smaller with higher temperatures, which indicates the charge transfer at TPB is the rate limiting step for LSCF from 500 to 650°C. For the MC infiltrated LSCF, m values slightly increase but very close to 0.125, thus the rate limiting step is still the charge transfer at TPB. Besides, the increased m values may possibly result from LSCF particle embedded in large MC phase. The m values at 2.8 wt% loading also supports the assumption, which it is very close to 0.25 at 650°C. Although, at a proper loading with the infiltration process used, such as 1.4 wt%, the composite cathode can have a better oxygen reduction catalytic activity from 500 to 650°C.

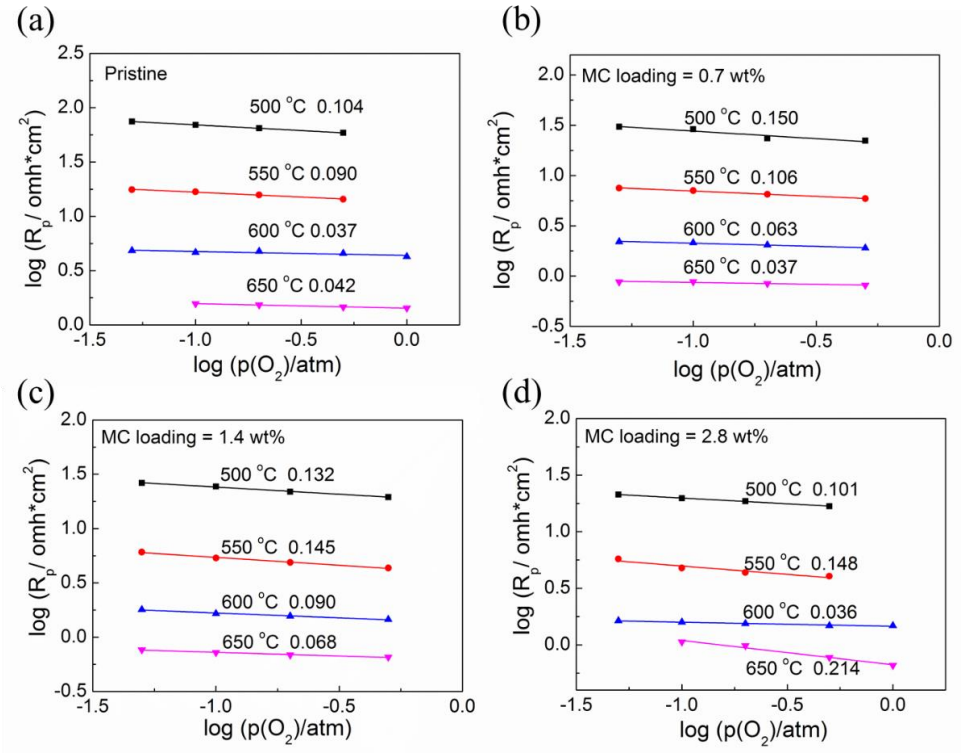

Figure 4.17. The Po_2 dependence of R_p with different MC loadings: (a) pristine, (b) 0.7 wt%, (c) 1.4 wt%, (d) 2.8 wt%. The corresponding m values in $R = Kp(O_2)^{-m}$ at different temperatures are inset.

4.4.5 DFT modeling of oxygen dissociation in molten carbonate

The experimental results clearly indicated that the MC phase is responsible for the enhanced ORR activity. We hypothesis that it is related to the enhanced adsorption/dissociation and diffusion of oxygen species at the MC-cathode interface. There are four possible reactions hypothesized:

$$CO_3^{2-} + O_2 \rightarrow CO_5^{2-} \quad (4\text{-}1)$$

$$CO_5^{2-} + CO_3^{2-} \rightarrow 2CO_4^{2-} \quad (4\text{-}2)$$

$$2CO_3^{2-} + O_2 \rightarrow 2CO_4^{2-} \quad (4\text{-}3)$$

$$CO_4^{2-} + 2e^- \rightarrow CO_3^{2-} + O^{2-} \quad (4\text{-}4)$$

Reaction (4-1) and (4-2) represent the adsorption and dissociation of oxygen molecule in molten carbonate forming the intermediate species CO_5^{2-} and CO_4^{2-}. These two processes can be combined in reaction (4-3). The reaction (4-4) describes reduction of CO_4^{2-} by electrons to CO_3^{2-} and O^{2-}, thus completing the mass balance cycle of CO_3^{2-}.

In the above model, the intermediate species CO_4^{2-} and CO_5^{2-} are critical to the understanding of the enhanced ORR activity. Therefore, we further study the structure of CO_4^{2-} and CO_5^{2-} by optimizing with the B3LYP/6-31G(d) level, which is shown in Figure 4.18.

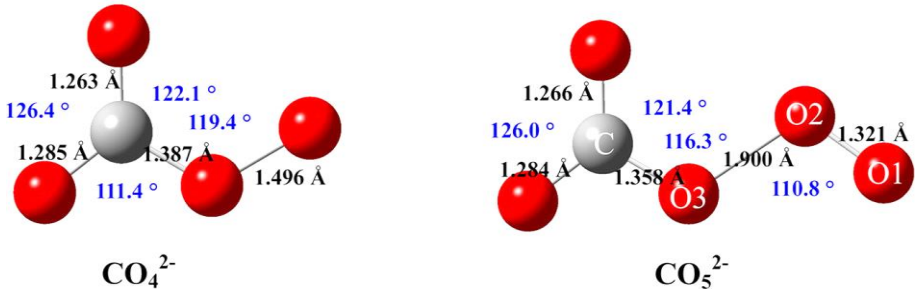

Figure 4.18. Optimized structures of CO_4^{2-} and CO_5^{2-} at the B3LYP/6-31G(d) level

4.4.5.1 Oxygen dissociation in the $(Li_2CO_3)_4$ cluster

The stability of oxygen-containing species CO_4^{2-} and CO_5^{2-} can be evaluated by a $(Li_2CO_3)_4O_2$ cluster. Figure 4.19 shows a process of oxygen dissociation in a $(Li_2CO_3)_4O_2$ cluster. The initial state is the structure with minimum energy optimized. The added oxygen molecule bonds with one carbonate to form CO_5^{2-}, which simulates oxygen adsorbing on a molten carbonate ion. The bond distance of O26 and O10 is 0.426 Å, shorter than that of single CO_5^{2-}. The APT charge of O25 and O26 is calculated to be 0.09e and -0.69e. The negative charge is about 75% from O10 and 25% from the surrounding Li atoms. The electrons are pulled toward O26 by Coulomb force since O26 connects to three Li atoms.

The electron density is injected into the antibonding orbital of O25-O26, resulting in an increase of distance. Thus, oxygen molecule and carbonate ion interaction is of covalent bonding and the bonding of oxygen atoms is weakened by the carbonate ion.

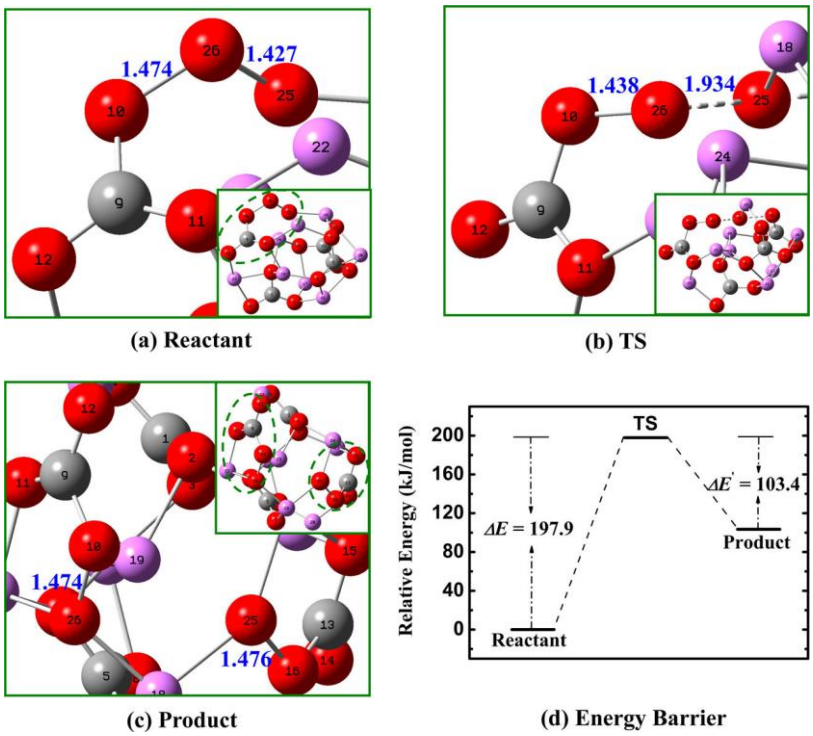

Figure 4.19. Structure of initial, transitional, and final states in $(Li_2CO_3)_4O_2$. Gray, red and purple balls represent C, O and Li.

A new O25-O16 bond forms when O25 departs from O26 to another carbonate oxygen atom O16. This process has a transition state (TS), at which the distance between O25 and O26 increases to 1.934 Å, while the distance between O26 and O10 decreases by 0.036 Å. The system has an energy barrier of 197.9 kJ/mol. In the end, the O25-O26 bond is broken with a distance of 3 Å, while O25-O16 bond forms.

4.4.5.2 Oxygen dissociation in the $(Na_2CO_3)_4$ cluster

Figure 4.20 shows a process of oxygen dissociation in a $(Na_2CO_3)_4$ cluster. The added oxygen molecule bonds with one carbonate to form O26-O4 bond as a CO_5^{2-}. The bond distance of O26-O25 and O26-O4 is 1.391 Å and 1.578 Å, respectively. The APT charge

of O25 and O26 is 0.20e and -0.60e, respectively. As the same dissociation process as in $(Li_2CO_3)_4$ cluster, the O25-O6 bond forms when O25 departs from O26 to another carbonate oxygen atom O6. At the TS, the distance between O25 and O26 increases to 1.986 Å, while the distance of O26-O4 bond decreases by 0.114 Å. The system has an energy barrier of 116.7 kJ/mol. In the end, two CO_4^{2-} form to complete the oxygen dissociation process.

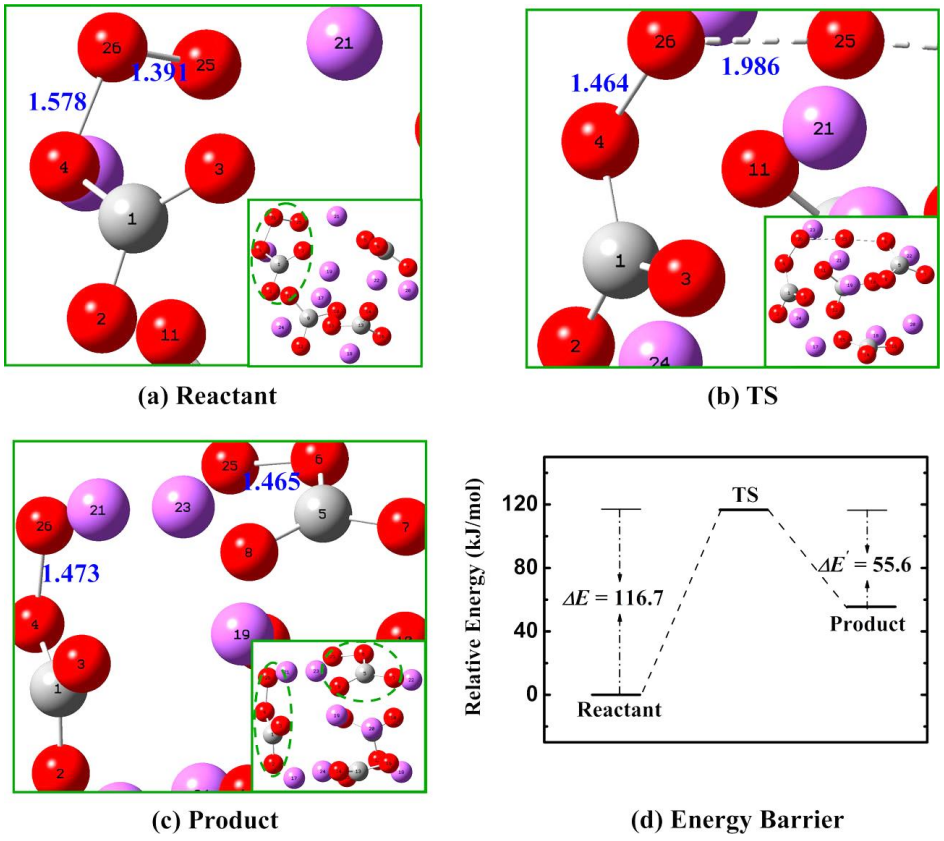

Figure 4.20. Structure of initial, transitional, and final states in $(Na_2CO_3)_4O_2$. Gray, red and purple balls represent C, O and Na.

4.4.5.3 Oxygen dissociation in the $(K_2CO_3)_4$ cluster

Figure 4.21 shows the process of oxygen dissociation in a $(K_2CO_3)_4$ cluster. Similarly, the O25-O26 bond is attached to O8 as a CO_5^{2-}. The bond distance of O26-O25 and O25-O8 is 1.408 Å and 1.450 Å, respectively. The APT charge of O25 and O26 is 0.11e and -

0.69e, respectively. As the same process, O26 leaves O25 toward O3 with O25-O26 bond breaking, while O26 and O3 begin to bind together. At TS, the distance between O25 and O26 increases to 2.000 Å, while the distance of O25-O8 bond decreases by 0.001 Å. The system has an energy barrier of 170.3 kJ/mol. In the end, O26 and O3 bond together with a distance of 1.466 Å, and O26 is 3.470 Å away from O25.

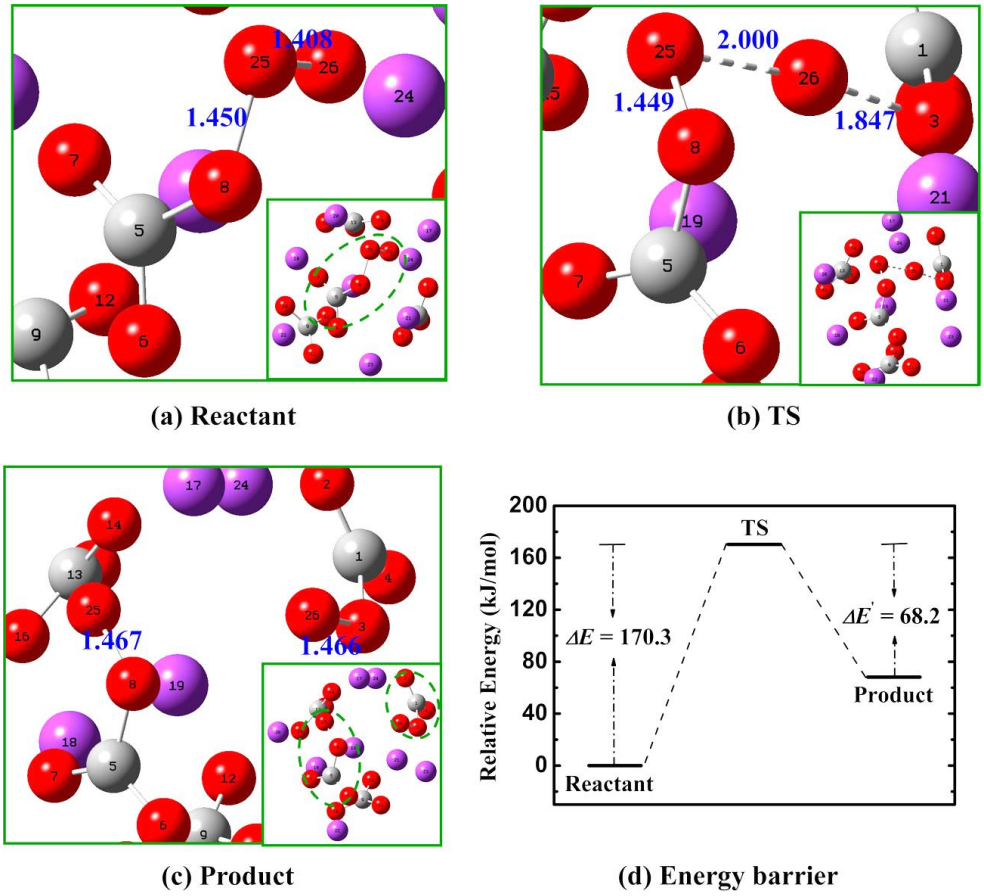

Figure 4.21. Structure of initial, transitional, and final states in $(Na_2CO_3)_4O_2$. Gray, red and purple balls represent C, O and K.

4.4.5.4 Total oxygen dissociation reaction in MC

The formation of CO_5^{2-} in molten carbonate suggests a chemisorption of gaseous oxygen on the surface of MC. The binding energy was estimated as 101.7 kJ/mol.[264] After the formation of CO_5^{2-}, it reacts another CO_3^{2-} to form two CO_4^{2-}, which is the rate-limiting

on potential energy surface as shown in Figure 4.22. The energy barriers were calculated to be 197.7, 116.7 and 170.3 kJ/mol for Li, Na and K, in previous section.

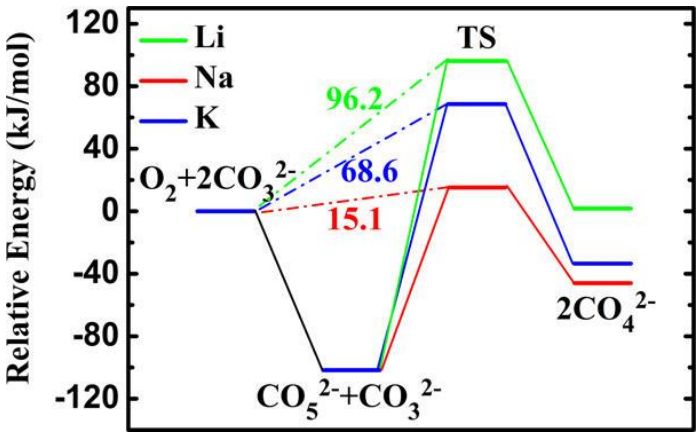

Figure 4.22. Potential energy surface of oxygen dissociation in the $(M_2CO_3)_4$ (M=Li, Na, K) cluster.

The energy change from CO_5^{2-} with CO_3^{2-} to CO_4^{2-} is 103.3, 55.6 and 68.2 kJ/mol, respectively, which agrees with the result of 86.2 kJ/mol for the reaction in gas phase at the B3LYP/6-31G(d) level. If the reaction is expressed below, CO_5^{2-} is deemed an intermediate:

$$2CO_3{}^{2-} + O_2 \underset{k_{-1}}{\overset{k_1}{\rightleftarrows}} CO_5{}^{2-} + CO_3{}^{2-} \overset{k_2}{\rightarrow} 2CO_4{}^{2-} \tag{4-5}$$

$$\text{Reaction Rate} = \frac{k_1}{k_{-1}+k_2}\,[O_2]\left[CO_3{}^{2-}\right]^2 \tag{4-6}$$

In terms of steady-state theory, the reaction rate can be described by reaction (4-6). Hence, in this reaction, the effective activation energy is 96.2, 15.1 and 68.6 kJ/mol in Li, Na and K molten carbonates, respectively. The pseudo one-step reaction is exothermic and favored by chemical thermodynamics for Na and K, but slightly endothermic for Li. In addition, the reaction rate is affected by the pressure of oxygen. Increasing oxygen pressure will promote the reaction.

4.4.6 DFT modeling of oxygen transfer in molten carbonate

Although the dissociation of oxygen in molten carbonate is proved to be energetically favorable, energy profile of oxygen atoms migration from surface to MC/cathode interface needs to be identified. This study is started with the modeling of oxygen atom transfer in a carbonate ion.

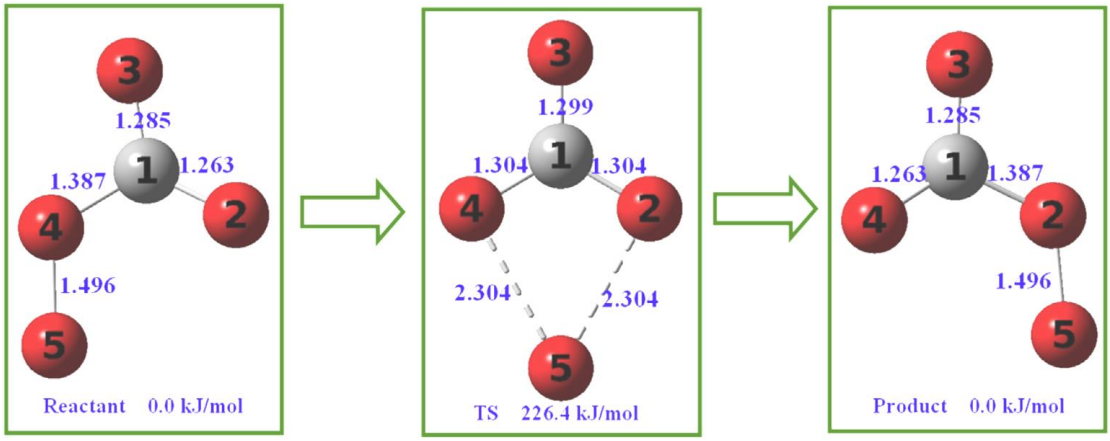

Figure 4.23. The structures of reactant, transition state and product with the relative energy.

4.4.6.1 Intramolecular migration of oxygen in carbonate ion

Figure 4.23 indicates the structure of initial, transitional, and final phase of intramolecular transfer oxygen in a carbonate ion. The reactant and product are identical CO_4^{2-} with a Cs symmetry. O5 is bonded to O4 and O2, respectively. The bonding of O5 with O4 weakens C1-O4 bond with a distance of 1.387 Å, compared to the optimized C-O bond distance of 1.313 Å. However, C1-O2 and C1-O3 are shortened to 1.263 Å and 1.285 Å. The Mulliken charge on O4-O5 is calculated to be -1.13e with bond distance of 1.496 Å, suggesting that O4-O5 is a fragment between superoxide and peroxide. At the TS, O5-O4 stretches to 2.304 Å as well as O5-O2, where O5 almost detaches from the carbonate ion. Besides, the C-O bond length becomes close to 1.313 Å in CO_3^{2-}. From the molecular

orbitals related to the interaction between O5 and carbonate ion, small overlaps between 2p of O5 and 2p lone pairs of O4 and O2 can be seen in Figure 4.24. Due to the long distance, the electron density between O5 and O4, O2 is not largely increased, which also indicates that O5 almost detaches from the carbonate ion at TS. The calculated energy barrier is 226.4 kJ/mol.

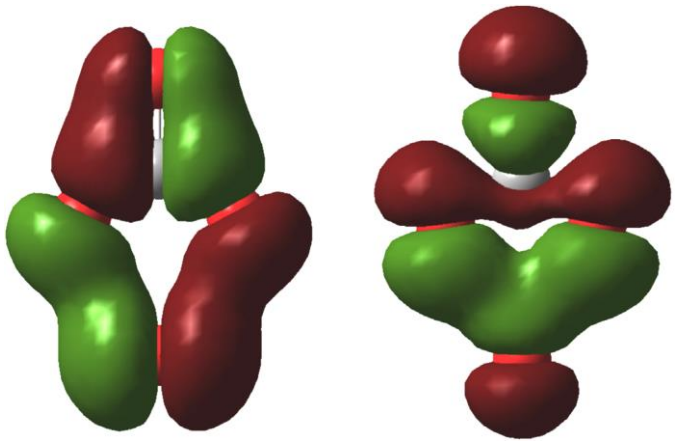

Figure 4.24. Selected molecular orbitals related to the bonding of O5-O4 and O5-O2 at TS.

4.4.6.2 Intermolecular migration of oxygen in Li_2CO_3

There are three stationary points in potential energy surface of migration process in Figure 4.25. The local structure of $[Li_2O(CO_3^{2-})_2]^{2-}$, where oxygen transfer occurs, is enlarged at the top and the whole cluster is shown at bottom. At the initial state, O1-O4 bond distance is 1.465 Å. The whole CO_4^{2-} twists with an O4-O1-C1-O3 dihedral of 20°. The bond length are close to that in gas phase. The charge of O1-O4 is -0.77 e, which is 0.36 e less than the value in a single CO_4^{2-} ion. The total charge of CO_4^{2-} and CO_3^{2-} are calculated to be -1.030 and -1.011 e, respectively, which are very close to the charge of CO_3^{2-} (0.976 e) in the $(Li_2CO_3)_4$ cluster.

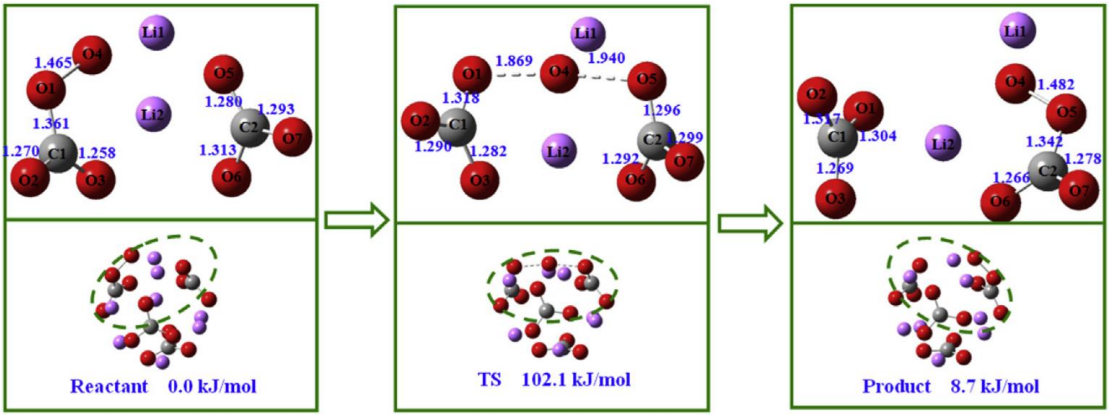

Figure 4.25. The structures of initial, transitional and final state with the relative energy for oxygen migration in $(Li_2CO_3)_4$

The stretching of O1-O4 initiates the oxygen transfer. At TS in Figure 4.25, the O1-O4 bond is stretched to 1.869 Å, while O4-O5 is shorted to 1.940 Å. After O4 leaves, the resonance in the carbonate (C1 center) is almost restored, indicated by the C-O bonds. The IRC modeling proves the connectivity from the reactant to product via TS on potential energy surface.

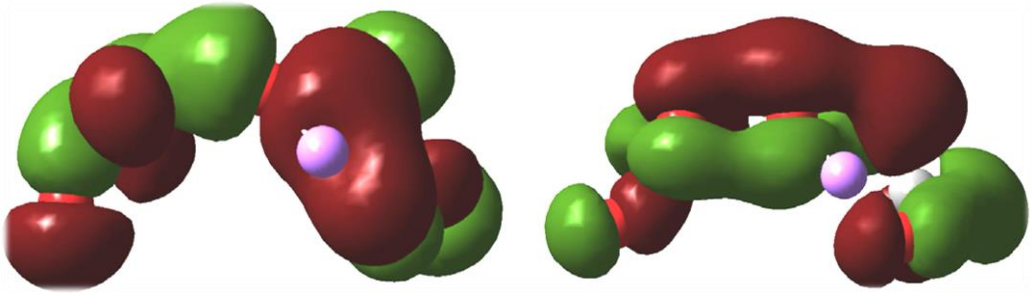

Figure 4.26. Selected molecular orbitals related to the bonding of O1-O4-O5 at transition state.

Molecule orbital analysis is shown in Figure 4.26. The bond forming and breaking process is concerted through the formation of O1-O4-O5. Two major bonding modes are in O1-O4-O5 linkage, sigma bond between the 2p orbital of oxygen along the O1-O4-O5 axis and pi bond by oxygen 2p. The bond distance of O1-O4 and O4-O5 indicate a stable

transition structure and this linkage largely lowers the energy barrier for oxygen migration between two carbonate ions. The calculated energy barrier is 102.1 kJ/mol, which is far lower than that of the intramolecular path.

4.4.6.3 Intermolecular migration of oxygen in Na_2CO_3

The migration process is similar in sodium carbonate cluster, as shown in Figure 4.27. The oxygen O4 transfer from one carbonate (C1) to another carbonate ion (C2). The O1-O4 increases from 1.480 Å to 2.098 Å and O4-O5 bond forms at the length of 1.859 Å at TS. O1-O4-O5 linkage also forms in sodium carbonate cluster. This TS structure connects the reactant and product on potential energy surface identified by the IRC calculations. The activation energy is 131.4 kJ/mol, a slightly higher than that of lithium carbonate, but still lower than that of the intramolecular transfer.

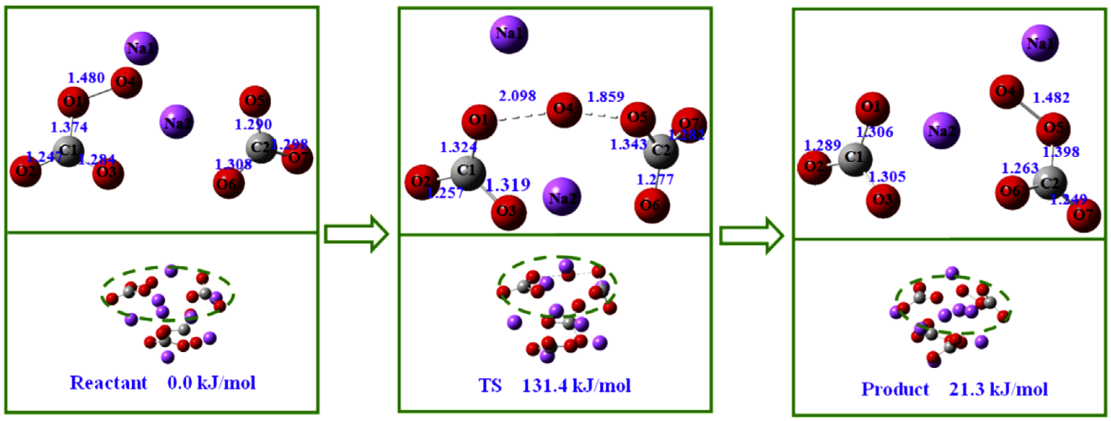

Figure 4.27. The structures of initial, transitional and final state with the relative energy for oxygen migration in $(Na_2CO_3)_4$.

4.4.6.4 Intermolecular migration of oxygen in K_2CO_3

The migration process including the structure of reactant, transition state and product is shown in Figure 4.28. The process is the same as other carbonates. The oxygen O4 transfer from one carbonate (C1) to another carbonate ion (C2). The O1-O4 increases from

1.465 Å to 1.946 Å and O4-O5 bond forms at the length of 1.958 Å at TS. O1-O4-O5 linkage also forms in potassium carbonate cluster. This TS structure connects the reactant and product on potential energy surface identified by the IRC calculations. The activation energy is 128.1 kJ/mol, very close to the value in lithium carbonate and sodium carbonate.

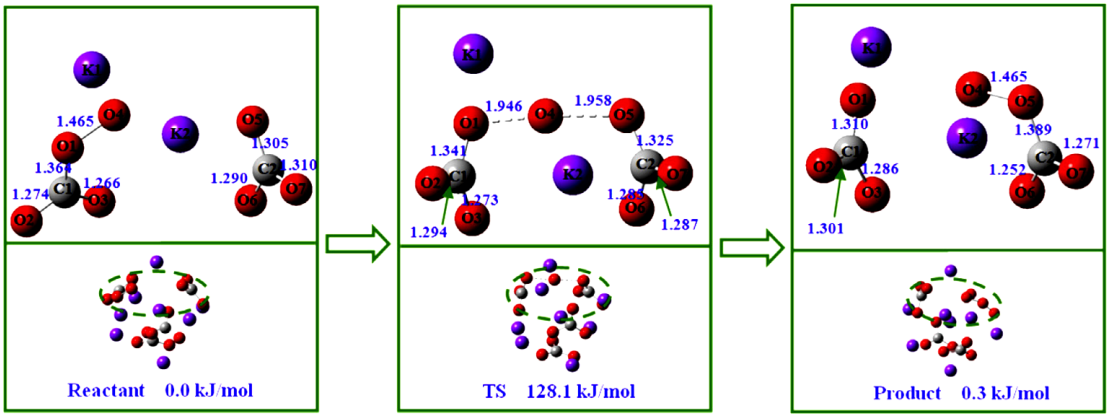

Figure 4.28. The structures of initial, transitional and final state with the relative energy for oxygen migration in $(K_2CO_3)_4$.

4.4.6.5 Summary of oxygen migration in molten carbonate

Oxygen migration in molten carbonate is energetically favorable by intermolecular pathways. For intermolecular migration, the energy barriers are calculated to be 103.0, 136.3 and 127.9 kJ/mol for lithium, sodium and potasium carbonates, respectively. In CO_4^{2-} of the molten carbonate salt as shown in Figure 4.25, 4.27, and 4.28, the O1- O4 distance is 1.465 to 1.480 Å, while the total Mulliken charge is -0.77e to 0.85e, respectively. The change of geometry, charge and frequency from Li, Na to K salt is negligible. In terms of bond distance and stretching, O1-O4 is similar to peroxide with both π_{2p} bonding and π_{2p}^* antibonding orbitals occupied. Once O1-O4 is elongated, the $\sigma_{2p\text{-}2p}$ bond is broken, which will release the 2p orbital of O4 being ready for bonding with O5. A linkage of O1-O4-O5 is then formed, which is also strengthened by a π_{2p} orbital. The formation of such oxygen atoms linkage facilitates the oxygen migration between the carbonate ions.

4.5 Conclusion

MC infiltrated cathodes have been evaluated microstructurally and electrically to understand the enhanced ORR activity. It was shown that the MC phase can be successfully introduced into the porous cathodes by carbonate salt precursor and oxalate salt precursor, although the infiltrated Li/Na carbonate eutectic phase could not form nanosized particles in the cathode. This eutectic has a melting point around 500^{o}C. Above 500^{o}C, the decreasing viscosity of MC makes more mobile. Once the loading reaches to 2.8 wt%, MC phase tends to aggregate at 600 to 650^{o}C, which may weaken the effect on enhancing ORR activity. The following EIS study show that adding MC can reduce R_p of different cathodes, including Au, LSM, LSCF and LNO. Specifically, more studies on MC loading effect were carried out on the LSCF cathode. It shows the higher loading makes a greater reduction on R_p and the degree of reduction is the same for 500 to 600^{o}C. As the loading increase to 1.4 wt%, the degree of R_p reduction tends to reach a limit. The lowest R_P obtained at 2.8 wt% is less than 2% that of the pristine sample within 500-650^{o}C. At a fixed MC loading from 0.7 to 1.4 wt%, R_p decreases with temperature. However, at 2.8 wt%, R_p increases with temperature from 550 to 650^{o}C, which suggests that aggregation and even loss of MC may have occurred. Thus, the optimal loading for MC is around 1.4 wt%. The activation energy (E_a) for MC-LSCF is 1.18-1.38 eV, a significant reduction from xx eV, suggesting that MC phase promotes the ORR. The study of R_p dependence of MC-LSCF cathode on Po_2 suggests that the rate-determining step remains almost the same for both modified and baseline LSCF cathodes.

First-principles DFT modeling further was used to investigate the incorporation of oxygen into MC. The formation of CO_5^{2-} in molten carbonate was considered to represent

a chemisorption of gas oxygen on the surface of MC infiltrated cathode. After the formation of CO_5^{2-}, it reacts with another CO_3^{2-} to form two CO_4^{2-}, which is a rate-limiting step on potential energy surface. If the total reaction begins from the incorporation of oxygen to CO_3^{2-}, CO_5^{2-} becomes an intermediate. With the steady-state theory, the calculated effective activation energy is 96.2, 15.1 and 68.6 kJ/mol for Li, Na and K molten carbonates, respectively. The pseudo one-step reaction is exothermic and favored by chemical thermodynamics for Na and K, but slightly endothermic for Li. After dissociation, Oxygen atoms migrate in molten carbonate, which is energetically favored by intermolecular pathways. The calculated energy barriers are 103.0, 136.3 and 127.9 kJ/mol in lithium, sodium and potassium carbonates, respectively. For CO_4^{2-} in the molten carbonate salt, the O1- O4 distance is 1.465 to 1.480 Å, while the total Mulliken charge is -0.77e to 0.85e. The change of geometry, charge and frequency from Li, Na to K salt is negligible. For the bond distance and stretching, O1-O4 is similar to peroxide with both π_{2p} bonding and π_{2p}^* antibonding orbitals occupied. Once O1-O4 is elongated, the $\sigma_{2p\text{-}2p}$ bond is broken, which will release the 2p orbital of O4 being ready for bonding with O5. A linkage of O1-O4-O5 is then formed, which is also strengthened by a π_{2p} orbital. The formation of such oxygen atoms linkage facilitates the oxygen migration between each carbonate ions.

CHAPTER 5

SUMMARY

Energy supply structure adjustment and clean energy conversion technology promotion are needed to deal with the energy supply stress and environmental problem. Fuel cell is a cleaner, more efficient, and possibly the most flexible chemical-to-electrical energy conversion device to help mitigate the growing environmental issues and the utilization and deployment of renewable energy. Solid oxide fuel cells (SOFCs) as a high-temperature fuel cell have the advantage of fuel flexibility (capable of using existing hydrocarbon fuel) and high efficiency. The recent research is aimed to lower the operating temperature to an intermediate temperature (IT) range of 500 to 700^{o}C, while maintaining a proper performance. This Ph.D. research project investigates the promotional effects of alkaline carbonate eutectics on the proton conductivity of proton conducting electrolytes and cathodic ORR reactivity in SOFCs by both experimental and computational methods.

$BaZr_{0.8}Y_{0.2}O_{3-\delta}$ (BZY) has good ionic conductivity and chemically stability, but it is hard to sinter into a dense body. Li/Na carbonate eutectic (denoted as molten carbonate, MC) was used as a sintering aid to enable BZY sintering at lower temperatures, while introducing CO_3^{2-} into the ionic conduction, making it a mixed H^+ and CO_3^{2-} conductor. The MC-BZY composite electrolyte has been evaluated experimentally and

computationally to understand the enhanced conductivity and improved SOFC performance. It was shown that the composite can be made into a dense membrane at 650^{o}C by filling the pores in BZY with MC phase. The ionic conductivity of the composite above 500 ^{o}C increases with the loading and type of MC. More importantly, the sample exhibited nearly a factor of two higher conductivity in H_2-containing atmosphere than in air. The dependences of conductivity on partial pressures of H_2 and H_2O, as well as the type of H (H *vs* D), suggested that proton conduction takes place, primarily via the MC phase. A defect chemistry model was proposed to explain the synergetic proton transfer between BZY and MC phases.

First-principles DFT modeling further investigated proton transfer in a carbonate ion, lithium carbonate crystal and lithium carbonate cluster. The results show that proton rotation around an oxygen of carbonate ion is more energetically favorable than transfer between oxygen atoms, revealing the feasible path of proton migration relying on the orientation of carbonate ions. The migration pathways in lithium carbonate crystal were also modeled. The calculated energy profiles show that the $[001]$ and $[00\bar{1}]$ directions (along *c*-axis) are the lowest energy barrier pathways, which is originated from the crystallographic orientation of carbonate ion perpendicular to *c*-axis, further facilitating proton rotation. The $(Li_2CO_3)_8$ cluster model was used to simulate the disordered molten carbonates. The calculated energy profile shows an extremely low proton migration energy barrier.

The proton migration at the interface of $BaZrO_3$ and molten carbonate were also studied. At ZrO_2-terminated (100) surface of $BaZrO_3$, proton moves via a curved path with an energy barrier of 0.567 eV and the effect of dopant Y on the energy barrier for proton

migration is very small, only lowering the energy barrier by 0.034 eV. With the presence of carbonate ion, the energy barrier for proton migration becomes as low as 0.332 eV, which agrees well with the activation energy of 0.33 eV obtained by the experiment. The modeling indicates the reduction of energy barrier is resulted from the change of rate-determining step from proton transfer between oxygen atoms to proton rotation around oxygen atom.

At lower temperatures, increasing polarization losses from cathode is a major challenge. Infiltration of MC into porous cathode can reduce the polarization of resistance (R_p), i.e., enhance the oxygen reduction reaction (ORR) activity. A number of MC infiltrated cathode composites were evaluated microstructurally and electrically. Alkaline carbonates have very good solubility in water and it is insoluble in other commonly used liquids, such as acetone, ammonia and alcohol. The high solubility makes carbonate precipitating out in large particles. The eutectic has a melting point around 500^{o}C. Beyond 500^{o}C, the reduced viscosity of MC makes it more mobile. As the loading reaches to 2.8 wt%, MC phase tends to aggregate at 600 to 650^{o}C, which may weaken the beneficial effect on ORR activity. The EIS analysis shows that MC indeed has a beneficial effect on reducing R_p for different cathodes including Au, LSM, LSCF and LNO. Specifically, the study on MC loading effect was carried out on LSCF cathode. It shows that a higher loading makes a greater reduction on R_p and the degree of reduction is the same for 500 to 600^{o}C. As the loading increases to 1.4 wt%, the degree of R_p reduction tends to reach a limit. The lowest R_P obtained at 2.8 wt% is less than 2% that of the pristine sample within 500-650^{o}C. At a fixed MC loading ranging from 0.7 to 1.4 wt%, R_p decreases with temperature. However, at 2.8 wt%, R_p increases with temperature from 550 to 650^{o}C, which infers

aggregation and even loss of MC. Thus, the optimal loading is around 1.4 wt%. The activation energy (E_a) of MC-LSCF cathode has a lower 1.18-1.38 eV, suggesting that MC phase promotional effect on the ORR was resulted from the introduction of active species. The study of Po_2-dependent R_p of MC infiltrated LSCF cathodes shows the rate-determining step remains almost the same as the pure LSCF cathode.

First-principles DFT modeling was further used to investigate the incorporation of oxygen into the molten carbonate. The formation of CO_5^{2-} in molten carbonate was considered as a chemisorption of gas oxygen on the surface of MC infiltrated cathodes. After the formation of CO_5^{2-}, it reacts with another CO_3^{2-} to form two CO_4^{2-}, which is a rate-limiting step on potential energy surface. If the total reaction begins from the incorporation of oxygen to CO_3^{2-}, CO_5^{2-} becomes an intermediate. With the steady-state theory, the calculated effective activation energy is 96.2, 15.1 and 68.6 kJ/mol in Li, Na and K molten carbonates, respectively. The pseudo one-step reaction is exothermic and favored by chemical thermodynamics for Na and K carbonates, but slightly endothermic for Li carbonate. After dissociation, oxygen atoms migrate in molten carbonate, which is energetically favor by intermolecular pathways. The calculated energy barriers are 103.0, 136.3 and 127.9 kJ/mol for lithium, sodium and potassium carbonates, respectively. For CO_4^{2-} in the molten carbonate salt, the O1- O4 distance is 1.465 to 1.480 Å, while the total Mulliken charge is -0.77e to 0.85e. The change of geometry, charge and frequency from Li, Na to K salts is negligible. In terms of bond distance and stretching, O1-O4 is similar to peroxide with both π_{2p} bonding and π_{2p}^* antibonding orbitals occupied. Once O1-O4 is elongated, the $\sigma_{2p\text{-}2p}$ bond is broken, which will release the 2p orbital of O4 being ready for bonding with O5. A linkage of O1-O4-O5 is then formed, which is also strengthened by a

π_{2p} orbital. The formation of such oxygen atoms linkage facilitates the oxygen migration between each carbonate ions.

In conclusion, this project demonstrates MC is an effective “catalyst” to enhance proton conductivity of a proton conductor, such as BZY, by providing a new energetically favorable migration pathway for proton transfer at the interface of molten carbonate and ceramic phase. On the other hand, promotion of ORR activity of standard cathodes by MC is confirmed by both experimental data and computational modeling. The participation in oxygen dissociative adsorption by molten carbonate and facilitated oxygen transfer between carbonate ions are the major contributing factors promoting ORR activity.

REFERENCES

1. Li, F., Z. Song, and W. Liu, *China's energy consumption under the global economic crisis: Decomposition and sectoral analysis.* Energy Policy, 2014. **64**: p. 193-202.
2. Yuan, C., S. Liu, and N. Xie, *The impact on chinese economic growth and energy consumption of the Global Financial Crisis: An input–output analysis.* Energy, 2010. **35**(4): p. 1805-1812.
3. Chow, E. and J. Elkind, *Hurricane Katrina and US Energy Security.* Survival, 2005. **47**(4): p. 145-160.
4. *Annual Energy Outlook.* U.S. Energy Information Administration, 2016.
5. O'hayre, R., et al., *Fuel cell fundamentals*. 2016: John Wiley & Sons.
6. Thomas F. Stocker, Q.D., Gian-Kasper Plattner, *Technical Summary.* IPCC AR5 WG1 2013, 2013.
7. Hansen, J., et al., *Assessing "Dangerous Climate Change": Required Reduction of Carbon Emissions to Protect Young People, Future Generations and Nature.* PLoS ONE, 2013. **8**(12): p. 1-26.
8. Fuhrer, J. and P.J. Gregory, *Climate Change Impact and Adaptation in Agricultural Systems: Soil Ecosystem Management in Sustainable Agriculture*. Vol. 5. 2014: CABI.
9. Fischer, E.M. and R. Knutti, *Anthropogenic contribution to global occurrence of heavy-precipitation and high-temperature extremes.* Nature Clim. Change, 2015. **5**(6): p. 560-564.
10. Mazdiyasni, O. and A. AghaKouchak, *Substantial increase in concurrent droughts and heatwaves in the United States.* Proceedings of the National Academy of Sciences, 2015. **112**(37): p. 11484-11489.
11. Watson, C.S., et al., *Unabated global mean sea-level rise over the satellite altimeter era.* Nature Clim. Change, 2015. **5**(6): p. 565-568.
12. Hansen, J., et al., *Ice melt, sea level rise and superstorms: evidence from paleoclimate data, climate modeling, and modern observations that 2 ℃ global warming could be dangerous.* Atmos. Chem. Phys., 2016. **16**(6): p. 3761-3812.
13. Fingar, T., *National intelligence assessment of the national security implications of global climate change to 2030.* http://www.dni.gov/testimonies/20080625_testimony.pdf, 2008.
14. Qureshi, M.I., A.M. Rasli, and K. Zaman, *Energy crisis, greenhouse gas emissions and sectoral growth reforms: repairing the fabricated mosaic.* Journal of Cleaner Production, 2016. **112, Part 5**: p. 3657-3666.
15. Twidell, J. and T. Weir, *Renewable energy resources*. 2015: Routledge.
16. Dincer, I., *Environmental issues: Ii-potential solutions.* Energy sources, 2001. **23**(1): p. 83-92.

17. Steele, B.C.H. and A. Heinzel, *Materials for fuel-cell technologies.* Nature, 2001. **414**(6861): p. 345-352.
18. Briguglio, N., et al., *Evaluation of a low temperature fuel cell system for residential CHP.* International Journal of Hydrogen Energy, 2011. **36**(13): p. 8023-8029.
19. Gigliucci, G., et al., *Demonstration of a residential CHP system based on PEM fuel cells.* Journal of Power Sources, 2004. **131**(1–2): p. 62-68.
20. *The Department of Energy hydrogen and fuel cells program plan: an integrated strategic plan for the research, development, and demonstration of hydrogen and fuel cell technologies.* US Department of Energy, 2011.
21. Varkaraki, E., N. Lymberopoulos, and A. Zachariou, *Hydrogen based emergency back-up system for telecommunication applications.* Journal of Power Sources, 2003. **118**(1–2): p. 14-22.
22. Elgowainy, A., L. Gaines, and M. Wang, *Fuel-cycle analysis of early market applications of fuel cells: Forklift propulsion systems and distributed power generation.* International Journal of Hydrogen Energy, 2009. **34**(9): p. 3557-3570.
23. Renquist, J.V., B. Dickman, and T.H. Bradley, *Economic comparison of fuel cell powered forklifts to battery powered forklifts.* International Journal of Hydrogen Energy, 2012. **37**(17): p. 12054-12059.
24. Cowey, K., et al., *Portable and military fuel cells.* Current Opinion in Solid State and Materials Science, 2004. **8**(5): p. 367-371.
25. Patil, A.S., et al., *Portable fuel cell systems for America's army: technology transition to the field.* Journal of Power Sources, 2004. **136**(2): p. 220-225.
26. Liming, H., *Financing rural renewable energy: A comparison between China and India.* Renewable and Sustainable Energy Reviews, 2009. **13**(5): p. 1096-1103.
27. Michael Wang, A.E., Jeongwoo Han, *Life-Cycle Analysis of Criteria Pollutant Emissions from Stationary Fuel-Cell Systems.* Us Department of Energy Hydrogen and Fuel cells Program, 2010.
28. Bauen, A., D. Hart, and A. Chase, *Fuel cells for distributed generation in developing countries—an analysis.* International Journal of Hydrogen Energy, 2003. **28**(7): p. 695-701.
29. Alcaide, F., P.-L. Cabot, and E. Brillas, *Fuel cells for chemicals and energy cogeneration.* Journal of Power Sources, 2006. **153**(1): p. 47-60.
30. Holmberg, K., P. Andersson, and A. Erdemir, *Global energy consumption due to friction in passenger cars.* Tribology International, 2012. **47**: p. 221-234.
31. Pollet, B.G., I. Staffell, and J.L. Shang, *Current status of hybrid, battery and fuel cell electric vehicles: From electrochemistry to market prospects.* Electrochimica Acta, 2012. **84**: p. 235-249.
32. Institute, B.T., *2011 Fuel Cell technologies market report.* US Department of Energy, 2012. **DOE/EE-0755**.
33. Minh, N.Q., *Ceramic fuel cells.* J. Am. Cer. Soc., 1993. **76**(3): p. 563-588.
34. Dees, D.W., et al., *Conductivity of Porous Ni / ZrO2 - Y 2 O 3 Cermets.* Journal of The Electrochemical Society, 1987. **134**(9): p. 2141-2146.
35. Koide, H., et al., *Properties of Ni/YSZ cermet as anode for SOFC.* Solid State Ionics, 2000. **132**(3–4): p. 253-260.
36. Zhu, W.Z. and S.C. Deevi, *A review on the status of anode materials for solid oxide fuel cells.* Materials Science and Engineering: A, 2003. **362**(1–2): p. 228-239.

37. Brown, M., S. Primdahl, and M. Mogensen, *Structure/Performance Relations for Ni/Yttria-Stabilized Zirconia Anodes for Solid Oxide Fuel Cells.* J. Electrochem.Soc., 2000. **147**(2): p. 475-485.
38. Nakagawa, N., et al., *Evaluation of the Effective Reaction Zone at Ni (NiO) / Zirconia Anode by Using an Electrode with a Novel Structure.* Journal of The Electrochemical Society, 1995. **142**(10): p. 3474-3479.
39. Chan, S.H. and Z.T. Xia, *Anode Micro Model of Solid Oxide Fuel Cell.* Journal of The Electrochemical Society, 2001. **148**(4): p. A388-A394.
40. Iwata, T., *Characterization of Ni-YSZ Anode Degradation for Substrate-Type Solid Oxide Fuel Cells.* Journal of The Electrochemical Society, 1996. **143**(5): p. 1521-1525.
41. Itoh, H., et al., *Configurational and Electrical Behavior of Ni-YSZ Cermet with Novel Microstructure for Solid Oxide Fuel Cell Anodes.* Journal of The Electrochemical Society, 1997. **144**(2): p. 641-646.
42. Aguiar, P., C.S. Adjiman, and N.P. Brandon, *Anode-supported intermediate temperature direct internal reforming solid oxide fuel cell. I: model-based steady-state performance.* J. Power Sources, 2004. **138**(1–2): p. 120-136.
43. Aguiar, P., C.S. Adjiman, and N.P. Brandon, *Anode-supported intermediate-temperature direct internal reforming solid oxide fuel cell: II. Model-based dynamic performance and control.* J. Power Sources, 2005. **147**(1–2): p. 136-147.
44. Molinelli, M., et al., *Dynamic behaviour of SOFC short stacks.* J. Power Sources, 2006. **154**(2): p. 394-403.
45. Weber, A., et al., *Oxidation of H2, CO and methane in SOFCs with Ni/YSZ-cermet anodes.* Solid State Ionics, 2002. **152–153**: p. 543-550.
46. Koh, J.-H., et al., *Carbon deposition and cell performance of Ni-YSZ anode support SOFC with methane fuel.* Solid State Ionics, 2002. **149**(3–4): p. 157-166.
47. Matsuzaki, Y. and I. Yasuda, *The poisoning effect of sulfur-containing impurity gas on a SOFC anode: Part I. Dependence on temperature, time, and impurity concentration.* Solid State Ionics, 2000. **132**(3–4): p. 261-269.
48. Gong, M., et al., *Sulfur-tolerant anode materials for solid oxide fuel cell application.* Journal of Power Sources, 2007. **168**(2): p. 289-298.
49. Kurokawa, H., et al., *Ceria Nanocoating for Sulfur Tolerant Ni-Based Anodes of Solid Oxide Fuel Cells.* Electrochemical and Solid-State Letters, 2007. **10**(9): p. B135-B138.
50. Gorte, R.J., et al., *Anodes for Direct Oxidation of Dry Hydrocarbons in a Solid-Oxide Fuel Cell.* Advanced Materials, 2000. **12**(19): p. 1465-1469.
51. Hui, S. and A. Petric, *Evaluation of yttrium-doped SrTiO3 as an anode for solid oxide fuel cells.* Journal of the European Ceramic Society, 2002. **22**(9–10): p. 1673-1681.
52. Marina, O.A., N.L. Canfield, and J.W. Stevenson, *Thermal, electrical, and electrocatalytical properties of lanthanum-doped strontium titanate.* Solid State Ionics, 2002. **149**(1–2): p. 21-28.
53. Lee, S., et al., *SOFC Anodes Based on Infiltration of La0.3Sr0.7TiO3.* Journal of The Electrochemical Society, 2008. **155**(11): p. B1179-B1183.
54. Neagu, D., et al., *In situ growth of nanoparticles through control of non-stoichiometry.* Nat Chem, 2013. **5**(11): p. 916-923.

55. Neagu, D., et al., *Nano-socketed nickel particles with enhanced coking resistance grown in situ by redox exsolution.* Nature Communications, 2015. **6**: p. 8120.
56. Myung, J.-h., et al., *Switching on electrocatalytic activity in solid oxide cells.* Nature, 2016. **537**(7621): p. 528-531.
57. Tao, S. and J.T.S. Irvine, *A redox-stable efficient anode for solid-oxide fuel cells.* Nat Mater, 2003. **2**(5): p. 320-323.
58. Kim, G., et al., *Investigation of the Structural and Catalytic Requirements for High-Performance SOFC Anodes Formed by Infiltration of LSCM.* Electrochemical and Solid-State Letters, 2009. **12**(3): p. B48-B52.
59. Kim, J.-S., et al., *A study of the methane tolerance of LSCM–YSZ composite anodes with Pt, Ni, Pd and ceria catalysts.* Scripta Materialia, 2011. **65**(2): p. 90-95.
60. Huang, Y.-H., et al., *Double Perovskites as Anode Materials for Solid-Oxide Fuel Cells.* Science, 2006. **312**(5771): p. 254.
61. Bossche, M.v.d. and S. McIntosh, *On the methane oxidation activity of Sr2(MgMo)2O6-[small delta]: a potential anode material for direct hydrocarbon solid oxide fuel cells.* Journal of Materials Chemistry, 2011. **21**(20): p. 7443-7451.
62. Ji, Y., et al., *Electrochemical performance of La-doped Sr2MgMoO6−δ in natural gas.* Electrochemistry Communications, 2007. **9**(8): p. 1881-1885.
63. Huang, Y.-H., et al., *Double-Perovskite Anode Materials Sr2MMoO6 (M = Co, Ni) for Solid Oxide Fuel Cells.* Chemistry of Materials, 2009. **21**(11): p. 2319-2326.
64. Sengodan, S., et al., *Layered oxygen-deficient double perovskite as an efficient and stable anode for direct hydrocarbon solid oxide fuel cells.* Nat Mater, 2015. **14**(2): p. 205-209.
65. Cheng, Z., et al., *Chemical, electrical, and thermal properties of strontium doped lanthanum vanadate.* Solid State Ionics, 2005. **176**(23–24): p. 1921-1928.
66. Zha, S., Z. Cheng, and M. Liu, *A Sulfur-Tolerant Anode Material for SOFCs.* Electrochemical and Solid-State Letters, 2005. **8**(8): p. A406-A408.
67. Chan, S.H., K.A. Khor, and Z.T. Xia, *A complete polarization model of a solid oxide fuel cell and its sensitivity to the change of cell component thickness.* Journal of Power Sources, 2001. **93**(1–2): p. 130-140.
68. Suzuki, T., et al., *Impact of Anode Microstructure on Solid Oxide Fuel Cells.* Science, 2009. **325**(5942): p. 852.
69. Othman, M.H.D., et al., *Novel fabrication technique of hollow fibre support for micro-tubular solid oxide fuel cells.* Journal of Power Sources, 2011. **196**(11): p. 5035-5044.
70. Yang, C., et al., *Fabrication and characterization of an anode-supported hollow fiber SOFC.* Journal of Power Sources, 2009. **187**(1): p. 90-92.
71. Yang, C., C. Jin, and F. Chen, *Micro-tubular solid oxide fuel cells fabricated by phase-inversion method.* Electrochemistry Communications, 2010. **12**(5): p. 657-660.
72. Wang, H. and J. Liu, *Effect of anode structure on performance of cone-shaped solid oxide fuel cells fabricated by phase inversion.* International Journal of Hydrogen Energy, 2012. **37**(5): p. 4339-4345.
73. Liu, T., et al., *Novel light-weight, high-performance anode-supported microtubular solid oxide fuel cells with an active anode functional layer.* Journal of Power Sources, 2015. **293**: p. 852-858.

74. Sun, W., et al., *Preparation of dual-pore anode supported Sc2O3-stabilized-ZrO2 electrolyte planar solid oxide fuel cell by phase-inversion and dip-coating.* Journal of Power Sources, 2012. **218**: p. 352-356.
75. Kharton, V.V., F.M.B. Marques, and A. Atkinson, *Transport properties of solid oxide electrolyte ceramics: a brief review.* Solid State Ionics, 2004. **174**(1–4): p. 135-149.
76. Yamamoto, O., et al., *Zirconia based oxide ion conductors for solid oxide fuel cells.* Ionics, 1998. **4**(5): p. 403-408.
77. Lee, D.S., et al., *Characterization of ZrO2 co-doped with Sc2O3 and CeO2 electrolyte for the application of intermediate temperature SOFCs.* Solid State Ionics, 2005. **176**(1–2): p. 33-39.
78. Will, J., et al., *Fabrication of thin electrolytes for second-generation solid oxide fuel cells.* Solid State Ionics, 2000. **131**(1–2): p. 79-96.
79. Zhao, F. and A.V. Virkar, *Dependence of polarization in anode-supported solid oxide fuel cells on various cell parameters.* J. Power Sources, 2005. **141**(1): p. 79-95.
80. Wang, J., et al., *Study of slurry spin coating technique parameters for the fabrication of anode-supported YSZ Films for SOFCs.* Journal of Power Sources, 2007. **164**(1): p. 17-23.
81. Brett, D.J.L., et al., *Intermediate temperature solid oxide fuel cells.* Chem. Soc. Rev., 2008. **37**(8): p. 1568-1578.
82. Jacobson, A.J., *Materials for Solid Oxide Fuel Cells.* Chem. Mater., 2010. **22**(3): p. 660-674.
83. Mai, A., et al., *Ferrite-based perovskites as cathode materials for anode-supported solid oxide fuel cells: Part I. Variation of composition.* Solid State Ionics, 2005. **176**(15–16): p. 1341-1350.
84. Duan, Z., et al., *Ba0.5Sr0.5Co0.8Fe0.2O3−δ as a cathode for IT-SOFCs with a GDC interlayer.* J. Power Sources, 2006. **160**(1): p. 57-64.
85. Kim, J.H., et al., *Electrochemical Investigation of Composite Cathodes with SmBa0.5Sr0.5Co2O5+δ Cathodes for Intermediate Temperature-Operating Solid Oxide Fuel Cell.* Chem. Mater., 2010. **22**(3): p. 883-892.
86. Steele, B.C.H., *Appraisal of Ce1−yGdyO2−y/2 electrolytes for IT-SOFC operation at 500 ℃.* Solid State Ionics, 2000. **129**(1–4): p. 95-110.
87. Eguchi, K., et al., *Electrical properties of ceria-based oxides and their application to solid oxide fuel cells.* Solid State Ionics, 1992. **52**(1): p. 165-172.
88. Mogensen, M., N.M. Sammes, and G.A. Tompsett, *Physical, chemical and electrochemical properties of pure and doped ceria.* Solid State Ionics, 2000. **129**(1–4): p. 63-94.
89. Tsoga, A., et al., *Performance of a double-layer CGO/YSZ electrolyte for solid oxide fuel cells.* Ionics, 1998. **4**(3): p. 234-240.
90. Marques, F.M.B. and L.M. Navarro, *Performance of double layer electrolyte cells Part II: GCO/YSZ, a case study.* Solid State Ionics, 1997. **100**(1): p. 29-38.
91. Hrovat, M., et al., *Interactions between lanthanum gallate based solid electrolyte and ceria.* Materials Research Bulletin, 1999. **34**(12–13): p. 2027-2034.

92. Hirabayashi, D., et al., *Design of a Reduction-Resistant Ce0.8Sm0.2 O 1.9 Electrolyte Through Growth of a Thin BaCe1 − x Sm x O 3 − α Layer over Electrolyte Surface.* Electrochemical and Solid-State Letters, 2004. **7**(10): p. A318-A320.
93. Jiang, N. and E.D. Wachsman, *Structural Stability and Conductivity of Phase-Stabilized Cubic Bismuth Oxides.* J. Am. Ceram. Soc., 1999. **82**(11): p. 3057-3064.
94. Jiang, N., E.D. Wachsman, and S.-H. Jung, *A higher conductivity Bi2O3-based electrolyte.* Solid State Ionics, 2002. **150**(3–4): p. 347-353.
95. Wachsman, E.D., et al., *Structural and defect studies in solid oxide electrolytes.* Solid State Ionics, 1992. **52**(1): p. 213-218.
96. Kruidhof, H., et al., *Bismuth oxide based ceramics with improved electrical and mechanical properties.* Materials Research Bulletin, 1988. **23**(3): p. 371-377.
97. Jiang, N., et al., *Aging phenomenon of stabilized bismuth oxides.* Mater. Res. Bull., 1994. **29**(3): p. 247-254.
98. Jung, D.W., et al., *Effect of Annealing Temperature and Dopant Concentration on the Conductivity Behavior in (DyO1.5)x–(WO3)y–(BiO1.5)1−x−y.* J. Am. Ceram. Soc., 2010. **93**(5): p. 1384-1391.
99. Jiang, N., et al., *Anion ordering in aged stabilized bismuth oxide.* Mater. Lett., 1995. **22**(5): p. 215-219.
100. Huang, K., M. Feng, and J.B. Goodenough, *Bi2O3 Y2O3 CeO2 solid solution oxide-ion electrolyte.* Solid State Ionics, 1996. **89**(1): p. 17-24.
101. Wachsman, E.D. and K.T. Lee, *Lowering the temperature of solid oxide fuel cells.* Science, 2011. **334**(6058): p. 935-939.
102. Lee, K.T., et al., *Interfacial modification of La0.80Sr0.20MnO3−δ–Er0.4Bi0.6O3 cathodes for high performance lower temperature solid oxide fuel cells.* J. Power Sources, 2012. **220**: p. 324-330.
103. Ishihara, T., H. Matsuda, and Y. Takita, *Doped LaGaO3 Perovskite Type Oxide as a New Oxide Ionic Conductor.* J. Am. Chem. Soc., 1994. **116**(9): p. 3801-3.
104. Huang, K., R.S. Tichy, and J.B. Goodenough, *Superior Perovskite Oxide-Ion Conductor; Strontium- and Magnesium-Doped LaGaO3: I, Phase Relationships and Electrical Properties.* J. Am. Ceram. Soc., 1998. **81**(10): p. 2565-2575.
105. Huang, K., R.S. Tichy, and J.B. Goodenough, *Superior Perovskite Oxide-Ion Conductor; Strontium- and Magnesium-Doped LaGaO3: II, ac Impedance Spectroscopy.* Journal of the American Ceramic Society, 1998. **81**(10): p. 2576-2580.
106. Hayashi, H., et al., *Structural consideration on the ionic conductivity of perovskite-type oxides.* Solid State Ionics, 1999. **122**(1–4): p. 1-15.
107. Khan, M.S., M.S. Islam, and D.R. Bates, *Dopant Substitution and Ion Migration in the LaGaO3-Based Oxygen Ion Conductor.* The Journal of Physical Chemistry B, 1998. **102**(17): p. 3099-3104.
108. Ishihara, T., et al., *Improved Oxide Ion Conductivity in La0.8Sr0.2Ga0.8Mg0.2O3 by Doping Co.* Chemistry of Materials, 1999. **11**(8): p. 2081-2088.
109. Ma, G., et al., *Proton Conduction in La0.9Sr0.1Ga0.8Mg0.2O3-α.* Chemistry of Materials, 2006. **18**(25): p. 6006-6011.

110. Nakayama, S., et al., *Ionic conductivity of lanthanoid silicates, Ln10(SiO4)6O3(Ln = La, Nd, Sm, Gd, Dy, Y, Ho, Er and Yb).* Journal of Materials Chemistry, 1995. **5**(11): p. 1801-1805.
111. Jones, A., P.R. Slater, and M.S. Islam, *Local Defect Structures and Ion Transport Mechanisms in the Oxygen-Excess Apatite La9.67(SiO4)6O2.5.* Chemistry of Materials, 2008. **20**(15): p. 5055-5060.
112. Ali, R., et al., *Diffusion Path of Oxide Ions in an Apatite-Type Ionic Conductor La9.69(Si5.70Mg0.30)O26.24.* Chemistry of Materials, 2008. **20**(16): p. 5203-5208.
113. Ishihara, T., et al., *Nonstoichiometric La2-xGeO5-δ Monoclinic Oxide as a New Fast Oxide Ion Conductor.* Journal of the American Chemical Society, 2001. **123**(2): p. 203-209.
114. León-Reina, L., et al., *High Oxide Ion Conductivity in Al-Doped Germanium Oxyapatite.* Chemistry of Materials, 2005. **17**(3): p. 596-600.
115. Shao, Z. and S.M. Haile, *A high-performance cathode for the next generation of solid-oxide fuel cells.* Nature, 2004. **431**(7005): p. 170-173.
116. Huang, K., J.-H. Wan, and J.B. Goodenough, *Increasing Power Density of LSGM-Based Solid Oxide Fuel Cells Using New Anode Materials.* J. Electrochem. Soc., 2001. **148**(7): p. A788-A794.
117. Wan, J.-H., J.Q. Yan, and J.B. Goodenough, *LSGM-Based Solid Oxide Fuel Cell with 1.4 W/cm2 Power Density and 30 Day Long-Term Stability.* J. Electrochem. Soc., 2005. **152**(8): p. A1511-A1515.
118. Zhan, Z., et al., *A reduced temperature solid oxide fuel cell with nanostructured anodes.* Energy Environ. Sci., 2011. **4**(10): p. 3951-3954.
119. Kreuer, K.D., *Proton-Conducting Oxides.* Annual Review of Materials Research, 2003. **33**(1): p. 333-359.
120. Iwahara, H., et al., *Proton conduction in sintered oxides and its application to steam electrolysis for hydrogen production.* Solid State Ionics, 1981. **3**: p. 359-363.
121. Iwahara, H., et al., *Proton Conduction in Sintered Oxides Based on BaCeO3.* Journal of The Electrochemical Society, 1988. **135**(2): p. 529-533.
122. Bonanos, N., K.S. Knight, and B. Ellis, *Perovskite solid electrolytes: Structure, transport properties and fuel cell applications.* Solid State Ionics, 1995. **79**: p. 161-170.
123. Bonanos, N. and F. Willy Poulsen, *Considerations of defect equilibria in high temperature proton-conducting cerates.* Journal of Materials Chemistry, 1999. **9**(2): p. 431-434.
124. Bonanos, N., *Oxide-based protonic conductors: point defects and transport properties.* Solid State Ionics, 2001. **145**(1–4): p. 265-274.
125. Phillips, R.J., et al., *Structural and electrical characterisation of SrCe1−xYxOξ.* Solid State Ionics, 1999. **125**(1–4): p. 389-395.
126. Sammes, N., R. Phillips, and A. Smirnova, *Proton conductivity in stoichiometric and sub-stoichiometric yittrium doped SrCeO3 ceramic electrolytes.* Journal of Power Sources, 2004. **134**(2): p. 153-159.
127. Ahlgren, E.O., *Thermoelectric power of SrCe0.95Y0.05O3−δ.* Solid State Ionics, 1997. **97**(1–4): p. 489-495.
128. Nowick, A.S. and Y. Du, *High-temperature protonic conductors with perovskite-related structures.* Solid State Ionics, 1995. **77**: p. 137-146.

129. Norby, T., *Solid-state protonic conductors: principles, properties, progress and prospects.* Solid State Ionics, 1999. **125**(1–4): p. 1-11.
130. Iwahara, H., *Proton conducting ceramics and their applications.* Solid State Ionics, 1996. **86**: p. 9-15.
131. Pionke, M., et al., *Investigation of the hydrogen mobility in a mixed perovskite: Ba[Ca(1+x)/3Nb(2−x)/3]O3−x/2 by quasielastic neutron scattering.* Solid State Ionics, 1997. **97**(1–4): p. 497-504.
132. Matzke, T., et al., *Quasielastic thermal neutron scattering experiment on the proton conductor SrCe0.95Yb0.05H0.02O2.985.* Solid State Ionics, 1996. **86**: p. 621-628.
133. Münch, W., et al., *Proton diffusion in perovskites: comparison between BaCeO3, BaZrO3, SrTiO3, and CaTiO3 using quantum molecular dynamics.* Solid State Ionics, 2000. **136–137**: p. 183-189.
134. Münch, W., et al., *A quantum molecular dynamics study of proton conduction phenomena in BaCeO3.* Solid State Ionics, 1996. **86**: p. 647-652.
135. Karlsson, M., et al., *Vibrational properties of protons in hydrated $\mathrm{Ba}{\mathrm{In}}_{x}{\mathrm{Zr}}_{1\ensuremath{-}x}{\mathrm{O}}_{3\ensuremath{-}x/2}$.* Physical Review B, 2005. **72**(9): p. 094303.
136. Gomez, M.A., et al., *The effect of octahedral tilting on proton binding sites and transition states in pseudo-cubic perovskite oxides.* The Journal of Chemical Physics, 2005. **123**(9): p. 094703.
137. Taniguchi, N., et al., *Proton conductive properties of gadolinium-doped barium cerates at high temperatures.* Solid State Ionics, 1992. **53**: p. 998-1003.
138. Stevenson, D.A., et al., *Characterization of Gd, Yb and Nd doped barium cerates as proton conductors.* Solid State Ionics, 1993. **62**(3): p. 279-285.
139. Ma, G., T. Shimura, and H. Iwahara, *Ionic conduction and nonstoichiometry in BaxCe0.90Y0.10O3−α.* Solid State Ionics, 1998. **110**(1–2): p. 103-110.
140. Kikuchi, J., et al., *Ionic conductivity in lanthanoid ion-doped BaCeLnO3 electrolytes.* Solid State Ionics, 2008. **179**(27–32): p. 1413-1416.
141. Shima, D. and S.M. Haile, *The influence of cation non-stoichiometry on the properties of undoped and gadolinia-doped barium cerate.* Solid State Ionics, 1997. **97**(1–4): p. 443-455.
142. Zhang, C., H. Zhao, and S. Zhai, *Electrical conduction behavior of proton conductor BaCe1-xSmxO3-δ in the intermediate temperature range.* Inter. J. Hydrogen Energy, 2011. **36**(5): p. 3649-3657.
143. Glöckner, R., M.S. Islam, and T. Norby, *Protons and other defects in BaCeO3: a computational study.* Solid State Ionics, 1999. **122**(1–4): p. 145-156.
144. Mather, G.C. and M.S. Islam, *Defect and Dopant Properties of the SrCeO3-Based Proton Conductor.* Chemistry of Materials, 2005. **17**(7): p. 1736-1744.
145. Wu, J., et al., *Atomistic Study of Doped BaCeO3: Dopant Site-Selectivity and Cation Nonstoichiometry.* Chemistry of Materials, 2005. **17**(4): p. 846-851.
146. Wu, J., et al., *Dopant site selectivity in BaCe0.85M0.15O3-δ by extended x-ray absorption fine structure.* Journal of Applied Physics, 2005. **97**(5): p. 054101.
147. Levitskii, V.A., et al., *Phase relationships and thermodynamic parameters in the BaO-CeO system for 0-50 mol. % BaO.* Inorg. Mater. (Engl. Transl.); (United States), 1986: p. Medium: X; Size: Pages: 1190-1193.

148. Zakowsky, N., S. Williamson, and J.T.S. Irvine, *Elaboration of CO2 tolerance limits of BaCe0.9Y0.1O3–δ electrolytes for fuel cells and other applications.* Solid State Ionics, 2005. **176**(39–40): p. 3019-3026.
149. Taniguchi, N., E. Yasumoto, and T. Gamo, *Operating Properties of Solid Oxide Fuel Cells Using BaCe0.8Gd0.2 O 3 − α Electrolyte.* Journal of The Electrochemical Society, 1996. **143**(6): p. 1886-1890.
150. Wu, Z. and M. Liu, *Stability of BaCe0.8Gd0.2 O 3 in a H 2 O -Containing Atmosphere at Intermediate Temperatures.* Journal of The Electrochemical Society, 1997. **144**(6): p. 2170-2175.
151. Bhide, S.V. and A.V. Virkar, *Stability of BaCeO3-Based Proton Conductors in Water-Containing Atmospheres.* Journal of The Electrochemical Society, 1999. **146**(6): p. 2038-2044.
152. Tao, S.W. and J.T.S. Irvine, *A Stable, Easily Sintered Proton- Conducting Oxide Electrolyte for Moderate-Temperature Fuel Cells and Electrolyzers.* Advanced Materials, 2006. **18**(12): p. 1581-1584.
153. Xie, K., et al., *A stable and easily sintering BaCeO3-based proton-conductive electrolyte.* Journal of Alloys and Compounds, 2009. **473**(1–2): p. 323-329.
154. Bi, L., et al., *Indium as an ideal functional dopant for a proton-conducting solid oxide fuel cell.* International Journal of Hydrogen Energy, 2009. **34**(5): p. 2421-2425.
155. Pergolesi, D., et al., *High proton conduction in grain-boundary-free yttrium-doped barium zirconate films grown by pulsed laser deposition.* Nat Mater, 2010. **9**(10): p. 846-852.
156. Tao, S. and J.T.S. Irvine, *Conductivity studies of dense yttrium-doped BaZrO3 sintered at 1325 ℃.* Journal of Solid State Chemistry, 2007. **180**(12): p. 3493-3503.
157. Zhang, C., et al., *Influence of ZnO addition on the properties of high temperature proton conductor Ba1.03Ce0.5Zr0.4Y0.1O3−δ synthesized via citrate–nitrate method.* International Journal of Hydrogen Energy, 2009. **34**(6): p. 2739-2746.
158. Tong, J., et al., *Solid-state reactive sintering mechanism for large-grained yttrium-doped barium zirconate proton conducting ceramics.* Journal of Materials Chemistry, 2010. **20**(30): p. 6333-6341.
159. Nikodemski, S., J. Tong, and R. O'Hayre, *Solid-state reactive sintering mechanism for proton conducting ceramics.* Solid State Ionics, 2013. **253**: p. 201-210.
160. Duan, C., et al., *Readily processed protonic ceramic fuel cells with high performance at low temperatures.* Science, 2015. **349**(6254): p. 1321.
161. Fabbri, E., et al., *Chemically Stable Pr and Y Co-Doped Barium Zirconate Electrolytes with High Proton Conductivity for Intermediate-Temperature Solid Oxide Fuel Cells.* Advanced Functional Materials, 2011. **21**(1): p. 158-166.
162. Yamazaki, Y., R. Hernandez-Sanchez, and S.M. Haile, *High Total Proton Conductivity in Large-Grained Yttrium-Doped Barium Zirconate.* Chemistry of Materials, 2009. **21**(13): p. 2755-2762.
163. Ryu, K.H. and S.M. Haile, *Chemical stability and proton conductivity of doped BaCeO3–BaZrO3 solid solutions.* Solid State Ionics, 1999. **125**(1–4): p. 355-367.
164. Zuo, C., et al., *Ba(Zr0.1Ce0.7Y0.2)O3–δ as an Electrolyte for Low-Temperature Solid-Oxide Fuel Cells.* Advanced Materials, 2006. **18**(24): p. 3318-3320.

165. Katahira, K., et al., *Protonic conduction in Zr-substituted BaCeO3.* Solid State Ionics, 2000. **138**(1,2): p. 91-98.
166. Taniguchi, N., C. Nishimura, and J. Kato, *Endurance against moisture for protonic conductors of perovskite-type ceramics and preparation of practical conductors.* Solid State Ionics, 2001. **145**(1–4): p. 349-355.
167. Bi, L., et al., *Fabrication and characterization of easily sintered and stable anode-supported proton-conducting membranes.* Journal of Membrane Science, 2009. **336**(1–2): p. 1-6.
168. Fabbri, E., et al., *Design and fabrication of a chemically-stable proton conductor bilayer electrolyte for intermediate temperature solid oxide fuel cells (IT-SOFCs).* Energy & Environmental Science, 2008. **1**(3): p. 355-359.
169. Carter, S., et al., *Oxygen transport in selected nonstoichiometric perovskite-structure oxides.* Solid State Ionics, 1992. **53**: p. 597-605.
170. Nakajo, A., Z. Wuillemin, and D. Favrat, *Simulation of thermal stresses in anode-supported solid oxide fuel cell stacks. Part I: Probability of failure of the cells.* Journal of Power Sources, 2009. **193**(1): p. 203-215.
171. Mai, A., et al., *Time-dependent performance of mixed-conducting SOFC cathodes.* Solid state ionics, 2006. **177**(19): p. 1965-1968.
172. Tucker, M.C., et al., *A fundamental study of chromium deposition on solid oxide fuel cell cathode materials.* Journal of Power Sources, 2006. **160**(1): p. 130-138.
173. van Heuveln, F.H. and H.J.M. Bouwmeester, *Electrode Properties of Sr-Doped LaMnO3 on Yttria-Stabilized Zirconia: II. Electrode Kinetics.* J. Electrochem. Soc., 1997. **144**(1): p. 134-140.
174. Adler, S.B., *Factors Governing Oxygen Reduction in Solid Oxide Fuel Cell Cathodes.* Chemical Reviews, 2004. **104**(10): p. 4791-4844.
175. Wang, W. and S.P. Jiang, *A mechanistic study on the activation process of (La, Sr)MnO3 electrodes of solid oxide fuel cells.* Solid State Ionics, 2006. **177**(15–16): p. 1361-1369.
176. Jiang, S.P. and J.G. Love, *Origin of the initial polarization behavior of Sr-doped LaMnO3 for O2 reduction in solid oxide fuel cells.* Solid State Ionics, 2001. **138**(3–4): p. 183-190.
177. Jiang, S.P., et al., *The electrochemical performance of LSM/zirconia–yttria interface as a function of a-site non-stoichiometry and cathodic current treatment.* Solid State Ionics, 1999. **121**(1–4): p. 1-10.
178. Jiang, S.P. and J.G. Love, *Observation of structural change induced by cathodic polarization on (La,Sr)MnO3 electrodes of solid oxide fuel cells.* Solid State Ionics, 2003. **158**(1–2): p. 45-53.
179. Horita, T., et al., *Active Sites Imaging for Oxygen Reduction at the La0.9Sr0.1MnO3 − x /Yttria-Stabilized Zirconia Interface by Secondary-Ion Mass Spectrometry.* Journal of The Electrochemical Society, 1998. **145**(9): p. 3196-3202.
180. Gharbage, B., T. Pagnier, and A. Hammou, *Oxygen Reduction at La0.5Sr0.5MnO3 Thin Film/Yttria-Stabilized Zirconia Interface Studied by Impedance Spectroscopy.* Journal of The Electrochemical Society, 1994. **141**(8): p. 2118-2121.
181. Zheng, Y., R. Ran, and Z. Shao, *Activation and Deactivation Kinetics of Oxygen Reduction over a La0.8Sr0.2Sc0.1Mn0.9O3 Cathode.* The Journal of Physical Chemistry C, 2008. **112**(47): p. 18690-18700.

182. Jiang, S.P., *Development of lanthanum strontium manganite perovskite cathode materials of solid oxide fuel cells: a review.* J. Mater. Sci., 2008. **43**(21): p. 6799-6833.
183. Perry Murray, E. and S.A. Barnett, *(La,Sr)MnO3–(Ce,Gd)O2−x composite cathodes for solid oxide fuel cells.* Solid State Ionics, 2001. **143**(3–4): p. 265-273.
184. Steele, B.C.H., *Interfacial reactions associated with ceramic ion transport membranes.* Solid State Ionics, 1995. **75**: p. 157-165.
185. Jiang, Z., et al., *Electrochemical characteristics of solid oxide fuel cell cathodes prepared by infiltrating (La,Sr)MnO3 nanoparticles into yttria-stabilized bismuth oxide backbones.* Inter. J. Hydrogen Energy, 2010. **35**(15): p. 8322-8330.
186. Jiang, Z., et al., *Bismuth oxide-coated (La,Sr)MnO3 cathodes for intermediate temperature solid oxide fuel cells with yttria-stabilized zirconia electrolytes.* Electrochim. Acta, 2009. **54**(11): p. 3059-3065.
187. Jiang, Z., et al., *Nanoscale bismuth oxide impregnated (La,Sr)MnO3 cathodes for intermediate-temperature solid oxide fuel cells.* J. Power Sources, 2008. **185**(1): p. 40-48.
188. Li, J., et al., *La0.84Sr0.16MnO3−δ cathodes impregnated with Bi1.4Er0.6O3 for intermediate-temperature solid oxide fuel cells.* J. Power Sources, 2009. **194**(2): p. 625-630.
189. Li, J., et al., *(La0.74Bi0.10Sr0.16)MnO3−δ–(Bi2O3)0.7(Er2O3)0.3 composite cathodes for intermediate temperature solid oxide fuel cells.* J. Power Sources, 2008. **179**(2): p. 474-480.
190. Li, J., et al., *(La0.74Bi0.10Sr0.16)MnO3−δ–Ce0.8Gd0.2O2−δ cathodes fabricated by ion-impregnating method for intermediate-temperature solid oxide fuel cells.* J. Power Sources, 2009. **188**(2): p. 453-457.
191. Hou, J., et al., *High performance ceria-bismuth bilayer electrolyte low temperature solid oxide fuel cells (LT-SOFCs) fabricated by combining co-pressing with drop-coating.* J. Mater. Chem. A, 2015. **3**(19): p. 10219-10224.
192. Esquirol, A., et al., *Electrochemical Characterization of La0. 6Sr0. 4Co0. 2Fe0. 8 O 3 Cathodes for Intermediate-Temperature SOFCs.* Journal of The Electrochemical Society, 2004. **151**(11): p. A1847-A1855.
193. Leng, Y., S.H. Chan, and Q. Liu, *Development of LSCF–GDC composite cathodes for low-temperature solid oxide fuel cells with thin film GDC electrolyte.* International Journal of Hydrogen Energy, 2008. **33**(14): p. 3808-3817.
194. Marinha, D., et al., *Performance of (La, Sr)(Co, Fe) O 3− x double-layer cathode films for intermediate temperature solid oxide fuel cell.* Journal of Power Sources, 2011. **196**(11): p. 5084-5090.
195. Liu, M., et al., *Enhanced performance of LSCF cathode through surface modification.* International Journal of Hydrogen Energy, 2012. **37**(10): p. 8613-8620.
196. Shah, M. and S.A. Barnett, *Solid oxide fuel cell cathodes by infiltration of La0.6Sr0.4Co0.2Fe0.8O3 − δ into Gd-Doped Ceria.* Solid State Ionics, 2008. **179**(35–36): p. 2059-2064.
197. Tietz, F., A. Mai, and D. Stöver, *From powder properties to fuel cell performance–A holistic approach for SOFC cathode development.* Solid State Ionics, 2008. **179**(27): p. 1509-1515.

198. Ding, H., et al., *Suppression of Sr surface segregation in La 1− x Sr x Co 1− y Fe y O 3− δ: a first principles study.* Physical Chemistry Chemical Physics, 2013. **15**(2): p. 489-496.
199. Zhao, H., et al., *Structural and electrochemical studies of Ba0.6Sr0.4Co1−yTiyO3−δ as a new cathode material for IT-SOFCs.* Journal of Power Sources, 2009. **186**(2): p. 305-310.
200. Wei, B., et al., *Synthesis, electrical and electrochemical properties of Ba0.5Sr0.5Zn0.2Fe0.8O3−δ perovskite oxide for IT-SOFC cathode.* Journal of Power Sources, 2008. **176**(1): p. 1-8.
201. Pavone, M., A.M. Ritzmann, and E.A. Carter, *Quantum-mechanics-based design principles for solid oxide fuel cell cathode materials.* Energy & Environmental Science, 2011. **4**(12): p. 4933-4937.
202. Lee, Y.-L. and D. Morgan, *Ab initio and empirical defect modeling of LaMnO 3±δ for solid oxide fuel cell cathodes.* Physical Chemistry Chemical Physics, 2012. **14**(1): p. 290-302.
203. Mastrikov, Y.A., et al., *Pathways for oxygen incorporation in mixed conducting perovskites: A DFT-based mechanistic analysis for (La, Sr) MnO3− δ.* The Journal of Physical Chemistry C, 2010. **114**(7): p. 3017-3027.
204. Solomon, J.M., et al., *First principles study of pyrophosphate defects and dopant–defect interactions in stronium-doped lanthanum orthophosphate.* Journal of Materials Chemistry A, 2014. **2**(4): p. 1047-1053.
205. Hohenberg, P. and W. Kohn, *Inhomogeneous electron gas.* Physical review, 1964. **136**(3B): p. B864.
206. Kohn, W. and L. Sham, *Physical Review 140.* A1133, 1965.
207. Jones, R.O. and O. Gunnarsson, *The density functional formalism, its applications and prospects.* Reviews of Modern Physics, 1989. **61**(3): p. 689.
208. Kohn, W., *Electronic structure of matter-wave functions and density functionals.* Nobel Lectures: Chemistry, 2003: p. 213.
209. Kohn, W., *Nobel Lecture: Electronic structure of matter—wave functions and density functionals.* Reviews of Modern Physics, 1999. **71**(5): p. 1253.
210. Hafner, J., *Atomic-scale computational materials science.* Acta Materialia, 2000. **48**(1): p. 71-92.
211. Perdew, J.P., et al., *Atoms, molecules, solids, and surfaces: Applications of the generalized gradient approximation for exchange and correlation.* Physical Review B, 1992. **46**(11): p. 6671.
212. Perdew, J.P., et al., *Erratum: Atoms, molecules, solids, and surfaces: Applications of the generalized gradient approximation for exchange and correlation.* Physical Review B, 1993. **48**(7): p. 4978.
213. Perdew, J.P., K. Burke, and M. Ernzerhof, *Generalized gradient approximation made simple.* Physical review letters, 1996. **77**(18): p. 3865.
214. Singh, D.J. and L. Nordstrom, *Planewaves, Pseudopotentials, and the LAPW method*. 2006: Springer Science & Business Media.
215. Seminario, J.M., *An introduction to density functional theory in chemistry.* Theoretical and computational chemistry, 1995. **2**: p. 1-27.
216. Sholl, D. and J.A. Steckel, *Density functional theory: a practical introduction*. 2011: John Wiley & Sons.

217. Sousa, S.F., P.A. Fernandes, and M.J. Ramos, *General performance of density functionals.* The Journal of Physical Chemistry A, 2007. **111**(42): p. 10439-10452.
218. Perdew, J., K. Burke, and M. Ernzerhof, *Phys Rev Lett 77: 3865.* Errata:(1997) Phys Rev Lett, 1996. **78**: p. 1396.
219. Hammer, B., L.B. Hansen, and J.K. Nørskov, *Improved adsorption energetics within density-functional theory using revised Perdew-Burke-Ernzerhof functionals.* Physical Review B, 1999. **59**(11): p. 7413.
220. Kresse, G. and J. Furthmueller, *VASP the Guide; University of Vienna: Vienna, Austria, 2003.* There is no corresponding record for this reference.
221. Kresse, G. and J. Hafner, *Ab initio molecular-dynamics simulation of the liquid-metal–amorphous-semiconductor transition in germanium.* Physical Review B, 1994. **49**(20): p. 14251.
222. Kresse, G. and J. Furthmüller, *Efficiency of ab-initio total energy calculations for metals and semiconductors using a plane-wave basis set.* Computational Materials Science, 1996. **6**(1): p. 15-50.
223. Blöchl, P.E., *Projector augmented-wave method.* Physical Review B, 1994. **50**(24): p. 17953.
224. Pornprasertsuk, R., et al., *Predicting ionic conductivity of solid oxide fuel cell electrolyte from first principles.* Journal of applied physics, 2005. **98**(10): p. 103513.
225. Rossmeisl, J. and W.G. Bessler, *Trends in catalytic activity for SOFC anode materials.* Solid State Ionics, 2008. **178**(31): p. 1694-1700.
226. Choi, Y., et al., *Oxygen Reduction on LaMnO3-Based Cathode Materials in Solid Oxide Fuel Cells.* Chemistry of Materials, 2007. **19**(7): p. 1690-1699.
227. Choi, Y., et al., *Continuum and quantum-chemical modeling of oxygen reduction on the cathode in a solid oxide fuel cell.* Topics in Catalysis, 2007. **46**(3-4): p. 386-401.
228. Nikolla, E., J. Schwank, and S. Linic, *Promotion of the long-term stability of reforming Ni catalysts by surface alloying.* Journal of catalysis, 2007. **250**(1): p. 85-93.
229. Galea, N.M., D. Knapp, and T. Ziegler, *Density functional theory studies of methane dissociation on anode catalysts in solid-oxide fuel cells: suggestions for coke reduction.* Journal of Catalysis, 2007. **247**(1): p. 20-33.
230. Zhu, B., *Solid oxide fuel cell (SOFC) technical challenges and solutions from nano-aspects.* International Journal of Energy Research, 2009. **33**(13): p. 1126-1137.
231. Di, J., et al., *Samarium doped ceria–(Li/Na)2CO3 composite electrolyte and its electrochemical properties in low temperature solid oxide fuel cell.* Journal of Power Sources, 2010. **195**(15): p. 4695-4699.
232. Wang, X., et al., *Novel core–shell SDC/amorphous Na 2 CO 3 nanocomposite electrolyte for low-temperature SOFCs.* Electrochemistry Communications, 2008. **10**(10): p. 1617-1620.
233. Zhu, B., et al., *Innovative solid carbonate–ceria composite electrolyte fuel cells.* Electrochemistry communications, 2001. **3**(10): p. 566-571.
234. Tao, S. and J.T.S. Irvine, *Conductivity studies of dense yttrium-doped BaZrO3 sintered at 1325 °C.* Journal of Solid State Chemistry, 2007. **180**(12): p. 3493-3503.

235. Park, K.-Y., et al., *Highly conductive barium zirconate-based carbonate composite electrolytes for intermediate temperature-protonic ceramic fuel cells.* J. Alloys Compd., 2014. **585**: p. 103-110.
236. Kojima, T., et al., *Physical properties of molten Li2CO3-Na2CO3 (52:48 mol%) and Li2CO3-K2CO3 (62:38 mol%) containing additives.* J. Electrochem. Soc., 2013. **160**(10): p. H733-H741.
237. Grzechnik, A., P. Bouvier, and L. Farina, *High-pressure structure of Li 2 CO 3.* Journal of Solid State Chemistry, 2003. **173**(1): p. 13-19.
238. Islam, M.S., et al., *Doping and defect association in AZrO 3 (A= Ca, Ba) and LaMO 3 (M= Sc, Ga) perovskite-type ionic conductors.* Dalton Transactions, 2004(19): p. 3061-3066.
239. Heifets, E., J. Ho, and B. Merinov, *Density functional simulation of the Ba Zr O 3 (011) surface structure.* Physical Review B, 2007. **75**(15): p. 155431.
240. Nowick, A. and Y. Du, *High-temperature protonic conductors with perovskite-related structures.* Solid State Ionics, 1995. **77**: p. 137-146.
241. Münch, W., et al., *A quantum molecular dynamics study of the cubic phase of BaTiO 3 and BaZrO 3.* Solid State Ionics, 1997. **97**(1): p. 39-44.
242. Fabbri, E., D. Pergolesi, and E. Traversa, *Materials challenges toward proton-conducting oxide fuel cells: a critical review.* Chemical Society Reviews, 2010. **39**(11): p. 4355-4369.
243. Fabbri, E., et al., *Towards the Next Generation of Solid Oxide Fuel Cells Operating Below 600° C with Chemically Stable Proton-Conducting Electrolytes.* Advanced Materials, 2012. **24**(2): p. 195-208.
244. Münch, W., et al., *A quantum molecular dynamics study of proton conduction phenomena in BaCeO 3.* Solid State Ionics, 1996. **86**: p. 647-652.
245. Pionke, M., et al., *Investigation of the hydrogen mobility in a mixed perovskite: Ba [Ca (1+ x)/3 Nb (2− x)/3] O 3− x/2 by quasielastic neutron scattering.* Solid State Ionics, 1997. **97**(1): p. 497-504.
246. Kreuer, K.-D., A. Fuchs, and J. Maier, *HD isotope effect of proton conductivity and proton conduction mechanism in oxides.* Solid State Ionics, 1995. **77**: p. 157-162.
247. Becke, A.D., *Density-functional thermochemistry. III. The role of exact exchange.* The Journal of chemical physics, 1993. **98**(7): p. 5648-5652.
248. Lee, C., W. Yang, and R.G. Parr, *Development of the Colle-Salvetti correlation-energy formula into a functional of the electron density.* Physical review B, 1988. **37**(2): p. 785.
249. Rassolov, V.A., et al., *6-31G* basis set for third-row atoms.* Journal of Computational Chemistry, 2001. **22**(9): p. 976-984.
250. Rassolov, V.A., et al., *6-31G* basis set for atoms K through Zn.* The Journal of chemical physics, 1998. **109**(4): p. 1223-1229.
251. Blaudeau, J.-P., et al., *Extension of Gaussian-2 (G2) theory to molecules containing third-row atoms K and Ca.* The Journal of chemical physics, 1997. **107**(13): p. 5016-5021.
252. Francl, M.M., et al., *Self-consistent molecular orbital methods. XXIII. A polarization-type basis set for second-row elements.* The Journal of Chemical Physics, 1982. **77**(7): p. 3654-3665.

253. McLean, A. and G. Chandler, *0Contracted Gaussian basis sets for molecular calculations. I. Second row atoms, Z] 115181 J.* Chem Phys, 1980. **72**(10): p. 5639.
254. Krishnan, R., et al., *Self-consistent molecular orbital methods. XX. A basis set for correlated wave functions.* The Journal of Chemical Physics, 1980. **72**(1): p. 650-654.
255. Clark, T., et al., *Efficient diffuse function-augmented basis sets for anion calculations. III. The 3-21+ G basis set for first-row elements, Li–F.* Journal of Computational Chemistry, 1983. **4**(3): p. 294-301.
256. Montgomery Jr, J.A., et al., *A complete basis set model chemistry. VI. Use of density functional geometries and frequencies.* The Journal of chemical physics, 1999. **110**(6): p. 2822-2827.
257. Hay, P.J. and W.R. Wadt, *Ab initio effective core potentials for molecular calculations. Potentials for K to Au including the outermost core orbitals.* The Journal of Chemical Physics, 1985. **82**(1): p. 299-310.
258. Wadt, W.R. and P.J. Hay, *Ab initio effective core potentials for molecular calculations. Potentials for main group elements Na to Bi.* The Journal of Chemical Physics, 1985. **82**(1): p. 284-298.
259. Krishnan, R. and J.A. Pople, *Approximate fourth-order perturbation theory of the electron correlation energy.* International Journal of Quantum Chemistry, 1978. **14**(1): p. 91-100.
260. Scuseria, G.E., C.L. Janssen, and H.F. Schaefer Iii, *An efficient reformulation of the closed-shell coupled cluster single and double excitation (CCSD) equations.* The Journal of Chemical Physics, 1988. **89**(12): p. 7382-7387.
261. Janz, G.J. and M.R. Lorenz, *Solid-Liquid Phase Equilibria for Mixtures of Lithium, Sodium, and Potassium Carbonates.* Journal of Chemical & Engineering Data, 1961. **6**(3): p. 321-323.
262. Kournoutis, V.C., F. Tietz, and S. Bebelis, *AC Impedance Characterisation of a La0. 8Sr0. 2Co0. 2Fe0. 8O3–δ Electrode.* Fuel Cells, 2009. **9**(6): p. 852-860.
263. Van Heuveln, F. and H. Bouwmeester, *Electrode Properties of Sr-Doped LaMnO3 on Yttria-Stabilized Zirconia II. Electrode Kinetics.* Journal of The Electrochemical Society, 1997. **144**(1): p. 134-140.
264. Qin, C. and A. Gladney, *DFT study of CO42- and CO52- relevant to oxygen reduction with the presence of molten carbonate in solid oxide fuel cells.* Comput. Theor. Chem., 2012. **999**: p. 179-183.